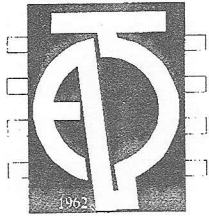


ЕЛЕКТРОТЕХНИЧКИ ФАКУЛТЕТ
УНИВЕРЗИТЕТА У БАЊАЛУЦИ
FACULTY OF ELECTRICAL ENGINEERING
UNIVERSITY OF BANJALUKA

ЕЛЕКТРОНИКА ELECTRONICS

ГОДИШТЕ 2, БРОЈ 1, СЕПТЕМБАР 1998. • VOLUME 2, NUMBER 1, SEPTEMBER 1998



ЕЛЕКТРОТЕХНИЧКИ ФАКУЛТЕТ БАЊАЛУКА

Адреса: Патре 5, Бањалука
Тел: 00381 78 11 408 00381 78 11 418
Факс: 00381 78 11 408

ЕЛЕКТРОНИКА

Уредник: проф. др Бранко Л. Докић, Електротехнички факултет,
Универзитет у Бањалуци, Република Српска
e-mail: bdokic@etf-bl.rstel.net

УРЕЂИВАЧКИ ОДБОР :

- Nikolaos Uzunoglu, National Technical University of Athens, Greece
- Barry Jefferies, University of Hertfordshire, UK
- Војин Оклобџија, University of California, Davis, USA
- Братислав Миловановић, Електронски факултет Ниш, СРЈ
- Милић Стојић, Електротехнички факултет Београд, СРЈ
- Војислав Аранђеловић, Институт "Винча" Београд, СРЈ
- Вељко Милутиновић, Електротехнички факултет Београд, СРЈ
- Илија Стојановић, САНУ Београд, СРЈ
- Владимир Катић, Технички факултет Нови Сад, СРЈ
- Александар Илишковић, Електротехнички факултет Бањалука, РС
- Златко Бундало, Електротехнички факултет Бањалука, РС

Секретар: дипл. инг. ел. Милан Лукић, Електротехнички факултет,
Универзитет у Бањалуци, Република Српска
e-mail: mlukic@etf-bl.rstel.net

Лектори: Милена Мандић, за српски језик
Радомир Косић, за енглески језик

Издавач:
Електротехнички факултет, Универзитет у Бањалуци
Адреса: Патре 5, Бањалука
Тел: 00381 78 11 408 00381 78 11 418
Факс: 00381 78 11 408

Штампа:
ЕУРОПРИНТ, Бањалука
ТИРАЖ: 100

UDK 621.38

ISSN 1450-5843

GUEST EDITOR
PROF. DR. MILIĆ R. STOJIĆ



Milić R. Stojić was born in Užice, Serbia, Yugoslavia, on February 27, 1940. He received the B.S., M.S., and Ph.D. degrees from the Electrical Engineering Faculty, University of Belgrade, in 1963, 1965, and 1967, respectively.

Since 1980, he has been a full Professor at the Electrical Engineering Faculty, University of Belgrade, teaching graduate and postgraduate courses in automatic control. In 1980, 1984, and 1988, he spent six months at the Physics Department, University of Birmingham, U.K., under a Cooperative Research Program. His scientific interests are: stability theory, sensitivity analysis of dynamic systems, system simulation, and microcomputer-based real time control of electrical drives and industrial processes. He teaches graduate and postgraduate courses in automatic control at the Faculty of Electrical Engineering, University of Belgrade; Faculty of Electronic Engineering, University of Niš; Faculty of Technical Science, University of Novi Sad; Faculty of Mechanical Engineering, University of Kragujevac; and Faculty of Electrical Engineering, University of Banjaluka. He has published six books and over 130 papers in scientific journals and conferences. He is the author of *Continuous Control Systems*, 8th edition. (Belgrade, Yugoslavia: Science, 1996) and *Digital Control Systems*, 3rd edition. (Belgrade, Yugoslavia: Science, 1994), written in Serbian, which are used as standard textbooks on automatic control at universities in Yugoslavia. He is the co-author of two monographs in Serbian, one monograph in English, and the author of one monograph in Russian. He also designed and equipped two analog and digital student laboratories.

Professor Stojic has been awarded the October Prize of the City of Belgrade (1980) by the City Council; Golden Medal of Work (1979) by the Yugoslav Government; IFIP Prize, for the best paper (1970); three prizes "Dišan Mitrović", for the best papers at the ETRAN Conferences (1973, 1981, and 1990); Prize "Professor Branko Raković", for the best papers published in distinguished international journals (1993); Tesla's Prize (1993), for prominent technical achievements; and charters of merit by several universities and professional organizations in Yugoslavia.

Professor Stojić is the president of the Society for Electronics, Telecommunications, Computers, Automation, and Nuclear Engineering (ETRAN) and the secretary of the Technical Division of Serbian Scientific Society. He has been the associate editor of *Automatica*, International Journal of IFAC, and the editor-in-chief of *Publications of Electrical Engineering Faculty*, Belgrade. Now he is the editor of *Scientific Review, Series: Science and Engineering*, Journal of the Serbian Scientific Society. Professor Stojić is a member of editorial boards of *Facta Universitatis, Series: Electronics and Energetics*, Journal of the University of Niš, and *Electronics*, Journal of Faculty of Electrical Engineering, University of Banjaluka.

P R E D G O V O R

Počastvovan sam pozivom Dekana Elektrotehničkog fakulteta u Banjaluci prof. dr Branka Dokića da budem gost urednik ove sveske časopisa *Electronics*, naučnog glasila Univerziteta u Banjaluci. Elektrotehnički fakultet u Banjaluci je osnovan uz podršku više uglednih profesora Elektrotehničkog fakulteta u Beogradu koji od osnivanja Fakulteta stalno ili povremeno održavaju nastavu u Banjaluci iz predmeta redovnih i postdiplomskih studija. Kvalitetom nastavnog kadra, učešćem u naučnoistraživačkim projektima i saradnjom sa privredom Elektrotehnički fakultet u Banjaluci je stekao visok ugled visokoškolske i naučne ustanove u Republici Srpskoj i Bosni i Hercegovini. Tom ugledu je značajno doprineo rad Fakulteta u otežanim uslovima ratom zahvaćene zemlje.

U ovu svesku uvrstio sam radove poznatih autoriteta u oblasti elektronike i njene primene u srodnim područjima. Prvi članak je skraćena verzija plenarnog rada podnetog na XLII Konferenciji ETRAN-a održanoj početkom juna u Vrnjačkoj Banji. Rad je privukao pažnju velikog broja učesnika Konferencije, pa će otuda uskoro u celini biti štampan kao brošura u izdanju Društva za ETRAN. Pet članaka su proširene verzije radova po pozivu i zapaženih radova podnetih na Konferenciji ETRAN-a. Ostali radovi su originalni naučni doprinosi koji se prvi put saopštavaju stručnoj javnosti.

Nadam se da će ovo izdanje časopisa *Electronics* doprineti daljem povećanju ugleda Elektrotehničkog fakulteta u Banjaluci. Zasluga za to pripada pre svega autorima radova, kojima se iskreno zahvaljujem. Bio bih ponosan ako se moja uloga gosta urednika bude tumačila kao moj doprinos tom ugledu.

P R E F A C E

I have been honored by the invitation of the Dean of Electrical Engineering Faculty in Banjaluka Prof. Dr. Branko Dokić to be a guest editor of this issue of *Electronics*, Journal of the University of Banjaluka. The Faculty of Electrical Engineering in Banjaluka has been founded by the support of many distinguished professors from the Faculty of Electrical Engineering in Belgrade. Since the founding, these professors continuously or occasionally teach graduate and postgraduate courses in Banjaluka. By the high quality of educational staff, participation in research programs, and cooperation with industry, the Faculty has achieved a creditable reputation as the Highest School of Electrical Engineering in Serbian Republic and Bosnia and Herzegovina. To these reputation significantly contributed the permanent work of the Faculty in difficult conditions of the war-stricken country.

In this issue, I included the papers by recognized researches in electronics and its applications in related areas. First article is an abridged version of the plenary paper presented at the XLII ETRAN Conference held in early June in Vrnjačka Banja. The paper has attracted the attention of many conference participants, and thus, in the near future, the original version of the paper will be published as a brochure by the Society for ETRAN. Five articles included in this issue are extended versions of invited or outstanding papers presented at the ETRAN Conference. Other papers are original scientific contributions that are first time presented to engineering community.

I hope that this issue of *Electronics* will contribute to a further growth of reputation of the Faculty of Electrical Engineering in Banjaluka. First of all, merits belong to the authors of included papers to whom I am sincerely grateful. I would be proud if my engagement as the guest editor was understood as my contribution to this reputation.

M.R. Stojić

Slobodan N. Vukosavić, *School of Electrical Engineering, University of Belgrade*

Abstract - In the past decade, electric drives with electronic speed control were advantageously used in industrial applications, appliances and automotive field. AC and DC motors in machine tools, industrial robots, automated presses, elevators, conveyers, rolling mills, compressors, pumps, fans, electrical vehicles, cranes and many other applications spend more than 2/3 of all the electric energy produced in an industrialized country. Complex tasks of the process and the motor control are performed with the help of high throughput digital controllers and subminiature signal processors capable of performing 10^8 operations per second. The frequency of the pulse width modulation in the drive power converter section is increasing steadily due to advancements in the field of high power semiconductor switches. The increase in the PWM frequency offers faster response of the current and torque control loops and improves the overall drive performance.

Most drive problems are already settled. Mature technology of electrical drives offers widely accepted solutions for the power converter topology, basic control algorithms and most of the drive functions. Therefore, no significant changes in the drive structure will take place in the years to come. A widespread use of controlled electrical drives is primarily limited by the cost of the drive package. Therefore, a significant research effort is directed towards motor and drive integration, development of low cost intelligent power devices and invention of reduced topologies of the drive power converter. The elimination of the shaft sensor and the phase current sensors contribute to the cost decrease, simplified cabling and an increased reliability of the drive. Sensorless drives call for the development of robust, nonlinear state observers and parameter estimators capable of acquiring the information on the drive states that are not directly measured. The indirect state and parameter evaluation based on the secondary phenomena such as the slot harmonics, leakage inductance modulation, and the spatially distributed saturation call for a highly evolved signal processing and the spectrum estimation techniques. The problems of sensorless drive realization attract attention of significant R/D forces all over the world.

High performance servo drives are exposed to an ever increasing demand for higher response speed and precision. The evolution of production technology and development of new tool materials require the servo loop bandwidths of well above 200 Hz. Improvements in the drive dynamic response must go with highly evolved decision making functions built into the drive software package. To shorten the installation, replacement and to speed up the production process change, the drive should be equipped with adaptation features, self commissioning procedures and the decision making routines capable of

replacing or eliminating the intervention of human operator.

This article outlines the status of technology for the drive power converters, motors, sensors, and control algorithms and gives a brief overview of the trends and perspectives in the field of digitally controlled electric drives. Pointed out are the cutting edge applications that incite further improvements of the drive performances and the advances in the motor and semiconductor technology that make such developments possible.

1. INTRODUCTION

From the beginning of this century, electric drives have been replacing fluid power actuators and IC machines in both high performance and general purpose applications, the growth of electric drives application being determined by the current level of technology. High reliability, long lifetime, relatively low maintenance and short startup times of electric drives are in consort with their ecological compatibility: low emission of pollutants. The quality of electric drives is extended by a high efficiency, low no-load losses, high overload capability, fast dynamic response, the possibility of recuperation, and immediate readiness for the full-featured operation after the drive startup. Electric drives are available in a wide range of rated speeds, torques and power, they allow for a continuous speed regulation, reversal capability, and they easily adapt to different environment conditions such as the explosive atmosphere or clean room requirements. Unlike the IC engines, electric motors provide for a ripple-free, continuous torque and secure a smooth drive operation. At present, electric drives absorb 60-70% of all the electric energy produced in an industrial country [1,2].

During the past two decades, the evolution of powerful digital microcontrollers allowed for a full-digital control of the electromechanical conversion processes taking place in an electrical drives. The process automation made significant progress in the fifties, thanks to the introduction of numerical control (NC). Although not flexible and fully programmable, NC systems replaced relays and mechanical timers common on the factory floor in the first half of the century. As the first reliable and commercially available microcontrollers were made in the sixties, they were advantageously used for the purpose of a flexible control of electric drives in production machines. As from then, the hydraulic and pneumatic actuators gradually disappear and give space to DC and AC electric motors.

Although more robust and easier to produce than the DC motors, the AC electric motors were mostly used in constant speed applications and supplied from the mains [3] until the technological breakthroughs in the early seventies.

It took the development of transistorized three phase inverters with digital PWM to provide for a variable frequency supply of induction motors. The invention of IGBT transistors and high speed digital controllers made the variable speed AC drives reliable and acceptable for the drive market. Dunfoss in 1968, produced the legendary VLT 5 frequency converter weighing 54kg, suitable for the speed regulation of 4kW induction motors (recent versions of the same converter weigh 3.5 kg [4]). Among the first applications of variable speed frequency controlled AC drives were pumps, fans and compressors, where the speed regulation feature eliminated mechanical damping of the fluid flow and reduced the associated power losses and turbulence. For their increased reliability, low maintenance, and better characteristics, the frequency controlled induction motors gradually replaced DC drives in many of their traditional fields of application. At this level, the reign of DC drives reduced to high speed servo applications.

In early eighties, the frequency controlled AC drives are widely accepted, but their prices still level those of DC drives. The cost of an AC drive package has a 30% motor + 70% power converter structure, while in the case of a DC drive the motor is worth 70% of the package cost [12]. The prices of power- and signal- semiconductors will presumably decline, while the cost of electric motors will remain tied to the copper and iron prices. For that reason, the AC drives have the perspective of decreasing the package cost, evermore cheaper than their DC counterparts. Further technological improvements are likely to make the frequency controlled AC drives the cheapest actuators ever. At present, in an industrialized country the AC drives substitute DC motors at a pace of 15% per year [1]. More than 20% of the drives are frequency controlled, while the remaining 80% operate at a constant speed.

The AC drives were used in high performance applications only after the development of the field oriented control concept. Following the introduction of space vectors [6], direct (DFOC) and indirect (IFOC) field orientation control structures were devised, also known as the vector control [7,8]. Although invented in sixties, the vector control concept was put in use only some twenty years latter [11].

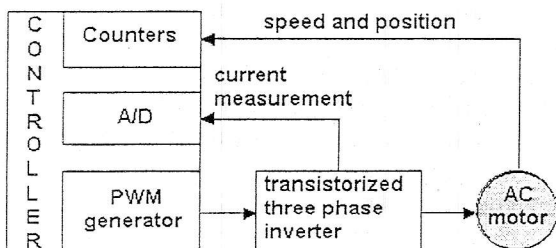


Fig.1 Basic functions of the feedback signal acquisition and the control of the power conversion process in a typical induction motor electric drive.

Numerically intensive, vector control structures required high-throughput 16/32-b digital controllers and signal processors [13]. Aside from high performance drives,

general purpose and application specific digital drive controllers are found nowadays even in commodity products. In most of high volume applications of digitally controlled electric motors, microcontroller executes both the drive control functions [15,16] and the application specific functions such as the handling of the washing, rinsing and drying in the case of modern dishwashers and washing machines. Compact digital controllers emulate the functions traditionally implemented in the analog form and allow also the execution of nonlinear and complex functions that could not have been completed by analog circuitry (ANN, nonlinear estimators, spectrum estimation and others).

The vector control concept empowered the AC machines to conquer the high performance drives market. Although effective, both the IFOC and the DFOC structures rely on motor parameters and exhibit considerable sensitivity to parameter fluctuation [17,18]. Therefore, both the DFOC and IFOC controllers must be equipped with proper means for the parameter identification [24] at the installation phase (self-commissioning) [19] and during the drive regular operation [20] (on-line tuning). Besides the adaptation routines, most applications require high performance digital current control [21] and on-line power loss minimization routines. Numerically intensive, such algorithms require the use of fast transputer networks [9,22] and digital signal processors within the drive control section. Powerful and flexible, the DSP based drive controllers [22] create the potential for significant performance increase through the application of advanced control concepts [23,25]. Highly evolved observers of the drive states allow reduction of the number of sensors. The drives with minimum number of sensors and the shaft sensorless drives are more robust and reliable than their sensed counterparts. The lack of sensors and associated cables makes the drive cheaper and the installation simpler and faster. In the development phase are the advanced parallel control structures such as the direct and incremental torque control (DTC, IncTC) that make the use of a large numerical throughput to implement a non-cascade control concept thereupon augmenting the response speed and overall drive dynamic performance.

2. ECONOMIC IMPORTANCE OF DIGITALLY CONTROLLED ELECTRIC DRIVES

The number of general purpose drives installed each year considerably exceeds the number of new high performance servo drives. According to *Frost & Sullivan Market Intelligence* data for 1997, 52.7% of new drive installations in U.K. used Tesla's induction motor, some 33.7% were the DC drives, while the remaining 13.9% corresponds to fluid power and other non-electric actuators. According to the same source, the AC drive growth in 1998. is predicted to be 3.9%. Market analysis performed 1994. in North America show that more than 90% of the motor units are in the fractional horsepower range ($P < 1$ HP). Most of the FHP motors produced in the U.S. are the universal or

single phase motors; Tesla's induction motor is less diffused than in Europe. Each year, some 550×10^6 general purpose FHP motors are produced in U.S. with the total value of $\$6.1 \times 10^9$. The number of high performance drives produced each year is much lower, but their value in the U.S. reach $\$1.06 \times 10^9$ per year.

In Europe, the three phase supply is much more accessible than in the U.S., which rouses frequent use of Tesla's induction motor. AC motors above 75kW account for 29% of European annual production, the motors rated 7.5 – 75kW correspond to 31% and the induction motors below 7.5kW are worth the remaining 40%. The AC drives expansion to home appliance field is sluggish due to extraordinary low prices required by the market. The production cost of electronic speed controlled AC drives ranging 0.5 - 1 kW must drop below \$20 threshold for the final products be competitive to their open-loop counterparts. With the present growth rate, this might happen in 2001.-2002.

The growth of high performance drives depends on the investments in new production sites. R/D efforts and production of servo drives take place in highly industrialised countries: Japan and Germany make each 25% of the world production of industrial robots and machine tools, while China produces more than 20%. *Frost & Sullivan* report on annual high performance drives growth of 5% in Europe, while *Motion Tech Trends* study predicts the servo drives sales in the U.S. to grow up to $\$4.5 \times 10^9$ in the year 2000. More than 52% of high performance drives employ Tesla's induction motors, the step motors are used in 4.2% of the cases, the DC servo motors cover 22% of the market, while the permanent magnet synchronous motors account for some 20% of the market. Relatively high cost and low volume of high performance drives make their development relatively slow with respect to general purpose drive. Lengthy and expensive R/D efforts restrain the servo drives design and production to few highly developed industrialised countries.

3. CLASSIFICATION OF CONTROLLED ELECTRIC DRIVES

Digitally controlled electric drives may be ranked according to the application, characteristics, voltage and power range, and the power converter topology. Five basic categories may be distinguished: i) High performance servo drives; ii) General purpose drives; iii) Electronic speed controlled drives in homes, offices and automotive applications; iv) Medium voltage high power drives; and v) Electric propulsion applications.

The article discusses the problems and future trends in each group of electric drives. Particular attention is paid to the motion control algorithms and to the developments in the power conversion control. Specific influence of an ever increased number crunching capability of modern digital controllers on the drive controller structures is probed deeply. Performance enhancements of semiconductor power switches are outlined and their

influence on the drive converter topology and characteristics is briefly analyzed. Finally, the needs and the possibilities are outlined for a digitally controlled drive to assume versatile adaptation and self-commissioning features [33,34], reducing in such a way the need for the operators intervention in both the installation and regular operation phases.

4. GENERAL PURPOSE ELECTRIC DRIVES

General purpose drives are mostly used in pump, fan and compressor applications (PFC) in industry and the heating, ventilation, and air conditioning (HVAC) systems in home and office buildings, and other non-servo industrial and domestic applications. The workhorse of these applications is Tesla's induction motor accompanied by the IGBT three phase inverter. Fast response of the speed loop is generally not required. Majority of applications require only a relatively slow speed adjustments to the process needs, and the motors are usually installed without the shaft sensor. Response of the speed loop can be sluggish, yet the drive is expected to provide the speed regulation in a wide range. The drive controller task is providing the stable operation at very low speeds, characterized by the supply frequencies below 1 Hz. At the same time, it is essential to support the field weakening operation up to the speeds exceeding the rated one by 2-3 times. Preferred drive characteristics are high efficiency, environmental friendliness, high starting torque, low maintenance, large mean time between failures (MTBF), simplicity of the installation, commissioning and a low cost of the drive package. Speed sensorless operation is essential for many reasons. The shaft sensor usage increases the system cost, decreases reliability and makes the cabling more complex. Moreover, sensed drives must use non-standard motors, since all the general purpose, series produced induction motors include no shaft sensors nor the means for the sensor installation. A variety of different schemes for speed sensorless operation of Tesla's induction motor have been proposed in the past decade. Most of them ensure a very good dynamic performance in a fairly large speed range.

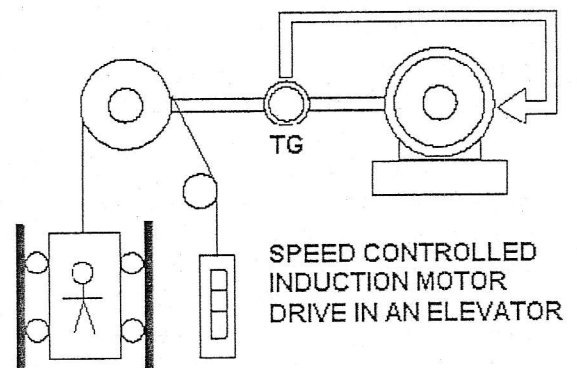


Fig.2 Speed controlled induction motor drive used in a passenger elevator

However, at low stator frequencies, performances notably deteriorate. The motor flux linkages cannot be directly measured. Instead, the states of interest are derived from the motor terminal quantities by means of motor fitted nonlinear state observers and estimators. The information on the motor flux is contained in the stator voltages as the back electromotive force. As the supply frequency drops down towards zero, the stator resistance voltage drop prevails in the terminal voltages making the flux derivation more difficult. The stator flux estimation is particularly sensitive to an inaccurate stator resistance value in the estimation model. This inaccuracy causes estimation errors both in the amplitude and the estimated angle of the stator flux vector. The flux error and variations of other machine parameters continue to impair the accuracy of the estimated mechanical rotor speed, particularly under load. The crucial parameter for the speed estimation is the rotor resistance, while a detuned value of the leakage inductance affects the flux and speed observers and estimators only to a limited extent. Lacking a conventional speed estimator with adequate performances, the shaft speed of Tesla's induction motor may be derived relying on secondary effects and the motor imperfections such as the spatial distributed saturation and the slot induced harmonics in the motor terminal quantities. The speed extraction based on the evaluation of rotor slot harmonics does permit very precise estimation in the steady state, but lacks the possibility of tracking fast changes in the rotor speed. Hence, the sensorless drive with the slot harmonics feedback is bound to have a poor dynamic performance. This is due to the very low number of rotor slots normally encountered in induction machines, which imposes severe bandwidth restrictions on the obtained speed signal. An accurate speed signal is extracted, which serves for model parameter tuning. This method requires considerable computing power, which inhibits implementation in standard microcontroller hardware. For this reason, most authors propose the additional, slot harmonic derived information be used for the parameter adaptation purposes. Provided correct values of the motor parameters, DFOC controller will secure the flux, torque and the speed control in all the general purpose drives operating modes.

5. LOW COST DRIVES IN HOUSEHOLD AND AUTOMOTIVE APPLIANCES

Many commodity products demand the motion control functionality. Some of them are the vacuum cleaners, washing machines and dish washers. Similar characteristics and the power range have the auxiliary drives in the automotive field. The servo steering, motorized windows, automated seat adjustment and active suspension systems require low cost, robust and reliable electric drives. Having the cost reduction as the primary goal, significant research resources are assigned to development of simple converter topologies [26,29], new types of electric motors [27] and algorithms for the sensorless speed control [28].

Among other requirements, electric drives in household and office appliances are expected to be

environmentally friendly; low thermal, acoustic and electromagnetic emissions are forced by government regulations and international standards. The level of the electromagnetic interference strongly depends on the power section layout and might be improved by the introduction of newly developed power switches with spatially distributed lifetime control (CAL). At the same time, the cost reduction of the power switches would give a strong incentive to a more frequent use of electronic controlled drives in the appliance field.

Power semiconductors are used within the drive converter for accurate control of the energy flow between the power source (i.e. the mains) and the motor. They have extremely short response times and low dissipation. The dramatic developments in IC technology, particularly during the last ten years, have made possible the design of modern, self-protected components, with simple, lowloss drive characteristics, wide dynamic control range, switching power levels up to the megawatt range, and a direct interface to microelectronic systems.

6. TRACTION DRIVES

Electric propulsion of autonomous, battery supplied electric vehicles (EV) such as the electric cars and buses require efficient, robust and light weight drives with fast and accurate traction effort response. The EV drive controller habitually encompasses the means for suppression of resonance modes in the transmission and the vehicle mechanical parts [29]. Simple construction of Tesla's induction motor with the squirrel cage rotor makes it an ideal candidate for advanced traction motor designs such as the linear motor (LIM) and the tubular axle induction motor (TAIM).

7. LARGE POWER, MEDIUM VOLTAGE DRIVES

Large power AC drives are found in rolling mills, petroleum industry, water supply and many other applications where the rated power exceeds 300 kW and the nominal stator voltage falling into the medium voltage range (2300, 4160 or 6600 V) [30-32]. The main problem in this class of electric drives is the design of controlled three phase variable frequency source in the megawatt range. Until recently, the variable frequency, medium voltage drives were not available due to the absence of high voltage semiconductor power switches. The need for the economic use of energy, miniaturization of electrical systems, and reactive power compensation have been the motives for the revolutionary development of high voltage, high current power semiconductors. For their high power rating, Gate turn off thyristors (GTO) are considered the main switching device for the construction of multi-level high power three phase inverters. The power losses occurring in the GTO at turnoff limit the GTO's normal operating voltage to the range from 30 to 40% of the breakdown voltage, thus limiting the dc-link voltage of a conventional GTO inverter to 1500-2500 V.

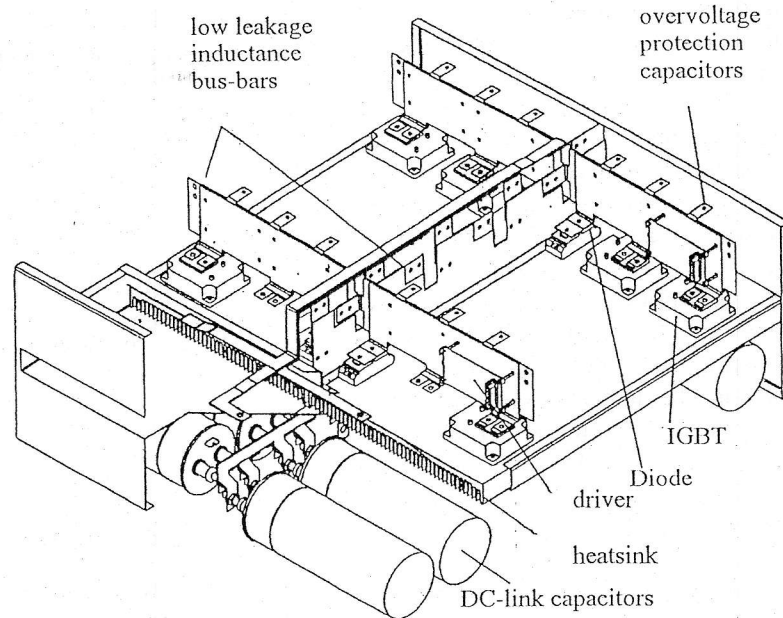


Fig.3 The three phase power converter for a 500 kW AC motor drive.

High-power inverters with dc-link voltage up to 4000 V and existing GTO's cannot be made with conventional six-switch topology. Several converter configurations for the realization of a large capacity inverter with more than 4000 V dc-link voltage are possible. One of them is the six-switch configuration with each of the switching elements being made out of several series connected GTO's. However, the direct series connection method of GTO's has the problem of blocking voltage unbalance during turn-off transient, due to the different turn-off characteristics of each device. Whenever additional equipment is used to overcome this problem, the overall system becomes more complex and expensive. Besides the circuit complexity, a limited switching frequency of GTO's causes large harmonic components of the output voltage and current. Split DC-link voltage three-level converter topologies configurations are being developed for the large capacity inverters, capable of solving the above mentioned problems. Appreciable research effort is devoted to switching rules for a multilevel inverter capable of reducing the commutation stress while maintaining at the same time an acceptable ripple amplitude and the spectral content of the output current.

8. BASIC CHARACTERISTICS OF HIGH PERFORMANCE DRIVES

High performance servo drives are used in production machines, machine tools, industrial robots, automated presses, and many other applications where the speed and position control loops are indispensable. Most frequently used are the AC induction and the permanent magnet synchronous motor drives [5],[14] with the rated power ranging from 50 W to 200 kW. Required bandwidth of the torque, speed and the position loops is roughly 1kHz,

200Hz and 60Hz respectively. Every year, the number of high performance DC drives increases by 3% while the annual growth of AC servo drives exceeds 12%.

9. THE PROBLEMS AND DEVELOPMENT TRENDS OF MOTION CONTROL ALGORITHMS

The structure of a typical motion control system includes two basic types of control functions:

- i) 'External loop' dedicated to the mechanical subsystem where the speed control, position tracking and multiple axis synchronization functions are executed. The servo motor is considered the torque actuator with a response time much faster than the mechanical subsystem dynamics;
- ii) 'Internal loop' handling the motor flux and torque control, with the drive power converter used as an actuator and the motor electric subsystem as the plant to be controlled. Control objective is making the electromagnetic torque and the flux linkage track the reference values imposed by the master (external) loop.

The internal loop is motor dependent and changes as a different type of servo actuator is used. The vector controller is the most frequently encountered controller for AC servo drives with the parameter sensitivity being the main unresolved problem. On the other hand, the external loop copes with moving the production machine tools and parts in the work space with ever higher speed and precision. The main problems of the external part of the motion controller are the transmission imperfections, the torque ripple, compliance and mechanical resonance problems, as well as rapid changes in the motion profiles and the mechanical parameters of the system.

Variable structure systems ensure sufficient robustness and guarantee the reference trajectory be reached

whatever the initial conditions. However, sustained oscillations and a permanent driving force chatter exist even in the steady state, producing a periodic space error and making the VSS inadequate for most motion control applications. Nonlinear nature of fuzzy control structures sustains some of the VSS controller robustness and suppresses the chattering problem. Based on Zadeh's set theory [38], fuzzy controllers are inherently suboptimal. Even though, in some applications [37] they can permit significant improvements in the servo loop response time.

Aiming at an increase in both the operation quality and the production volume, recent production machines require the servo loop bandwidths surpassing 200Hz. Major impetus to the servo performance increase is the torque ripple of the servo motor, the imperfection of position sensor, transmission dynamics, nonlinear friction and unpredictable cutting resistance. All of deficiencies mentioned above are deterministic and cyclical in nature, some of them having the spatial period relative to one motor turn, and the others repeating the same way within each operating cycle. In essence, the said disturbances may be predicted and compensated for, eliminating in such a way the associated space tracking error. Many of disturbance components (such as the torque ripple [43]) are nonlinear functions with multiple arguments, such arguments being the states of both the electrical and mechanical subsystem. In most cases, disturbance prediction functions depend on the operating point, temperature and change in time due to the wear and other factors. Consequently, disturbance predictor must be a very complex function with some self learning features built into the structure. Good results are achieved by the application of artificial neural networks (ANN) [39,40,41] equipped with an on-line re-training mechanism. Unpredictable in itself, an ANN is hardly used for the operation critical tasks. Rather than that, production machines employ the ANN for advanced secondary functions such as the monitoring, diagnosis, recognition of specific defects, slow adaptation and similar. In recent times [42], some authors have proposed the neuro-fuzzy match for the position tracking tasks, expecting the ANN-fuzzy marriage to bring both the fuzzy robustness and the ANN advanced self learning and adaptation features into the servo loop.

10. ELECTRIC SERVO DRIVES IN AUTOMATED PRODUCTION MACHINES

Position and speed controlled servomechanisms exhibit a significant growth in the past years. From 1994. to 1997, the value of servo actuators produced in Germany increased from 203×10^9 DM to 264×10^9 DM. This growth is followed by the introduction of new production technologies such as the pressurized injection molding, water beam and laser cutting machines.

Development of new tool materials allows for an increased cutting speeds. In turn, the spindle drives are required to reach the rotation speed above 50.000 rpm with the rated power of 10 - 20 kW. The tool servo axis and the manipulator drives are expected to track desired trajectory

with the top speed well above 100 m/min and the precision better than $0.2 - 1 \mu\text{m}$. Particular cases, such as the hard disk drive production lines, require tracking error inferior to 10 nm and use piezoelectric actuators.

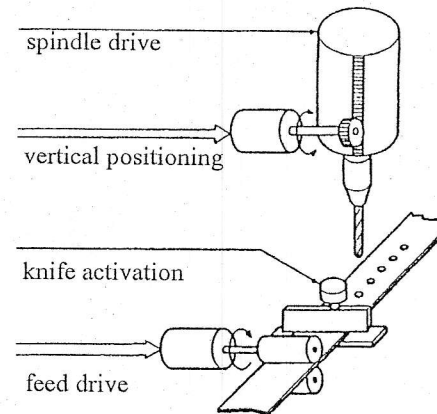


Fig.4 A typical feed drive application.

The main problem of tracking the exact tool position is the variable cutting resistance of the material. To suppress the space errors, position control stiffness of 100-1000 N/m is required in most of the cases. In some applications, such as the automated tool production and the diamond cutting, necessary stiffness might reach 10000 N/m, which cannot possibly be achieved by hydraulic and pneumatic actuators and the employment of high performance AC servo drives is required.

Many production processes require mixed force-position control in some phases of the production cycle. Industrial manipulators that clutch and move the objects must include a superimposed force control loop, in particular when grabbing and holding fragile objects like crystal glasses [35].

Secondary force control loop is needed for the purpose of stabilisation of human-like robots, which generally involves the installation of additional force and position sensors as well as the use of acceleration observers. Performance improvement of existing linear and rotary sensors and design of novel solutions attract the attention of many research engineers in the motion control field. The sales of position sensors alone have reached $\$1.7 \times 10^9$ in the U.S. Standard solutions include potentiometers, LVDT (*linear displacement to analog out*), resolvers, tachometers and optical encoders.

New-sprung position sensing techniques include interferometer-based devices with the He-Ne laser. According to recent reports, the laser sensors reach the resolution of 5 nm with 500 nm repeatability. Relatively expensive, the laser position sensors are used mostly in high productivity laser cutting machines where the sensor cost is not a hurdle. Among conventional sensors, the optical encoders are the most precise but still affordable solution. Disadvantage of absolute and incremental encoders is the temperature sensitivity of their photo sensitive semiconductor devices. In production machines, the operating temperature frequently exceeds the 125°C limit, thus precluding the usage of optical encoders. Position

measurement in dusty and oil contaminated environment is frequently performed by industrial cameras with dedicated frame grabbers and associated image processing routines.

Along with fast and precise position tracking, servo drives are expected to support the high speed digital communication protocols on the factory floor level. The CNC, sensors and servoamplifiers need the information exchange in both the installation and running phases. Fast serial link between the communication nodes allows for an easy, noise free interchange of the reference and the feedback values, inspection and change of control parameters, and flexible monitoring and diagnostic features.

11. LINEAR ELECTRIC SERVO MOTORS

Most of the operations of an automated production machine involve linear translation of machine parts, work pieces and tools. On the other hand, common electric motors are rotary electromechanical converters producing the torque at the output shaft. Transmission mechanisms such as the rack and pinion, ball screw and gear systems convert the rotary into linear motion. Dry friction, backlash, elastic coupling and the torsional resonance intrinsic to all the rotary – to – linear transducers severely limit the servo loop bandwidth.

Relatively large rotational masses constrain the peak acceleration of the system. On the other hand, large equivalent inertia filters out the torque ripple and the quantization excited ± 1 LSB torque chatter, alleviating in such a way the tracking error. Imperfection of the transmission mechanism may be eliminated by the application of direct drive concept with linear electric motors. As the tools are coupled directly to the motor moving parts, the problems of mechanical resonance exist no more. The absence of rotational masses results in a much larger peak acceleration of the overall system, while the ratio between the peak driving force and the friction increases several times when compared to a servo axis with a rotational actuator.

Contemporary linear motors exhibit the top speed of 3-5 m/s and offer the positioning accuracy down to $1 \mu\text{m}$. Exceptionally low inertia stresses the torque ripple and the

chatter related problems. Due to the motor imperfection and the finite resolution of the sensors, the driving force exhibits (the same way as the driving torque of a rotational servo motor) high frequency oscillations – the chatter – with an amplitude of 1-3 LSB. The smaller the inertia, the larger the speed and position fluctuations caused by the jitter in the driving force. Dissipativity based [36] approaches to the servo loop synthesis permit significant reduction of the chattering problems, but do not solve completely the torque/force ripple problems. For this reason, the force ripple minimization is one of the main design requirements for linear electric servo actuators.

Modern linear motors are mostly asynchronous or synchronous permanent magnet motors. They have magnetic, hydrostatic or the air bearings [44].

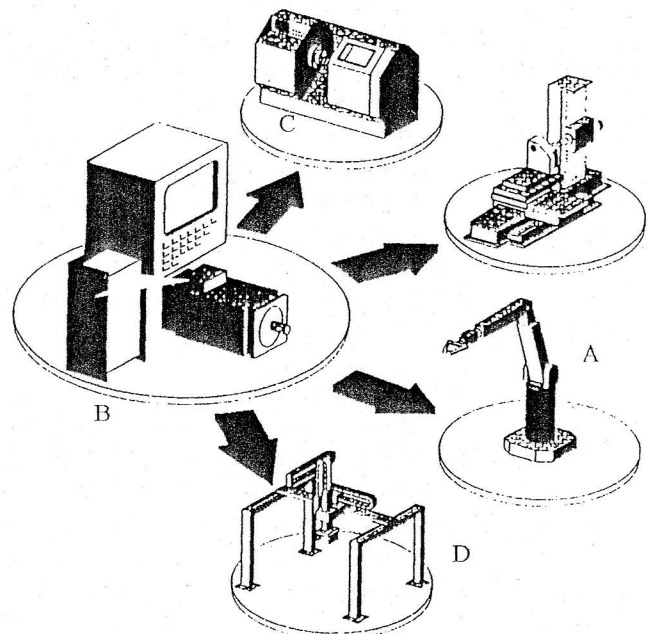


Fig.5 Position controlled drives in automated production processes: a) Industrial robot for cutting, welding and painting b) CNC, c) Machining and metal forming centre d) Gate entry.

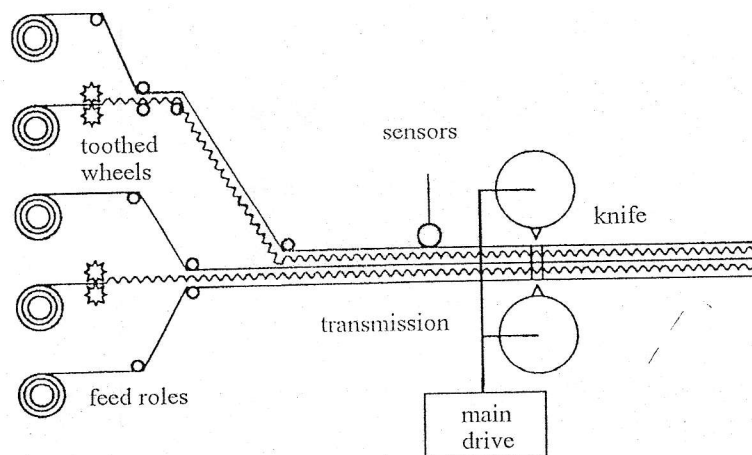


Fig.6 Application of high performance drives in paper and textile industry.

The stiffness coefficient of linear motors (200 N/m) is much better than the stiffness of the fluid power actuators (50 N/m). It is possible to move the weights above 50 kg and attain the driving forces up to 2000 N. Low equivalent inertia of motion control systems employing linear motors results in a speed loop bandwidth of 130-200 Hz and the peak acceleration well above 100 m/s².

12. THE STRUCTURE OF MODERN DIGITAL DRIVE CONTROLLERS

Digital motion controllers mostly use compact microcontrollers as the brain of the drive control hardware. Recently, digital signal processors have been introduced to the area of industrial control adding a new dimension to this field of application. Based on the Harvard architecture, DSP's are characterised by a high speed execution permitting the implementation of sophisticated control algorithms. The processor can also perform other tasks such as the real time generation of complex velocity profiles and position trajectories for multi-axis systems. The resulting design of the control hardware is simple, more flexible and more reliable. Digital implementation results in discrete time nature of compensators and involves a finite precision arithmetic. When using 8-bit and 16-bit microcontrollers, the state variables and relevant parameters are often represented as 16-b or 32-b numbers:

Software development for high precision arithmetic is neither short nor convenient, while the execution time of such programs is usually long. Due to a finite word length quantization error, the actual compensator differs from the designed one. In some recursive algorithms, even the lack of numerical stability may occur. Without a floating-point core, a designer is compelled to choose a controller structure that is least sensitive to the quantization errors and inaccurate coefficient storage. As an example, a higher order filter can be implemented as parallel or cascade combination of first and second order blocks, reducing in such a way the

response sensitivity to coefficient variations and the finite wordlength problems. Hence, even high order digital filters may be implemented on 8-b and 16-b microcontrollers, though with a limited sampling time and a large software overhead necessary to achieve required precision and numerical stability. Numeric throughput of existing general purpose 16-b microcontrollers (Table I) is not sufficient for most high performance AC drives and many sensorless, general purpose drives. The vector control alone requires several transformations of the voltage and current vectors from the d-q synchronous to α - β stationary frame. Parameter estimation and the state observers parallel to the flux, speed and position control may require more than 10⁷ operations per second, exceeding several times the capability of a conventional CPU [11].

Reduced execution time owed to the hardware implemented multiply-accumulate operations along with long 16/32-b words and the instruction set suitable for digital signal processing make the DSP based (see Table I) microcontrollers the prime candidates for the execution of the drive control tasks. Presently, several compact DSP - based microcontrollers exist, fitted with on-board peripheral modules needed for the drive signal acquisition and control. Many of them [21] allow for a numerical throughput of 20-40 x 10⁶ operations per second. Although very high, even such levels of the number crunching capability are insufficient for the implementation of recent nonlinear state estimators based on the parametric spectrum estimation techniques. The requirements of time critical, numerically intensive drive control functions might be fulfilled by the use of the latest parallel architecture signal processors [22], capable of executing more than 10⁹ instructions per second. Though, the price and the noise sensitivity of the said DSP chips prevents their use within the drive control hardware. Instead, in numerous high performance drive designs the fastest control functions are executed in digital hardware based on flexible, high gate density with FPGA chips (Fig. 8).

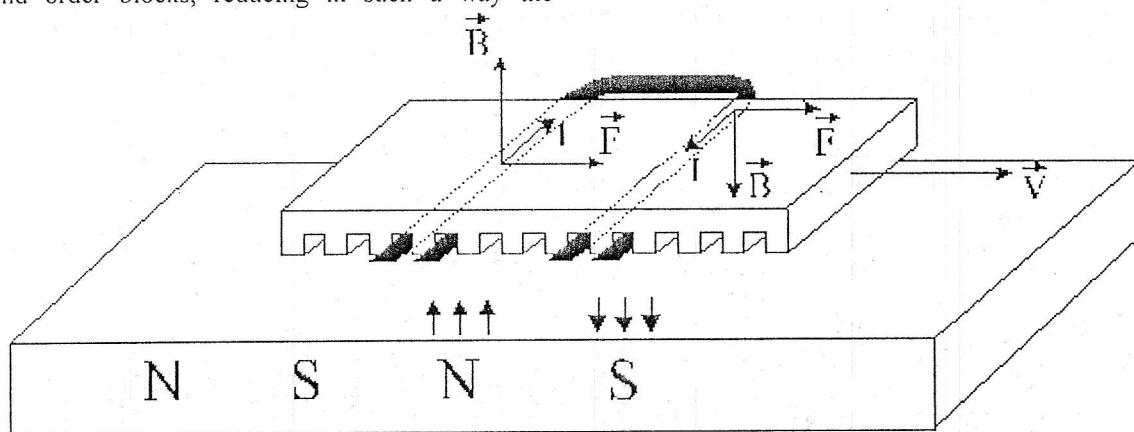


Fig.7 Linear induction motor: The driving force is generated through electromagnetic interaction between the current carrying conductors in the moving part and the currents induced in the conductive base.

13. CONCLUSION

Digitally controlled electric drives have reached mature phase in their development. The increased use of microelectronics in power control circuits enables the implementation of complex control concepts, allowing the production of environmentally acceptable, self optimized motor drives with applications ranging from precision machine tools to traction drives with Tesla's induction motor in high-speed passenger trains. Many elements and modules of the drive system are already consolidated; widely accepted solutions exist for the power converter topology, motor types and basic control structures. These well tested solutions are unlikely to undergo significant changes in the years to come.

The research and development efforts are directed towards the remaining drive problems, where substantial contributions are expected in the future. Some of these problems are:

- i) Present drives radiate relatively high levels of electromagnetic, acoustic and thermal pollution;
- ii) The drives use a large number of sensors, the wiring and cabling is fairly complex and the cost of the drive package is still excessive for most applications;
- iii) Elaborate installation and commissioning make the human operator inevitable in the startup, repair, replacement and run-time situations.

The international EMI regulations and problems with electromagnetic compatibility will incite the changes in the front end converter topology. At present, the front end converter in most of the drives is a six-pulse diode rectifier absorbing a distorted, nonsinusoidal currents from the mains.

In the future, full bridge synchronous rectifiers and other PFC topologies will be used at the drive front end. Novel front end topologies are expected to draw the sinusoidal currents from the mains, enable the regenerative braking of the drive and provide for the reduction of the DC-link filtering components.

Integration of the drive power converter into the motor frame allows for a significant cost reduction and more simple installation and wiring. With an integrated motor-converter package, the motor cable exists no more. The cable capacitance, electromagnetic radiation and the reflections of the dV/dt wave are cleared away, reducing greatly the problems of the EMI and an early breakdown of the motor insulation. To make the integration concept applicable in the field, it is indispensable to solve complex thermal management problems of the integrated drive package. At the same time, the semiconductor technology is to provide for the power and signal processing devices that can operate safely at motor case temperatures.

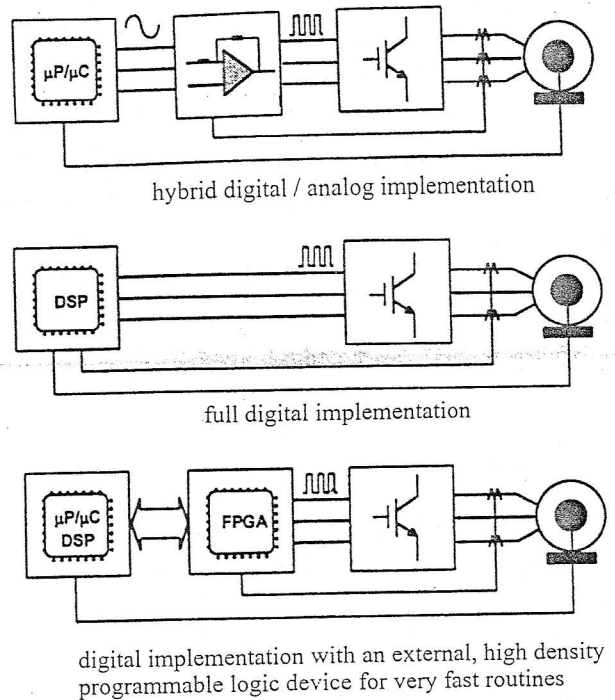


Fig.8 Evolution of digital drive controllers from analog to fully digital implementations.

The drive capacity to accommodate to the process and parameter changes without the intervention of the operator become ever more significant. In addition to slow adaptation features, most demanding applications of servo drives must possess the robustness with respect to abrupt changes in the system parameters and operating conditions. Performance criteria such as the cycle time, position tracking error, the servo loop bandwidth or some other synthetic performance function must be maintained even with the motor and process parameters changing in an arbitrary way within prescribed boundaries. Novel motion control solutions that might emerge in the years to come will have a direct influence on the work quality and the productivity of automated production machines. Local intelligence built into the drive might simplify and speed up the installation and commissioning. Providing the drive with self-adjustment and decision making routines, the interventions of human operator might be cut down to a minimum. In this way, electrical drives on the factory floor will start replacing the workers brains and not only the muscle.

Although with a mature technology and the basic problems already solved, controlled electrical drives are still in the intense development phase. Numerous control problems and the problems of energy conversion yet need to be solved. The said problems will attract the attention of many young engineers world-wide at Universities, research laboratories and companies involved in controlled electrical drives development and production.

TABLE I: Typical operations encountered in a control routine: DSP versus μC

Operation:	Digital controller:	TMS320C25	80C196MC-20
Multiply and accumulate		0.5 μs	4 μs
Speed derivation from the encoder pulse width		777 μs (*)	382 μs
Speed derivation from the encoder pulse count		2356 μs (*)	25 μs
(3 x 3) matrix multiplication		14,7 μs	225.9 μs
PID with D-action low pass filtering		0.9 μs	13.5 μs
Band-stop filter – Notch filter		2.3 μs	87 μs
(*) TMS320C25 has no peripherals needed for the pulse width and pulse count measurement. Instead, it is assumed that the DSP emulates the said functions in software.			

14. LITERATURE

- [1] V. R. Stefanović: "Present trends in Variable Speed AC Drives", in Conf. Rec. of IPEC 1983, pp. 438-449
- [2] B.K. Bose, (Editor) "Adjustable AC Drives", IEEE Press 1981.
- [3] I. Boldea and S.A. Nasar, "Vector control of AC Drives", CRC Press, 1992.
- [4] DBC drives data sheet, Vickers Elge, Settimo Milanese, Italy, 1993.
- [5] "FASK permanent magnet servo motors data sheets", Vickers Polymotor 1992.
- [6] Kovacs, K.P.; Racz, I.: "Transiente Vorgänge in Wechselstrommaschinen", Budapest, Publishing House of the Hungarian Academy, of Sciences 1959.
- [7] Hasse, K.: "On the dynamics of speed controlled static AC drives with squirrel cage induction machines", Ph.D. Dissertation, Technische Hochschule Darmstadt, 1969.
- [8] Blaschke, F.: "Das verfahren der feldorientierung zur regelung drehfeld maschinen", Ph.D. Dissertation, TU Braunschweig, 1974.
- [9] Y.Y Tzou, H.J. Hsu, "FPGA Realization of Space – Vector PWM Control IC for Three-Phase PWM Inverters", IEEE Trans. On Power Electronics, vol.12, No. 6, Nov. 1997, pp. 953-963
- [10] Leonhard, W.: "Adjustable Speed AC Drives", Proceedings of the IEEE, vol. 76, No 4, April 1988, pp. 455-471
- [11] Gabriel, R.; Leonhard, W.; Nordby, C.J.: "Field Oriented Control of a standard AC motor using Microprocessors", IEEE Trans. on Ind. Appl. vol. IA 16, No 2, March/April 1980, pp. 186-192
- [12] Lipo, T.A.: "Recent progress in the Development of Solid State AC Motor Drives", IEEE Trans. on Power Electronics, vol. PE3, No 2, April 1988, pp. 105-117
- [13] Gabriel, R.; Leonhard, W.: "Microprocessor Control of Induction Motors", in Conf. Rec. of IEEE ISPC, 1982, pp. 385-394
- [14] Lessmeier, R.; Schumacher, W.; Leonhard, W.: "Microprocessor controlled AC ServoDrives with Synchronous or Asynchronous Motors: which is preferable?", IEEE Trans. on Ind. Appl. vol. IA 22, No 5, Sept./Oct. 1986, pp. 812-819
- [15] B.K. Bose "Power electronics and AC drives", Prentice Hall 1986.
- [16] R.W. De Doncker and D.W. Novotny, "The Universal Field Oriented Controller", IEEE-IAS Conf. Rec. 1988, pp. 450-456
- [17] Miles, A.R.; Novotny, D.W.: "Transfer Functions of the Slip Controlled Induction Machine", IEEE Trans. on Ind. Appl. , vol. IA 15, No 1, Jan/Feb. 1979, pp. 54-62
- [18] Guisatski, U.M.: "Structure and dynamic characteristics of CSI induction motor drive", Proc. of the ICEM , Part 1, Budapest, 1982, pp. 199-202
- [19] Wang, C.; Novotny, D.W.; Lipo, T.A.: "An Automated Rotor Time Constant Measurement System for Indirect Field Oriented Drives", IEEE Trans. on Ind. Appl, vol. IA 24, No 1, Jan./Feb. 1988, pp. 151-159
- [20] Krishnan, R.; Doran, F.C.: "A method of Sensing Line Voltages for Parameter adaptation of Inverterfed Induction Motor Servo Drives", *ibid*, pp. 617-622
- [21] "TMS320F240 DSP Users manual", Texas Instruments 1997.
- [22] Digital signal processing solution: TMS320C62XX Technical brief, Texas Instruments, January 1997.
- [23] N.J. Kim, H.S. Moon, D.S. Hyun, "Inertia Identification for the Speed Observer of the Low Speed Control of Induction Machines", IEEE Trans. On Industry Applications, vol. 32, No. 6, Nov/Dec. 1996. pp. 1371-1379
- [24] M.Y. Chow "Methodologies of using Artificial Neural Network and Fuzzy Logic Technologies for Motor Incipient Fault Detection", World Scientific Publishing Co Pte, Ltd, 1997.
- [25] Discussion with Jelena Popović, assistant lecturer, Department of Electronics, ETF-Belgrade, April 1998.
- [26] Asymmetrical 6/2 SR drive, ACORN - European Washer Project, Emerson Electric Co, Electronic Speed Control Division, St. Louis U.S.A. 1988.
- [27] S. N. Vukosavić: "Third harmonic comutation control system and method", USA Patent 4912378, March 27, 1990

- [28] Philip C. Kjaer and Gabriel Gallegos-Lopez, "Single-sensor Current Regulation in Switched Reluctance Motor Drives" in Conf. Rec. of IEEE IAS Annual Meeting 1997.
- [29] M. Chis, S. Jayaram, R. Ramshaw, K. Rajashekara, "Efficiency Optimization of EV Drive Using Fuzzy Logic" in Conf. Rec. of IEEE IAS Annual Meeting 1997.
- [30] V. Stefanović, D. Borojević, *Current Problems in Industrial Drives*, in Proc. VIII Conference Energetska elektronika - Ee'95, Novi Sad, Serbia, Yugoslavia, 1995.
- [31] A. Nabae, I. Takahashi, H. Akagi, "A New Neutral-Point-Clamped PWM Inverter," IEEE Trans. Ind. Applications, vol. IA-17, No. 5, pp. 518-523, Sep./Oct. 1981
- [32] R. Joetten, Chr. Kehl, "A fast space-vector control for a three level voltage source inverter," Conf. Proc. EPE '91 (Firenze), vol. 2, pp. 70-75, 1991.
- [33] A. Barazzouk, A. Cheriti and G. Olivier "A Neural Networks Based Field Oriented Control Scheme for Induction Motors", in Conf. Rec. of IEEE IAS Annual Meeting 1997.
- [34] Kenji Inoue, Junji Yoshitsugu, Shin Shirogane, Prasanna Boyagoda, and Mutsuo Nakaoka "Automatic Learning Control-Based Gain Parameter Auto-Tuning Scheme for AC Servo System" in Conf. Rec. of IEEE IAS Annual Meeting 1997.
- [35] "DBM041 application in Verrerie Cristallerie d'Arc (F)", VESTAR 003/1998, publication of Vickers Electric, Casella (GE), Italy.
- [36] V. Davidkovich, A. M. Stankovic and G. Tadmor "Analysis and Experiments with Dissipativity-Based Control of PM Synchronous Motors" in *Conf. Rec. of IEEE Industrial Applications Society Annual Meeting 1997*.
- [37] C.Y. Won et. al. "New Fuzzy-Sliding Mode Controller for Position Control of Induction Motors", IEEE-IECON Conf. Record 1993, pp. 115-121
- [38] L.A. Zadeh, "Fuzzy Sets", *Information & Control*, vol. 8, No. 3, 1965, pp. 338-353
- [39] M.A. El-Sharkawi et.al. "High performance drive of brushless motors using neural networks" *IEEE Tran. on Energy Conversion*, vol. 9, No. 2, June 1994, pp. 317-322.
- [40] M.G. Simoes and B.K. Bose, "Neural Network Based Estimation of Feedback Signals for a Vector Controlled Induction Motor Drive", *IEEE Trans. on Ind. Applications*, vol. 31, No. 3, May-June 1995.
- [41] H.M. Tai et al, "A Neural Network Based Tracking Control", *IEEE Trans. on Ind. Electronics*, vol. 39, No. 6, Dec. 1992, pp. 504-510.
- [42] Bimal K. Bose and Nitin R. Patel, "A sensorless stator flux oriented vector controlled induction motor drive with neuro-fuzzy based performance enhancement", in *Conf. Rec. of IEEE IAS Annual Meeting 1997*.
- [43] S.O. Bogosyan, M. Gokosan, "Adaptive torque ripple minimization of permanent magnet synchronous motors for direct drive applications", in *Conf. Rec. of IEEE IAS Annual Meeting 1995*, pp. 231-237
- [44] Stephen L. Hero, Dover Instrument, PCIM 1991, Nov. 1991, pp. 39 - 42.

An extended version of this paper has been presented as a plenary paper at the XLII ETRAN Conference, Vrnjačka Banja, June 2-5, 1998.

THE BASIC MOVING AVERAGE ALGORITHM OF PRESET COUNT DIGITAL RATE METERS

Aleksandar Koturović, Vojislav Arandjelović, Radomir Vukanović
Institute of nuclear sciences - Vinča, Beograd

Abstract - The dynamic parameters: response time and steady-state fluctuations of a specific preset count digital rate meter algorithm have been determined. It is shown that the response time of this algorithm is always shorter than that of the classical weighted moving average preset count algorithm. The steady-state fluctuations of successive results of this algorithm are considerably lower than those of the classical weighted moving average algorithm. This makes this algorithm particularly applicable in practice.

I INTRODUCTION

The investigations of the preset count algorithms of digital rate meters carried out so far [1,...,4] have considered classical algorithms based on k ($k=1,2,\dots$) "pulse packages" (N, T_i), each package containing N pulses counted during measurement time T_i . Formation of a package required that the preset count was reached. The parameters defining dynamic behaviour of this class of algorithms: response time, steady-state fluctuations, and the associated relations identifying mutual relations between different algorithms have been determined.

The present article deals with an algorithm from the class of moving average preset count algorithms identified as the basic algorithm in this class since all algorithms considered so far could be derived as special cases of this one. This algorithm has been mentioned earlier [5] only as a possible rate meter algorithm since the implementation of this possibility by the technology available at that time was far too complicated. The present day technology, however, offers software/hardware functional solutions and this algorithm has become interesting for implementation.

For the purpose of assessing the dynamic properties of the algorithm the parameters defining its dynamic behaviour will be determined. Furthermore, the dynamic properties of this algorithm will be compared with those of the classical preset count weighted moving average algorithm [3].

II THE DEFINITION OF THE ALGORITHM

Let N be a selected preset count for determining the mean count rate on the basis of the lengths of time intervals, T_n , required for attaining the preset count. The peculiarity of the algorithm is the manner of specifying the measurement interval within which the preset count, N , is attained. Namely, after the first N pulses defining the first measurement interval, each subsequent pulse determines new measurement interval by rejecting the subinterval associated with the first pulse of the "pulse package" and by adding the subinterval associated with the new pulse. This manner of specifying measurement intervals is illustrated by Fig. 1.

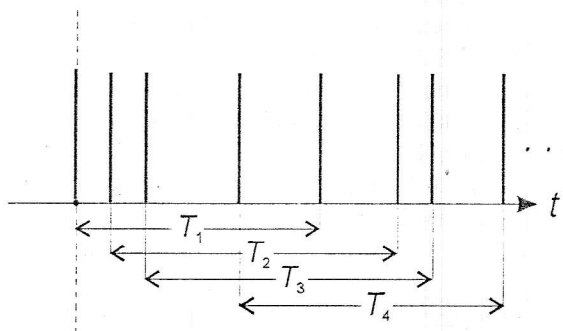


Figure 1. The schematic presentation of the manner of specifying measurement intervals

The n -th measurement interval, ending with the n -th pulse, will be

$$T_n = \sum_{i=1}^N \delta T_{n-(i-1)}, \quad (1)$$

where the subinterval δT is the time between two adjacent pulses.

The mean count rate after n measurement intervals is

$$R_n = \frac{N}{T_n}, \quad (2a)$$

where T_n is specified by Eq.(1). The mathematical definition of the algorithm is thus

$$R_n = \frac{N}{\sum_{i=1}^N \delta T_{n-(i-1)}} \quad (2b)$$

The present considerations will be restricted to the canonical form of the algorithm ($k=1$), i.e. without averaging the last k measurement results ($k=2,3,\dots$), the method commonly used in classical moving average algorithms [1,...,4]. This restriction has been introduced since the averaging process may introduce a weighting function whose influence can be the subject of separate investigations.

It is intuitively clear that this algorithm offers potentially faster response time compared to that of the corresponding classical algorithm since the whole transient will have to end within N pulses, whereas any classical algorithm involves transient times of at least several measurement intervals each containing N pulses. It may also be presumed that the fluctuations of two subsequent results will be less pronounced with this algorithm compared to those of any classical algorithm. This presumption is based on the fact that the difference between two successive measuring intervals is the difference between the contributions to the measurement interval of the rejected and the new subintervals, $\delta T_i - \delta T_{N+i}$.

III THE RESPONSE TIME ANALYSIS

Let a steady-state mean count rate suddenly changes from an initial count rate R_0 to a new steady-state count rate R_s . Figure 2. shows schematically the reaction of the algorithm to this change and introduces the variables

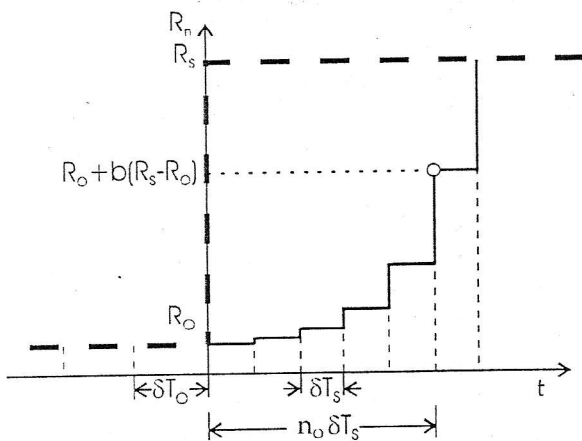


Figure 2. The schematic presentation of the transient of the algorithm for $N=5$

used in this analysis. It has been assumed that $R_s > R_0$, and that the sudden change of the mean count rate is coincident with the start of the first

subinterval of the new steady-state mean count rate, R_s . This second assumption does introduce a small error in these calculations, but for sufficiently large N the contribution of a single subinterval to the overall result is very small. On the other hand this assumption makes the following analysis considerably simpler. The parameter b ($b < 1$) involved in illustrating the transient time of the algorithm in Fig.2 determines the portion of the total count rate change taken for definition of the response time. In the present calculations the value $b = 1 - 1/e = 0.63212$ (e - the base of natural logarithms), common in health physics instrumentation, has been used.

Fig. 2 shows that the response time is reached after n_0 input pulses, counting from the moment of the change of the mean count rate, i.e. when count rate $R_0 + b(R_s - R_0)$ is reached. The figure shows the ideal case when the above criterion is exactly satisfied by the n_0 -th pulse.

In the course of determination of the response time the following approximation is used

$$\sum_{i=1}^N \delta T_i \cong N \cdot \frac{1}{R_s} \quad (3)$$

i.e. it has been assumed that N is sufficiently large that the total length of N subintervals can be approximated by N mean subintervals $\delta T_s = 1/R_s$, or $\delta T_0 = 1/R_0$, as shown in Fig. 2.

After the change of the mean count rate, the current value of the count rate during transient is

$$R_n = \frac{N}{(N-n)T_0 + nT_s} \quad (4)$$

From Eq.(4) it is straightforward to show that the stair-like curve of Fig.2 follows a continuous hyperbola

$$r_t = \frac{1}{1/R_0 + t(1 - R_s/R_0)/N} \quad (5)$$

After n_0 pulses, i.e. at the moment of reaching the criterion $R_0 + b(R_s - R_0)$, the equivalent of Eq.(4) is

$$\frac{N}{(N - n_0) / R_0 + n_0 / R_s} \geq R_0 + b(R_s - R_0), (6)$$

where the use of approximation (3) for writing the left-hand side of Eq.(6) is evident. The inequality sign in (6) is used because for $n=n_0$, the criterion $R_0 + b(R_s - R_0)$ can only by chance be exactly met when the equality sign applies.

From (6), after rearrangement:

$$n_0 \geq \frac{N b R_S}{R_0 + b(R_S - R_0)} \quad (7)$$

Therefore, n_0 is the lowest integer satisfying inequality (7). Even though all relations have been derived assuming a step-up change of the count rate, these relations are also applicable for any step-down change of the count rate.

In accordance with approximation (3), the response time of the algorithm is

$$\tau_0 = n_0 \frac{1}{R_S} \quad (8)$$

Figure 3. shows the response time dependence on the ratio $q=R_0/R_S$ for two different sets of values (N, R_0) .

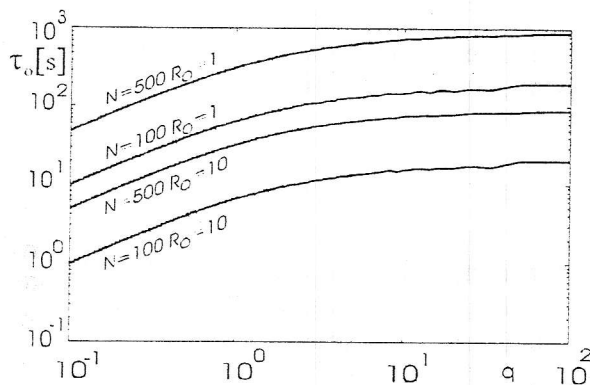


Figure 3. The response time dependence on ratio q for different preset counts (N) and initial count rates (R_0)

As expected, Fig.3 illustrates that the response time of the analyzed algorithm is directly proportional to the increase of the preset count (N) and inversely proportional to the initial count rate (R_0). The explicit dependence of τ_0 on R_S in Eq.(8) illustrates the known adaptability of this class of algorithms to count rate increases.

It is interesting to compare the dynamic properties of the present algorithm, the response time and steady-state fluctuations, to the corresponding properties of the classical preset count weighted moving average algorithm [3]. The selection of this algorithm for comparison does not exclude taking for comparison some other algorithms previously analyzed [2].

Figure 4. illustrates the response times of the present and the classical weighted moving average algorithms as functions of the ratio $q=R_0/R_S$, taking the preset count and initial count rate as parameters. Evidently, the response time of

the analyzed algorithm, τ_0 , is always shorter than that of the classical weighted moving average algorithm, τ_w . In the case of count rate decrease ($q > 1$) this difference becomes orders of magnitude big, whereas for count rate increase this difference stabilizes at a factor of approximately 2 in favor of the analyzed algorithm.

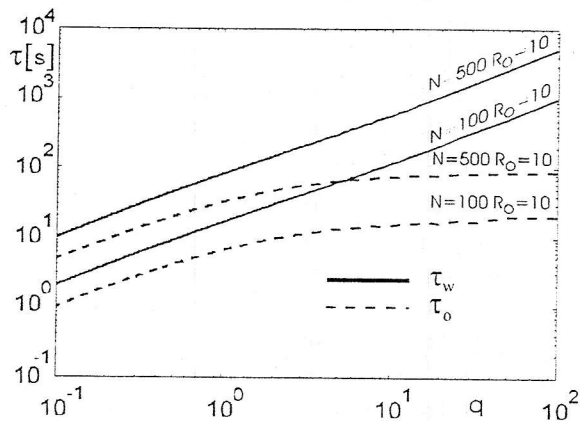


Figure 4. A comparison of the basic and classical weighted moving average ($k=1$) algorithms for different preset counts and different initial count rates

IV STEADY-STATE FLUCTUATIONS

For any preset count algorithm the steady-state statistical fluctuations of the measurement results are expressed as the fractional standard deviation $1/\sqrt{N}$ [6] (where N denotes a selected preset count). Since N is a constant for the measurement, the preset count algorithms are often called the constant accuracy algorithms.

It should be expected that the fluctuations of two subsequent results obtained by the present algorithm are considerably smaller than the total fluctuations since two subsequent results contain $N-1$ identical subintervals. Standard calculations showed that these fluctuations were given by $\sqrt{2}/N$. For a classical preset count algorithm, assuming $k=1$, the fluctuations of two subsequent results are given by $\sqrt{2/N}$. Obviously the fluctuations of subsequent results of the present algorithm are considerably smaller. This makes the present algorithm very attractive, particularly if the results have to be monitored by a visual display or if the measuring system is to be incorporated in an automatic control loop.

V CONCLUSIONS

The results presented in this article could be summarized as follows:

- the mathematical expressions for the dynamic parameters of the basic preset count moving average algorithm have been obtained;
- the response time of the analyzed algorithm is always shorter than that of the classical weighted moving average algorithm; this difference amounts orders of magnitude for step-down changes of the count rate;
- the steady-state statistical fluctuations of adjacent results are far less pronounced for the present algorithm compared to any preset count moving average algorithm;
- in general, the dynamic parameters of the present algorithm are superior compared to the corresponding parameters of any preset count moving average algorithm; these properties make the present algorithm potentially very useful in practice.

VI BIBLIOGRAPHY

1. A. Koturović, V. Arandjelović, The dynamic parameters of preset count digital rate meters, Proc. of the XL Conference for ETRAN, Vol. I, Budva, 1996, pp. 97-99 (in Serbian).
2. A. Koturović, V. Arandjelović, R. Vukanović, The moving average algorithms in digital rate meters, Proc. of the XLI Conference for ETRAN, Vol. I, Zlatibor, 1997, pp. 57-60 (in Serbian).
3. V. Dj. Arandjelović, A.M. Koturović, R.B. Vukanović, The dynamic properties of the preset count digital rate meter algorithms, Rev. Sci. Instrum., (accepted for publication in Vol. 69, No. 8, 1998).
4. V. Arandjelović, A.Koturović, The dynamic properties of digital rate meters, Proc. of the XLII Conference for ETRAN, Vrnjačka Banja, 1998 (invited paper) (in Serbian).
5. C.H. Vincent, Speed and random fluctuations in the inverse time interval type of linear rate meter, Nuclear Instruments and Methods 29 (1964), pp.337-340
6. G.F. Knoll, *Radiation Detection and Measurement*, John Wiley & Sons (1979), p.141

An abridged version of this paper has been presented as an invited paper at the XLII ETRAN Conference, Vrnjačka Banja, June 2-5, 1998.

THE GATE LEAKAGE INFLUENCE TO THE MESFET NOISE MODELING

Bratislav Milovanović, Vera Marković, Nataša Maleš-Ilić,
Faculty of Electronic Engineering, University of Niš, Yugoslavia

Abstract - A new model for MESFET noise parameter prediction including gate-leakage current influence is proposed in this paper. Starting from the previously developed model with two correlated noise sources and three corresponding equivalent temperatures, the noise effect of gate-leakage current is included by using extended intrinsic equivalent transistor circuit and four equivalent temperatures. A set of equation describing the noise parameters as the functions of equivalent circuit elements as well as fourth equivalent temperatures is derived. The procedure is implemented within the circuit simulator Libra.

INTRODUCTION

Microwave FET transistors (MESFET, HEMT) can be characterised by four noise parameters: magnitude and angle of optimum reflection coefficient Γ_{opt} (or, alternatively, by real and imaginary part of optimum admittance Y_{opt}), minimum noise factor F_{min} and noise resistance R_n .

In low noise microwave circuit design, the possibility to determine the transistor noise parameters using appropriate models and standard microwave software tools presents an useful alternative to suffering and expensive experimental characterisation of transistor noise.

In the previous work [1], [2] the authors of this paper have developed a procedure for efficient noise prediction of microwave FET transistors, starting from Pospieszalski's noise model [3] which is based on using two equivalent temperatures, T_g and T_d . With the aim to make a further improvement in modeling, the authors have included the correlation between two noise sources by defining the third equivalent temperature $T_c = |T_c| e^{j\phi_c}$, [4]. The developed procedure has been used for successful MESFET noise modeling by commercially available circuit simulators Libra [5].

However, in the most cases, the characteristics of simulated noise parameters do not agree very well with measured noise parameters at low part of corresponding frequency range. Some theoretical

investigation and experimental results have demonstrated that a gate-leakage current strongly affects the noise performance of microwave FET transistors, especially at low frequencies [6]. The established noise models are not able to describe the noise contributions of microwave FET transistors caused by the gate current. However, the successful design of some circuits, as for instance of low noise amplifier (LNA) at frequencies up to 10 GHz, requires a noise model which takes into account this additional effect. With the aspect to this, a model including the additional noise source between gate and source of microwave transistor was suggested in [6], but correlation effect between gate and drain noise sources has not been taken into account.

A new model for MESFET and HEMT noise parameter prediction including gate-leakage current influence is proposed in this paper. Starting from the previously developed model with two correlated noise sources and three corresponding equivalent temperatures, the noise effect of gate-leakage current is included by using extended intrinsic equivalent transistor circuit and four equivalent temperatures. A set of equation describing the noise parameters have been derived and implemented within standard circuit simulator.

NOISE PARAMETER EXPRESSIONS INCLUDING GATE-LEAKAGE EFFECT

Complete transistor equivalent circuit including parasitic elements is chosen in the form shown in Fig.1. The intrinsic equivalent circuit is shown in Fig.2. The gate current influence is presented by adding a shunt conductance G_p between gate and source. The noise sources in this extended intrinsic equivalent circuit are the resistance r_{gs} and conductances g_{ds} and G_p . The noise contribution of the resistance r_{gs} is modeled by a voltage noise sources e_{gs} , of the conductance g_{ds} by a current source i_{ds} , and of G_p by a noise current i_p . It is assumed that there exists a correlation between the sources e_{gs} and i_{ds} which is characterised by ρ_c .

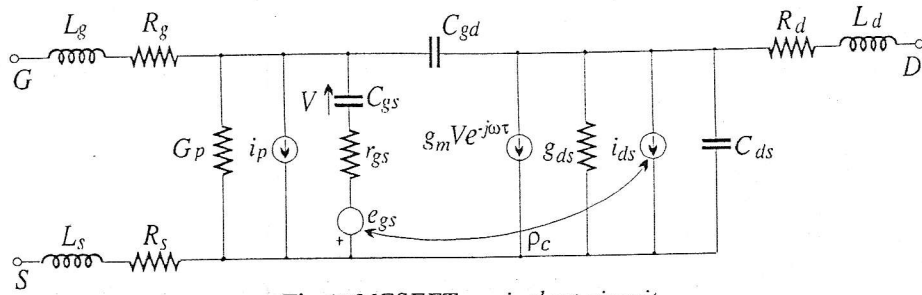


Fig.1. MESFET equivalent circuit

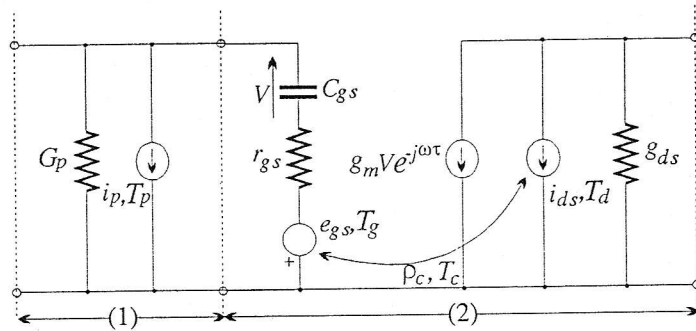
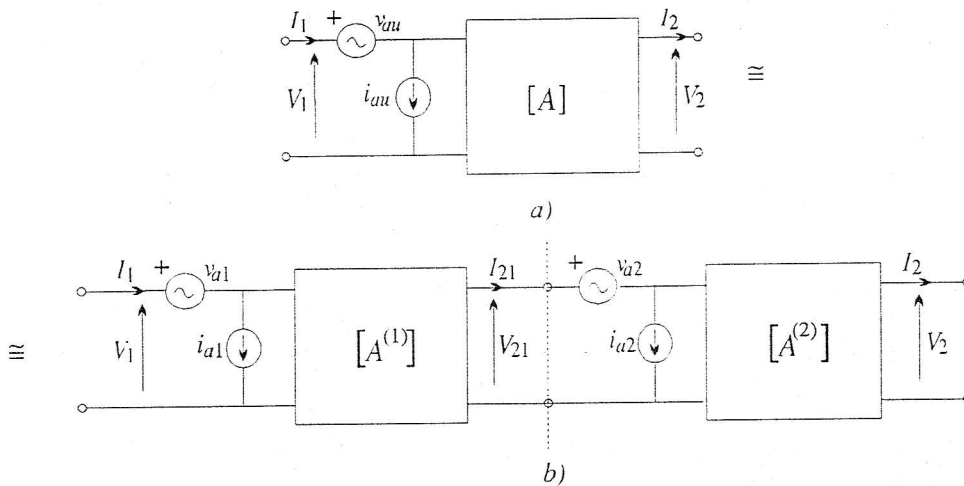


Fig.2. Extended intrinsic MESFET equivalent circuit



SI.3. "A" representation of noisy two-port circuit

a) complete circuit, b) cascade connected two two-port circuits

The equivalent temperatures T_g and T_d are assigned to the noise sources e_{gs} and i_{ds} , respectively and the correlation effect is expressed by an equivalent correlation temperature T_c , so that:

$$\langle |e_{gs}|^2 \rangle = 4kT_g r_{gs} B, \quad (1)$$

$$\langle |i_{ds}|^2 \rangle = 4kT_d g_{ds} B, \quad (2)$$

$$\langle e_{gs} i_{ds}^* \rangle = \rho_c \sqrt{\langle |e_{gs}|^2 \rangle \langle |i_{ds}|^2 \rangle} = 4kT_c B, \quad (3)$$

where k is Boltzmann constant, B is incremental bandwidth and $\langle \rangle$ represents time average.

The noise contribution of the conductance G_p is expressed through the equivalent temperatures T_p in the following way:

$$\langle |i_p|^2 \rangle = 4kT_p G_p B. \quad (4)$$

With the aim to derive the noise parameter expressions, intrinsic transistor equivalent circuit is considered as a cascade connection of two-port subcircuits (1) and (2) as denoted in Fig.2. It is convenient to represent the cascade connected noisy circuits by chain ("A") representation. In this case, two noise sources: voltage source v_{au} and current source i_{au} are assigned at the input port of noiseless circuit, Fig.3a). The chain

representation of subcircuits (1) and (2) are presented in Fig.3b).

The noise analysis of two cascade connected circuit is based on determining the correlation matrix of entire circuit C_{au} [7]. For this purpose, it is necessary to know the chain matrix $A^{(1)}$ and the noise correlation matrix $C_a^{(1)}$ of the first subcircuit as well as the correlation matrix $C_a^{(2)}$ for the second subcircuit. The resulting correlation matrix C_{au} can be compute according to:

$$C_{au} = A^{(1)}C_a^{(2)}(A^{(1)})^\# + C_a^{(1)}, \quad (5)$$

where $\#$ denotes transpose and conjugate matrix.

Considering the circuit shown in Fig.2, the matrices in the expression (5) have the following form:

$$C_{au} = \begin{bmatrix} C_{a11} & C_{a12} \\ C_{a21} & C_{a22} \end{bmatrix} = \frac{1}{4kBT_o} \begin{bmatrix} \langle |v_{au}|^2 \rangle & \langle v_{au}i_{au}^* \rangle \\ \langle i_{au}v_{au}^* \rangle & \langle |i_{au}|^2 \rangle \end{bmatrix}, \quad (6)$$

$$A^{(1)} = \begin{bmatrix} 1 & 0 \\ G_p & 1 \end{bmatrix}, \quad (7)$$

$$C_a^{(1)} = \frac{1}{4kBT_o} \begin{bmatrix} 0 & 0 \\ 0 & \langle |i_{a1}|^2 \rangle \end{bmatrix}, \quad (8)$$

$$C_a^{(2)} = \frac{1}{4kBT_o} \begin{bmatrix} \langle |v_{a2}|^2 \rangle & \langle v_{a2}i_{a2}^* \rangle \\ \langle i_{a2}v_{a2}^* \rangle & \langle |i_{a2}|^2 \rangle \end{bmatrix}. \quad (9)$$

In the relations above, the temperature T_o represents ambient temperature (290 K).

The noise parameters of intrinsic transistor circuit can be determined knowing elements of complete circuit correlation matrix C_{au} by following relationships [7]:

$$F_{min} = 1 + 2(C_{a12} + R_n Y_{opt}^*), \quad (10)$$

$$G_{opt} = \sqrt{\frac{C_{a22}}{C_{a11}} - \left(\text{Im} \left\{ \frac{C_{a12}}{C_{a11}} \right\} \right)^2}, \quad (11)$$

$$B_{opt} = \text{Im} \left\{ \frac{C_{a12}}{C_{a11}} \right\}, \quad (12)$$

$$R_n = C_{a11}. \quad (13)$$

On the basis of relations (5)-(9), the elements of intrinsic circuit correlation matrix can be expressed as:

$$\langle |v_{au}|^2 \rangle = \langle |v_{a2}|^2 \rangle, \quad (14)$$

$$\langle |i_{au}|^2 \rangle = \langle |i_{a1}|^2 \rangle + \langle |i_{a2}|^2 \rangle + \langle |v_{a2}|^2 \rangle G_p^2 + 2G_p \text{Re} \langle v_{a2}i_{a2}^* \rangle, \quad (15)$$

$$\langle v_{au}i_{au}^* \rangle = \langle |v_{a2}|^2 \rangle G_p + \langle v_{a2}i_{a2}^* \rangle. \quad (16)$$

By direct comparison between "H" and "A" representations in Fig.2. and Fig.3b) respectively, the following relationships are obtained:

$$i_{a1} = -i_p / h_{21}^{(1)}, \quad (17)$$

$$v_{a2} = -\frac{h_{11}^{(2)}}{h_{21}^{(2)}} i_{ds} - e_{gs}, \quad (18)$$

$$i_{a2} = -\frac{1}{h_{21}^{(2)}} i_{ds}, \quad (19)$$

By using these transformation rules, we have derived elements of correlation matrices $C_a^{(1)}$ and $C_a^{(2)}$ as follows:

$$\langle |i_{a1}|^2 \rangle = \frac{\langle |i_p|^2 \rangle}{|h_{21}^{(1)}|^2}, \quad (20)$$

$$\langle |v_{a2}|^2 \rangle = \langle |e_{gs}|^2 \rangle + \frac{|h_{11}^{(2)}|^2}{|h_{21}^{(2)}|^2} \langle |i_{ds}|^2 \rangle + 2 \text{Re} \left\{ \frac{h_{11}^{*(2)}}{h_{21}^{*(2)}} \langle e_{gs}i_{ds}^* \rangle \right\}, \quad (21)$$

$$\langle v_{a2}i_{a2}^* \rangle = \frac{h_{11}^{(2)}}{|h_{21}^{(2)}|^2} \langle |i_{ds}|^2 \rangle + \frac{1}{h_{21}^{*(2)}} \langle e_{gs}i_{ds}^* \rangle, \quad (22)$$

$$\langle |i_{a2}|^2 \rangle = \frac{\langle |i_{ds}|^2 \rangle}{|h_{21}^{(2)}|^2}. \quad (23)$$

The parameters h_{11} and h_{21} of subcircuits (1) and (2) are given by

$$h_{21}^{(1)} = -1, \quad (24)$$

$$h_{11}^{(2)} = \frac{1 + j\omega r_{gs} C_{gs}}{j\omega C_{gs}}, \quad (25)$$

$$h_{21}^{(2)} = \frac{g_m e^{-j\omega\tau}}{j\omega C_{gs}}. \quad (26)$$

By using expressions (20)-(26) the correlation matrices (8) and (9), are obtained. By replacing these relations in (5) the complete intrinsic correlation matrix (6) becomes known. At the end, by replacing the elements of this correlation matrix in (10)-(13) the noise parameters are expressed as the function of equivalent intrinsic circuit elements and equivalent temperatures T_g , T_d , T_c and T_p , in the form given by (27)-(30).

The optimum reflection coefficient Γ_{opt} can be expressed in the standard way, using optimum admittance $Y_{opt} = G_{opt} + jB_{opt}$. The derived expressions (27)-(30) have been implemented within the circuit simulator Libra.

NUMERICAL RESULTS

The proposed model can be applied for MESFET and HEMT transistors. The results presented in this paper are related to a N71000A MESFET. For this transistor there are manufacturer's S -parameter data in the frequency range (1.5-26.5) GHz and noise parameter data at several discrete frequencies in the range (2-18) GHz.

Whole MESFET equivalent circuit including some additional parasitic elements has been chosen for further work. The equivalent circuit element values are

determined in optimization procedure of program Libra by comparing simulated and measured S -parameter data. The values obtained in this way are used as starting values in an optimization routine simultaneously applied to all equivalent circuit elements and four equivalent temperatures with the aim to reach the best agreement between simulated and measured S and noise parameters at frequency range of interest. In this way the following equivalent temperature values are obtained: $T_g = 150$ K, $T_d = 1519$ K, $|T_c| = 50$ K, $\tau_c = 11.41$ ps, $T_p = 531$ K.

The characteristics for noise parameters F_{min} , R_n , $|\Gamma_{opt}|$ and $\angle\Gamma_{opt}$ are shown in Figs. 4-7. The curves obtained by using the proposed model are denoted by MOD2. The referent curves (REF) are based on the measured data. Very good agreement between these two curves can be observed for all presented characteristics. On the other hand, the curves denoted by MOD1 correspond to the procedure when the gate leakage current influence is not considered. It can be seen that the characteristics obtained by proposed model suit much better to the referent ones, especially for minimum noise figure at low frequencies comparing to the model which does not involve considered effect.

$$R_n = \frac{r_{gs}T_g}{T_o} + \frac{Q_1Q_2}{g_m^2T_o} g_{ds}T_d + 2 \frac{|T_c|}{g_mT_o} (P_1 + Q_3r_{gs}P_2), \quad (27)$$

$$B_{opt} = - \frac{Q_3(g_{ds}T_d + g_m|T_c|P_1)}{R_n g_m^2 T_o}, \quad (28)$$

$$G_{opt} = \left[\frac{Q_3^2 \left((Q_3Q_4)^2 + g_m^2 T_g Q_4 + 2Q_3 g_m Q_4 |T_c| P_2 - (g_m |T_c| P_1)^2 \right)}{R_n g_m^2 T_o} + R_n g_m^2 T_o \left(\frac{g_m^2 G_p T_p + 2Q_3^2 Q_4 G_p + 2Q_3 g_m G_p |T_c| P_2}{R_n g_m^2 T_o} + G_p^2 \right)^{\frac{1}{2}} \right] \quad (29)$$

$$F_{min} = 1 + \frac{2}{g_m T_o} \left[(G_{opt} + G_p) R_n g_m^2 T_o + Q_3^2 r_{gs} g_{ds} T_d + Q_3 g_m |T_c| P_2 \right] \quad (30)$$

where:

$$\begin{aligned} Q_1 &= 1 + j\omega C_{gs} r_{gs}, & Q_2 &= 1 - j\omega C_{gs} r_{gs}, \\ Q_3 &= \omega C_{gs}, & Q_4 &= r_{gs} g_{ds} T_d, \\ P_1 &= \cos[\omega(\tau_c - \tau)] \quad \text{and} \quad P_2 = \sin[\omega(\tau_c - \tau)]. \end{aligned}$$

CONCLUSION

Transistor noise model based on two correlated noise sources (voltage source at the input and current source at the output) is extended by involving gate-leakage current effect. It should be first emphasized that this effect is modeled by a shunt conductance between gate and source, with an equivalent temperature T_p assigned.

It can be concluded that noise characteristics obtained by using developed model agree very well with referent ones in whole frequency range. Better adjustment is achieved comparing to the model which does not take into account considered effect especially for minimum noise figure at the lower part of frequency range.

The undoubted benefit of developed procedure is that it is very appropriate for implementation within standard program packages for microwave circuits simulation.

REFERENCES

- [1] V. Marković, B. Milovanović, N. Maleš: "CAD Prediction of Noise Parameters Behavior for Microwave FET Devices", *Proceedings of 17th Annual Semiconductor Conference CAS'94*, pp.375-378, Sinaia, Romania, October 1994.
- [2] V. Marković, B. Milovanović, O. Pronić, N. Maleš-Ilić: "Efficient Extraction of Intrinsic Transistor Noise Temperatures by Standard Microwave Software Tools", *Conference Proceedings ANTEM'96*, pp.501-504, Montreal, Canada, August 1996.
- [3] M.W. Pospieszalski, "Modeling of Noise Parameters of MESFET's and MODFET's and Their Frequency and Temperature Dependence", *IEEE Trans. Microwave Theory Tech.*, vol.MTT-37, pp. 1340-1350, Sept. 1989.
- [4] V. Marković, B. Milovanović, N. Maleš-Ilić, "MESFET Noise Modeling Based on Three Equivalent Temperatures", *Proceedings of the Conference EUMC'97*, pp.966-971, Jerusalem, Israel, September 1997.
- [5] "Touchstone and Libra Users Manual", EEsof, Inc. 1990.
- [6] R. Reuter, S. van Waasen, F.J. Tegude, "A New Noise Model of HFET with Special Emphasis on Gate-Leakage", *IEEE Electron Device Letters*, vol.16, pp.74-76, Feb. 1995.
- [7] J.A. Dobrowolski, *Introduction to Computer Methods for Microwave Circuit Analysis and Design*, London, Artech House, 1991.

UTICAJ STRUJE GEJTA NA MODELOVANJE ŠUMA MESFET-A

Bratislav Milovanović, Vera Marković,
Nataša Maleš-Ilić

Sadržaj - U radu je razmatran uticaj struje curenja na gejtu na šumne karakteristike MESFET-a. Prethodno razvijeni empirijski šumni model tranzistora na bazi tri ekvivalentne temperature dopunjen je na sledeći način: Postojanje struje gejta modelovano je pomoću odvodnosti između gejta i sorsa, a njen efekat na karakteristike šuma izražen je pomoću nove ekvivalentne temperature T_p . Izveden je set jednačina kojima se opisuju parametri šuma unutrašnjeg ekvivalentnog kola tranzistora u funkciji elemenata ekvivalentnog kola i četiri ekvivalentne temperature. Ovaj set jednačina osnova je postupka koji je implementiran u okviru programa Libra.

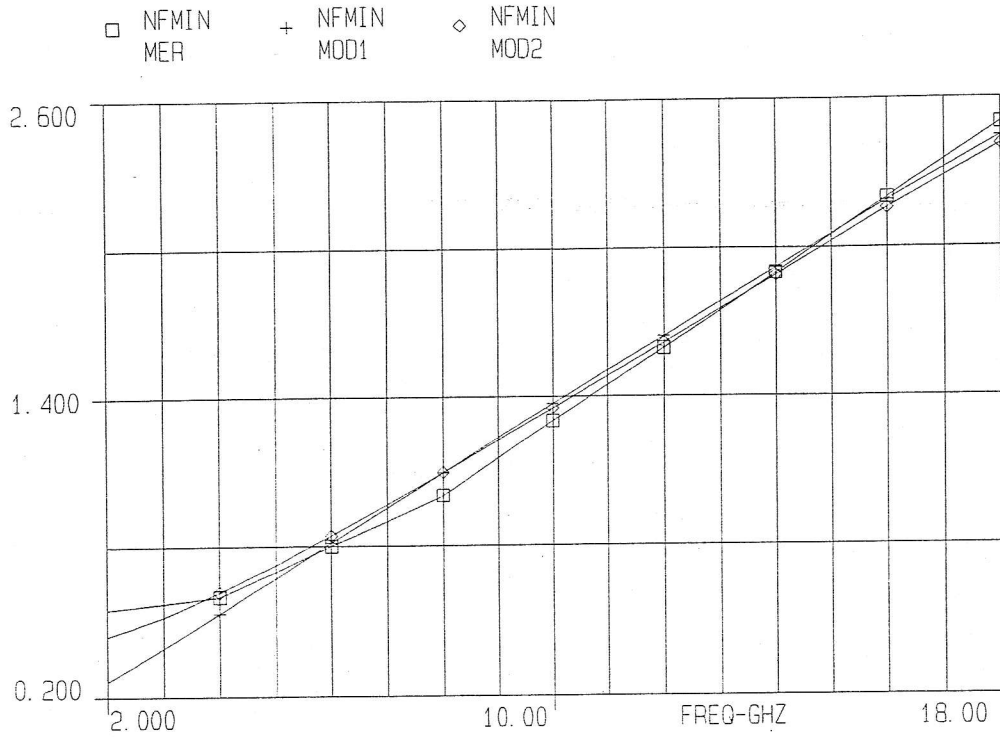


Fig.4. Minimum noise figure

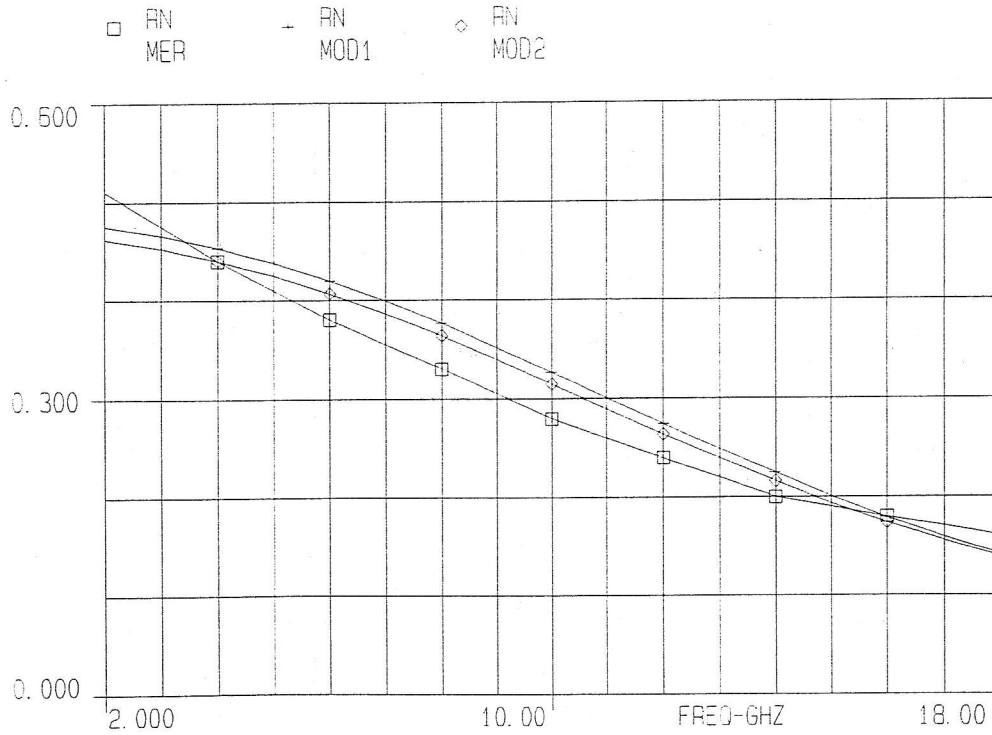


Fig.5. Normalized noise resistance

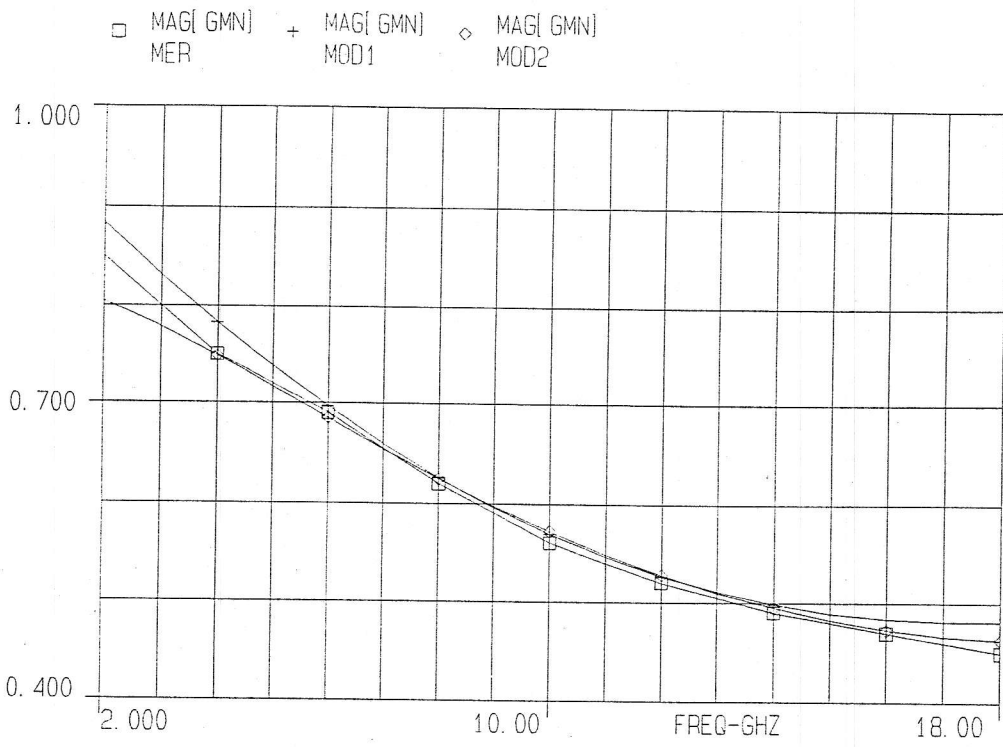


Fig.6. Magnitude of optimum reflection coefficient

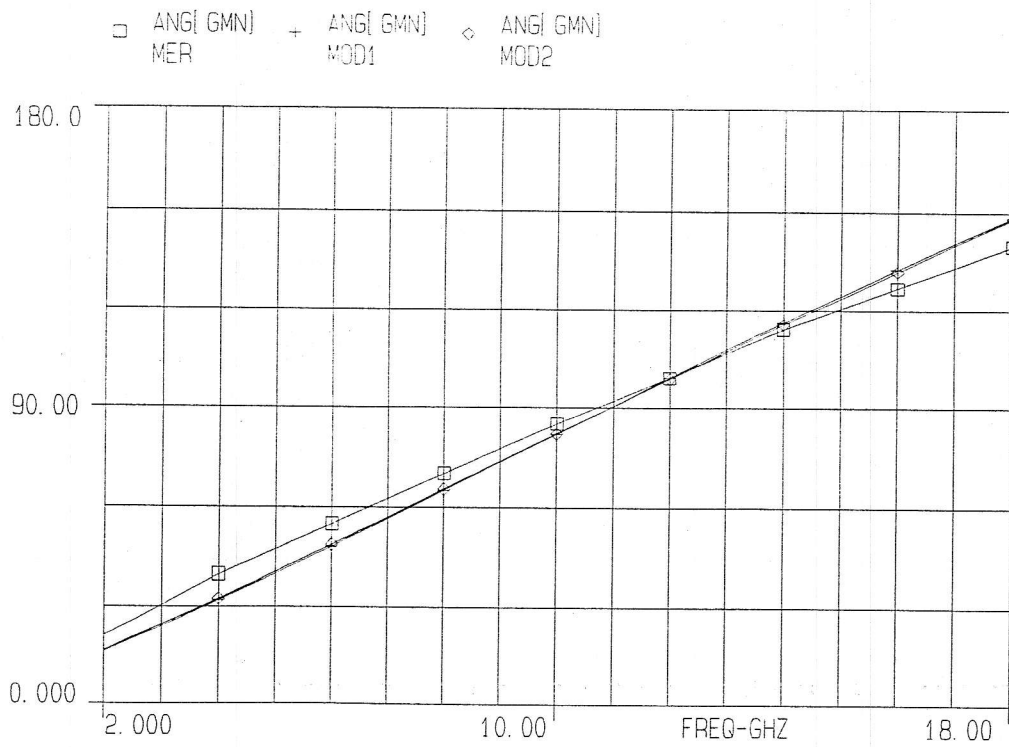


Fig.7. Angle of optimum reflection coefficient

An abridged version of this paper has been presented at the XLII ETRAN Conference, Vrnjačka Banja, June 2-5, 1998.

BELGRADE GRASPING SYSTEM

Dejan Popović¹ and Mirjana Popović²

¹Faculty of Electrical Engineering, Belgrade

²Institute for Medical Research, Belgrade

Abstract: Belgrade grasping system (BGS) comprises a four channel electronic stimulator, a set of six electrodes, and a set of sensors. BGS was designed to enhance the grasping and reaching of humans after spinal cord injury (SCI) and raise their level of independence. The controller cloning the natural grasping and reaching behavior of able-bodied humans is the major novelty of the BGS. This controller implements a sensory triggered preprogrammed control. BGS provides palmar and side grasping and control of elbow joint extension. Potential users are left with voluntary triggering of the system to initiate grasping/releasing of a given object. The stimulator includes the following components: 1) DC/DC converter providing four galvanically isolated channels; 2) four output stages designed to ensure constant current pulses with variable electrode impedance; 3) programmable controller based on the microcomputer Motorola 68HC11A8 capable of controlling pulse duration and frequency, and implementing a rule-based algorithm. BGS was tested in eight subjects with SCI. Daily functioning (handling utensils, comb, brush, phone, cup, glass and can, etc.) was improved and the working space increased when the BGS was used.

I. INTRODUCTION

Many of traumatic spinal cord injuries (SCI) lead to disability called tetraplegia. This is the most common cause of bilateral upper limb paralysis. SCI results in multiple impairment (e.g., bowel, bladder, sexual functions, etc.) but many humans with tetraplegia set restoration of grasp and release as a priority. Adaptive equipment, compensatory hand functioning, surgical procedures and orthotic management are customary rehabilitation strategies. In the past 25 years functional electrical stimulation (FES) of paralyzed but innervated muscles in upper extremities allowed functional restoration of grasping [1]. FES is by far the most promising technique for restoring the grasping and reaching, because it integrates preserved natural mechanisms with the externally driven biological resources [2-11].

FES systems with up to 30 percutaneous stimulation channels were systematically investigated for exercising both hand and arm muscles and used for restoration of movements [1, 4, 5]. FES systems are intended to control the elbow and wrist joints, and the hand [3, 12]. Stimulation profiles were derived from the averaged, amplified, filtered and integrated electromyographic (EMG) signals recorded from able-bodied subjects [4, 5]. Voluntary inspiration and expiration of air generated the control signals.

FES for reaching and grasping has been evaluated with a multichannel surface system [6, 13]. This system uses voice

control for twelve channels of bipolar stimulation for the control of the elbow joint (two channels), hand and wrist. Only a few subjects were tested with this rather complex system.

Investigators at Case Western Reserve University (CWRU), Cleveland, Ohio, developed a fully implantable system. Up to eight channels were used to enhance grasping [2, 3, 7, 11], often combined with surgical procedures [14]. The CWRU research team pioneered the usage of FES for control of reaching [15] where applying percutaneous electrodes to control elbow extension. A modern version of the reaching system is integrated with a fully implantable system for grasping [11]. The reaching system uses percutaneous electrodes and a simple feed-forward controller. A tilt sensor is attached to the upper arm and it generates control signals to turn on and off a stimulation channel applied to m. Triceps Brachii. Principles and methodology how to automatically control reaching, which have been used as the basis for BGS are described in details in Popović [12, 16]. BGS is a result of the development at the University of Miami [10,16], clinical evaluation of the Bionic Glove [17] and research at the University of Belgrade [18, 19].

II. PROGRAMMABLE STIMULATOR

Four-channel stimulator (Fig. 1). The following characteristics were chosen for the design: 1) the device has to be portable and battery powered; 2) monophasic, constant current stimulation pulses have to be used at the output; 3) programmable stimulation patterns have to allow pulse duration τ between 0 and 800 μ s, increments 20 μ s; interpulse interval T between 0 and 1000 ms, increments 20 ms; and current amplitude I between 0 and 80 mA, increments 4 mA; 4) low cost; and 5) control unit suitable for easy operation and non expert programmers.

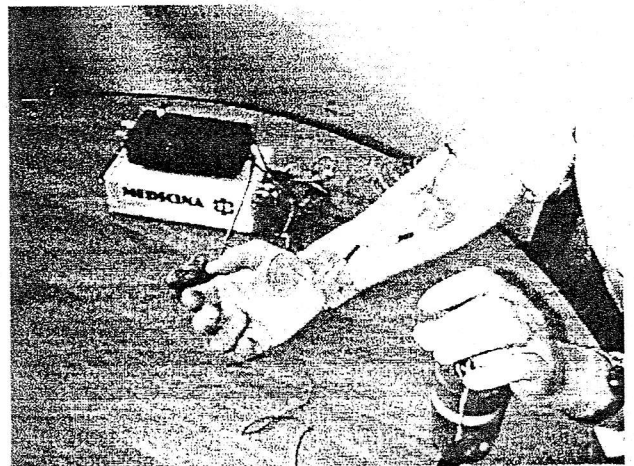


Figure 1: The BGS system. Electrodes for fingers and thumb flexion are shown. Left hand is controlling the triggering switch.

The power supply for the stimulator is realized by using a DC/DC converter (MAXIM 773 IC) and appropriate circuitry (Fig. 2). The advantages of such a design are small size and weight, and very low consumption both when operating and in the idle state. The design of power supply also ensures that when control is malfunctioning or the electrode impedance drops to low values the maximum current is limited; thus, the risk of injuries is minimized.

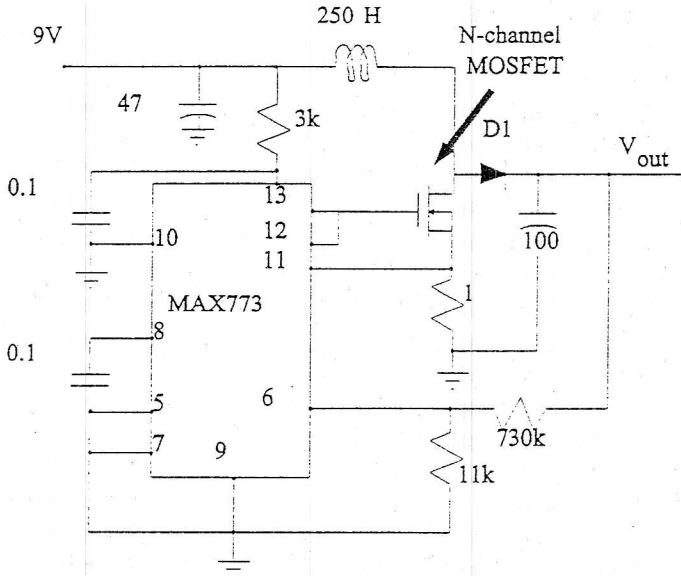


Figure 2: DC/DC converter used for the BGS

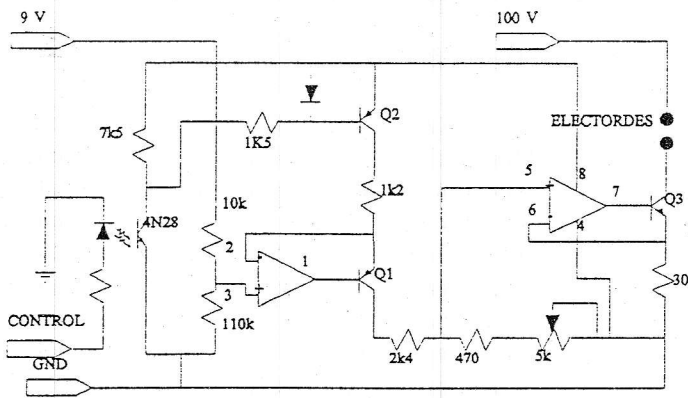


Figure 3: The output stage of the BGS

The output stage (Fig. 3) was designed to: 1) generate constant current pulses; 2) allow adjustments of the amplitudes of pulses. The output stage was realized using two OP-amps, and three transistors able to source current to a muscle through an electrode having the input impedance Z_p . Current sources are switched by galvanically isolated digital signals, which provide control of all output stages from the same control unit. The constant current source is designed with high voltage transistors. The amplitude of the constant current is determined by a potentiometer resistance, $P = 5k$.

The current amplitude varies within 10 percent about the nominal current value when the electrode impedance Z_p varies between 0.1 and 2 $k\Omega$. The realized output stage is physically

small and reliable. The standby power consumption is zero when the load current is zero. Short switching times of the output transistor (10 μs) are obtained by high current driving the optocoupler diode (50 mA). Both simulation and measurements have shown that the output stage produces pulses with the amplitude range from 0 to 80 mA with supply less than 100 V voltage throughout the working range [18].

The basic function of the controller is to drive the output stages with the desired pulse duration and frequency. In addition, the control unit must provide a powerful interface with the user, a host computer, and other stimulators and sensors. A general description of the controller (Fig. 4) shows that the interface was realized using IC (TOIM3232, Temic and MNI SIR transmitter, Nova Log) communication with a PC compatible computer, that a pulse shape is generated using programmable logic IC and counters.

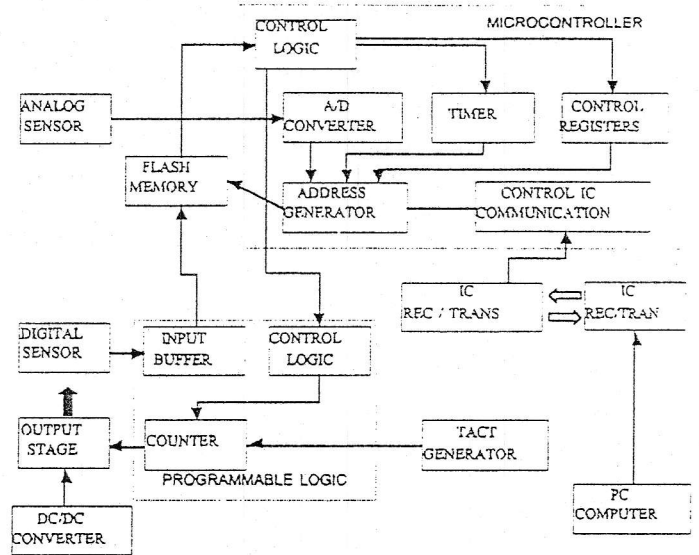


Figure 4: Scheme of the BGS controller

Flash memory (DA28F0116SV-080, Intel) is used for ensuring sufficient memory for eventual more complex applications. M68HC11A8 microcontroller is the core of the device operating at clock speed of 8 MHz. The microcontroller operation is supported by the reset (MX6314) and supply voltage monitoring circuit TL7705 and by the IC communication link [20]. A serial PROM (XC1736, Xilinx) and EPROM 27C256 are integrated into the controller. The expanded mode of microcontroller operation is used when the stimulator operates as an autonomous device. Programmable logic operates with PGA IC (XC3042-70PC841, Xilinx).

The A/D converter inputs of micro-controller can accept eight analog voltages ranging from 0 to 5 Volts. Up to four digital inputs can be used for control at this point, but this number can be increased to maximum of 8. Pulses at different outputs can not be generated simultaneously, they appear in sequence. The host PC based computer interface is realized by IC communication interface using TOIM chips.

III. CONTROL PARADIGM

For a long time a plausible approach for control of assistive systems relies on cloning or copying natural strategies. In order to clone the natural manipulation and grasping it was essential to study those functions.

In the broadest terms, there are two approaches for studying grasping the empirical and the analytical. The empirical approach explores grasping by humans and animals, the only successful grasping systems in our experience. Those studies came with some extremely important issues for external control of paralyzed hand. A concept of "virtual fingers" [21] suggests that any number of fingers that work as one can be modeled as single entity. Iberall [22] describes human grasping in terms of "oppositions," which are the basic hand configurations for applying forces to opposing faces of a grasped object.

All human grasps are formed from a set of only three oppositions: 1) pad, for forces between the pads of the fingers and thumb; 2) palm, for forces between fingers and the palm; and 3) side, for forces between the thumb and the side of the index finger. The importance of the listed features is essential since it is impossible to control individual finger alike humans do it naturally, and that the opposition is a feasible mechanism when externally stimulating finger and thumb flexor and extensor muscles.

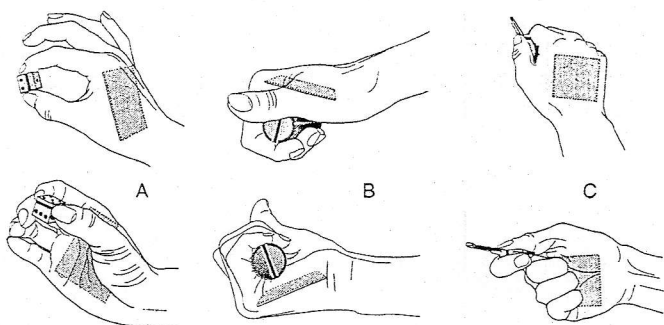


Figure 5: The grasp options: A) pad opposition; B) palm opposition; and C) side opposition. The figure adapted from Iberall [22] with permission.

Synergistic concept of stimulation is used in most assistive systems for restoring the grasping. Using a switch the user selects the type of grasping (palmar or side). The CWRU system is allowing the user to open and close the hand proportionally. The subject controls a joystick (0 to 100). At position 0 the hand is opened, and at position 100 the hand is closed. Joystick position between positions 0 and 100 subject controls the aperture of his hand by a preprogrammed individualized combination of stimulation parameters. Visual information is used as the only feedback. Voluntary input is integrated into the joystick and it allows "locking" the stimulating parameters at a desired combination.

Synergistic control is also implemented with three channels of surface stimulation within the Bionic Glove [8]. The operation

of the Bionic Glove can be described as an enhanced tenodesis. The Bionic Glove requires active control for both opening and closing operations. By extending the wrist the subject is turning on the stimulation of extensor muscles, and by flexing the wrist the flexor muscles are turned on. The hysteresis provides a large "dead zone". Dead zone is a range wrist at the wrist joint, which ensures that once the system is turned to open or close the hand, the stimulation regime will stay unchanged.

The Handmaster system [1, 6] uses a predefined synergy of opening and closing, and a switch mounted on a plastic splint containing the electrodes and supporting the wrist basically triggers the system. The Handmaster system was designed for exercise of muscles. The rigid structure of the splint holds the hand/forearm system in a fixed position reducing the applicability of the system for affective grasping.

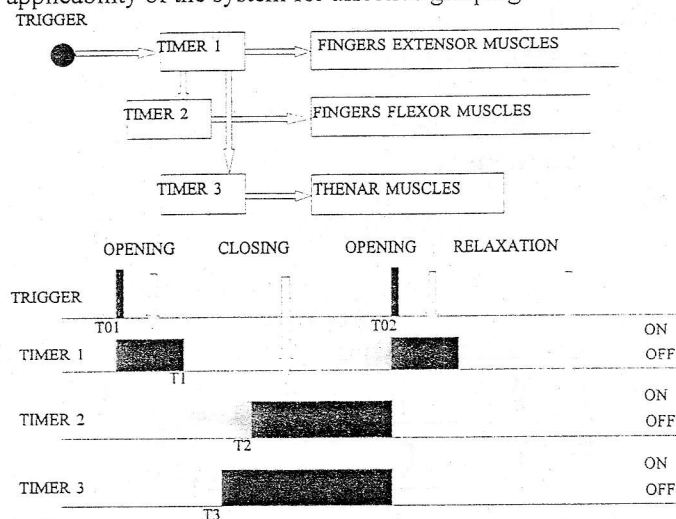


Figure 6: Timing diagram for the control of grasping

Control of grasping. The BGS includes two modality of grasping, and it follows the ideas implemented in the Handmaster system. The control system allows side and palm grasps by generating opposition. The control scheme shows the timing paradigm (Fig. 6). The grasping is separated into three phases: 1) opening of the hand (forming the correct aperture); 2) relaxing (allowing the hand to get a good contact with the

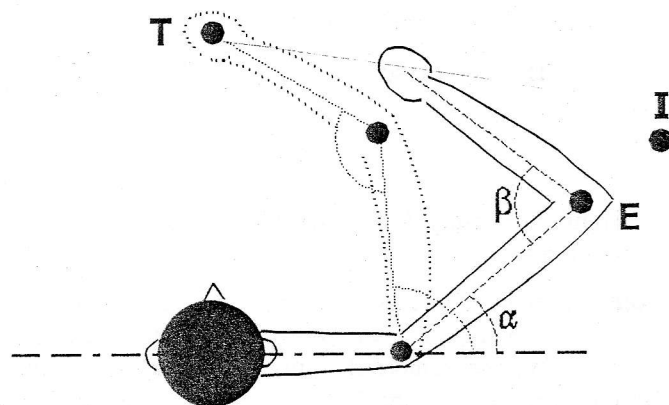


Figure 7: Joint angles used for control of reaching

object; and 3) closing the hand by opposing the palm and the thumb or the side of the index finger and the thumb. The releasing function includes two stages: 1) opening of the hand; and 2) remaining in the relaxed state. The control scheme shows that it is possible to select the duration of each of the phases of the grasp/release upon the individual characteristics of the subject, as well as need as his/her preferences. The choice of the grasp depends only on the relative duration of the periods T_2 and T_3 . If the period T_2 is longer, the palm grasp will be implemented and vice versa.

Control of reaching. A FES system for reaching requires effective control to permit subconscious and intuitive use. Here, we describe in short a paradigm used for control of the BGS. The following parameters are controlled: 1) the scaling parameter C between the angular velocities of the shoulder and elbow joints [16]; and 2) the individual stimulation parameters of the m. Triceps Brachii to generate movement with the desired angular velocity and its increment [12].

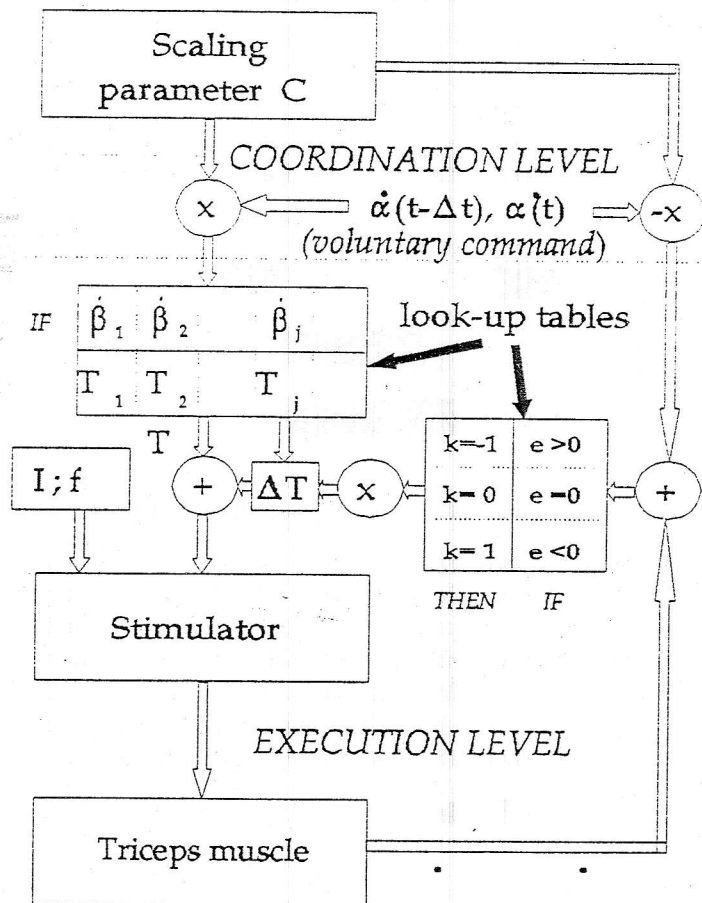


Figure 8: Sensory driven algorithm for control of reaching

Scaling introduces biological synergy into the control problem, and is not user specific. User specific stimulation parameters are a series of vectors composed of three elements: 1) the angular velocity of the elbow joint; 2) the increment of the elbow joint's angular velocity; and 3) the electric charge delivered to the muscle. The scaling depends only upon the position of initial

point of the hand and the target, that is the terminal point of the hand. The $\dot{\alpha}(t), \dot{\alpha}(t-\Delta t)$ are the angular velocities of the upper arm in two consecutive instants, and $\beta(t), \beta(t-\Delta t)$ are the corresponding computed values of the elbow angular velocities [Fig. 7]. The term 'computed' refers to dividing the measured shoulder angular velocity by the scaling coefficient C . The amplitude of the stimulation pulses (I) and the frequency of the stimulation (f) are preselected to allow a full range of externally elicited elbow extensions. The pulse duration (T) is responsible for the level of activation of the m. Triceps Brachii. The incremental pulse duration (ΔT) is the minimal value that generates a recognizable change in velocity. $\beta_m(t)$ is the measured relative angular velocity of the forearm with respect to the upper arm, and $e = \beta_m(t) - \beta(t)$ is the error in the sampled feedback control loop.

The structure of the controller is depicted in Fig. 8. The paradigm shown decomposes the control to two levels. At a higher, coordination level, the coefficient C is selected exclusively on the basis of the initial and target positions. This scaling does not depend on the user, but is universal for a given task. The input to the upper control level is the voluntarily controlled angular velocity of the shoulder joint. At the lower level, the time-sampled feedback adjusts the stimulation parameters to minimize the error between the achieved and desired elbow joint angular velocities. This sensory driven control uses a subject-dependent knowledge base within the microcomputer and only one channel of stimulation applied to the triceps brachii muscle, that is the muscle extending the elbow joint. The process of determining the scaling coefficient, the strategy to reducing the infinite number of scaling coefficients for practical implementation, and determining the stimulation parameters are described in details in Popović and Popović [12].

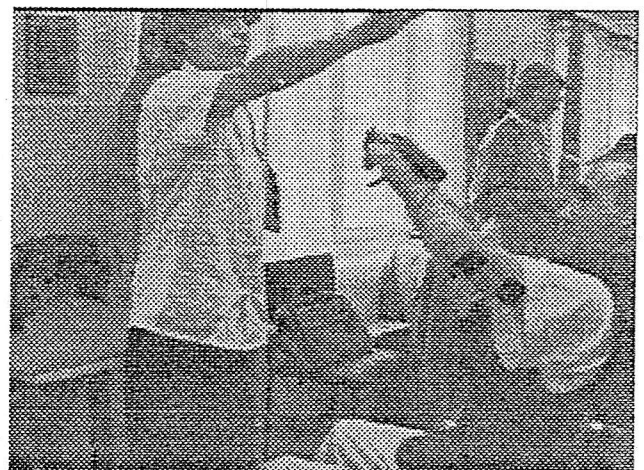


Figure 9: The usage of a reaching/grasping BGS system.

The usage of the system in a tetraplegic subject with an injury at C5 level is shown in Figure 9.

IV. ELECTRODES AND SENSORS

It is known that after SCI at cervical level many of the peripheral nerves still innervate arm and hand muscles, and this fact is used in all grasping systems [e.g., 6, 7, 8, 13, etc.]. In subjects in whom the forearm muscles are innervated it is possible to select small surfaces at the dorsal side to selectively stimulate deep and superficial finger flexors, without stimulating wrist flexion. It is also possible to select a small surface at the volar side of the forearm to selectively stimulate common finger extensor muscles. The diameter of the suitable electrodes, cathodes, is typically between 2 to 4 cm. The anode for both of these stimulation sites is the dorsal surface over the carpal tunnel. It is possible to position a cathode over the thenar muscle group, generating opposition and flexion of the thumb. The anode position described earlier, covering the median, ulnar and radial nerves is good enough for the control of the thumb. Three channels are a minimum number of channels for effective control of grasping.

The testing with more channels showed that better selectivity and better functioning can be obtained only if an implantable system is to be used [7]. The electrodes for stimulation of the elbow extension are positioned over the triceps brachii muscle that is lateral side of the upperarm. Both of the electrodes are relatively small, having the diameter of 2 cm each. It was shown that using the wrist anode is not functional.

Two accelerometers are used for the sensory control of reaching. The sensors are mounted at the shoulder and elbow joint angles. The accelerometers can be replaced with tachogenerators, but the mounting of the fixed axis transducers. The usage of flexible goniometers such as Penny and Giles, Blackwood, England [12, 16] is possible.

V. CLINICAL USE OF THE BELGRADE GRASPING SYSTEM

Eight young (23.8 ± 5.6 years of age), male subjects with a spinal cord injury between C5 and C7 were included in the evaluation. All eight subjects had a complete lesion. Four subjects had received only conservative treatment after their injury, two had undergone spinal operations, and two had been operated upon and had then received conservative treatment. At the beginning of the evaluation five subjects were over 24 months post-injury, two subjects were more than one-year post-injury, one more than six months. All the subjects signed an informed consent approved by the local ethics committee before they were tested and included into the study.

Following the quadriplegia index of function (QIF), the functional independence measure (FIM) and the upper extremity function test (UEFT) did the evaluation. All tests were done at the beginning of the test, and after one and two months of the usage.

QIF - Quadriplegia Index of Function.

Selected sections of importance for judging the improvement in hand functions were tested. Attention was paid to feeding, dressing and grooming. The scoring used the following grades: 4 - completely independent, requires no assistive device; 3 - independent with an assistive device, requires no human supervision, subject can put on assistive device; 2 - requires human supervision only, with or without physical contact; requires no lifting by another person; 1 - requires physical contact involving lifting of subject or part of subject's body by one person only; 0 - completely dependent, patient cannot do activity at all. The grade 9 was an indication of a specific comment, which can not be generalized. The feeding was scored to a maximum of 24 points, dressing was bringing a maximum of 20, and grooming a total of 12 points; hence, the maximum for all activities was 56 points.

FIM - Functional Independence Measure

FIM included a total of six activities of self care; two of sphincter control; three activities of relevance for mobility; two types of locomotion, two types of communication and three social cognition elements totaling 18 categories. The levels were: 7 - complete independence (timely and safely); 6 - modified independence (with a device) for activities which do not require helper; 5 -supervision (100 %), 4 - minimal assistance (70 %), and 3 - moderate assistance (50 %) for modified dependence; and 2 - maximal assistance (25 %) and 1 for total assistance (0 %) for complete dependence. The maximum score for FIM is 126.

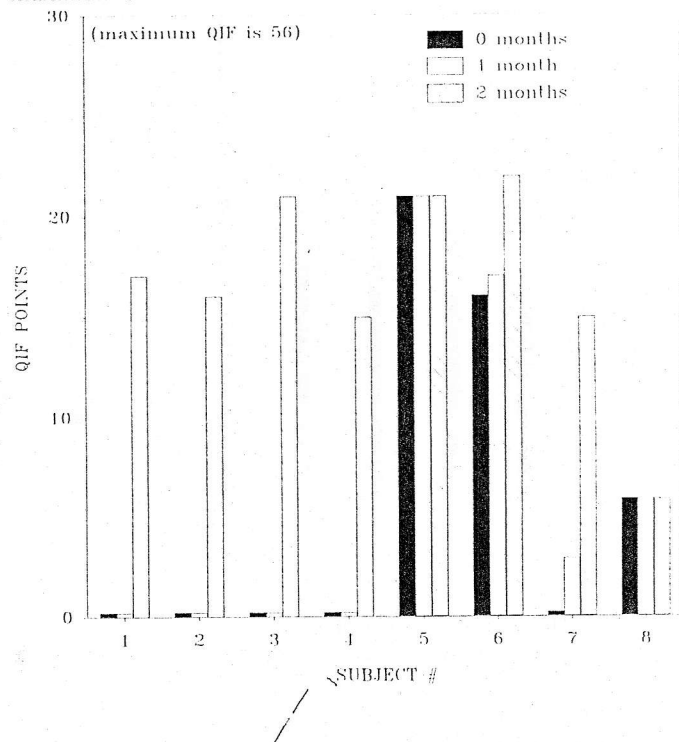


Figure 10: QIF determined at the beginning, and after one and two months of using the BGS

UEFT - Upper Extremity Function Test.

The purpose of this test was to determine differences in the

performance of certain activities of daily living with the use of the BGS when compared to performance of the same tasks done without it. In "non-device" trials subjects used any splint or cuffs that they would normally use to accomplish any of these tasks. The performance of the tasks was graded as Success, Failure and Non Tested. The time taken to complete the tasks was noted. The subjects were asked to rate the ease of accomplishing the task with and without the glove as Better, Worse and No Difference. The following tasks were tested: 1) combing hair; 2) using a fork; 3) picking up a VHS tape; 4) picking up a full juice can; 4) picking up a full pop/soda can; 6) writing with a pen; 7) answering the phone; 8) brushing teeth; 9) pouring from a one liter juice box; 10) drinking from a mug; and 11) handling finger food.

One subject stopped using the BGS after he completed the study and seven continued to use it at home after the study was finished. The main reason for quitting the program was very low cost-benefit ratio between using the device and no device.

The mean QIF was 7.5 ± 3.3 at the beginning, and reached 20.1 ± 3.8 , i.e. an improvement of 168%. The maximum possible QIF score is 56; hence, the determined average was still only about 36 % of maximum. The improvement in QIF is most probably the result of exercising and practice.

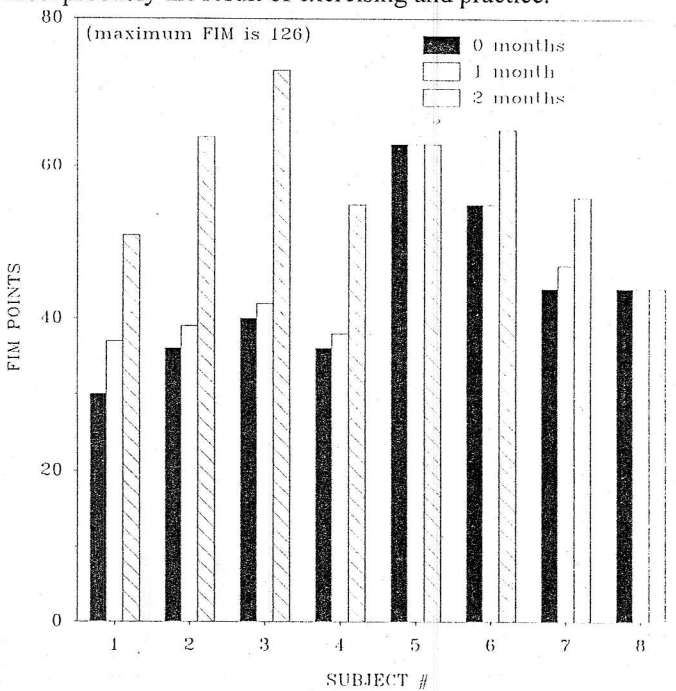


Figure 11: FIM determined at the beginning and after one and two months of using the BGS

The mean FIM value for all 8 subjects changed from 44.4 ± 13.5 at the beginning of the study to 64.8 ± 16.6 after two months of the training. The maximal FIM score is 126; hence, the maximum value is still only about 51% of the normal value. The increase of the FIM must be associated not only with usage of the BGS, but also with exercise and getting better due to practice. Figs. 10 and 11 show clearly why the subject No #5 stopped using the system. QIF and

FIM remained the same for and therefore, for him the application of the BGS was just a burden. Although subject 8 did not improved, he was motivated to continue using the system, mainly because he is much more functional because of the decreased spasticity (reported subjectively).

The comparison of efficacy in daily living activities when using the BGS with respect to functioning without the BGS is summarized in Fig. 12. Eleven tasks are listed in the horizontal axis: manipulating a comb, a fork, a VHS tape, a pop and a small can, a pen for writing, a toothbrush, a one liter package of juice to pour the contents into the glass, a mug, and finger food. The number of subjects is shown on the vertical axes. The top panel shows results in subjects whose hand function was improved with use of the BGS; the middle panel shows subjects in whom function deteriorated and the bottom panel shows subjects in whom there was no significant difference. Fig. 12 reflects the performance in the seven subjects who continued to use the BGS. The number in the "better" group increased with time, while the number in the "no difference" group decreased.

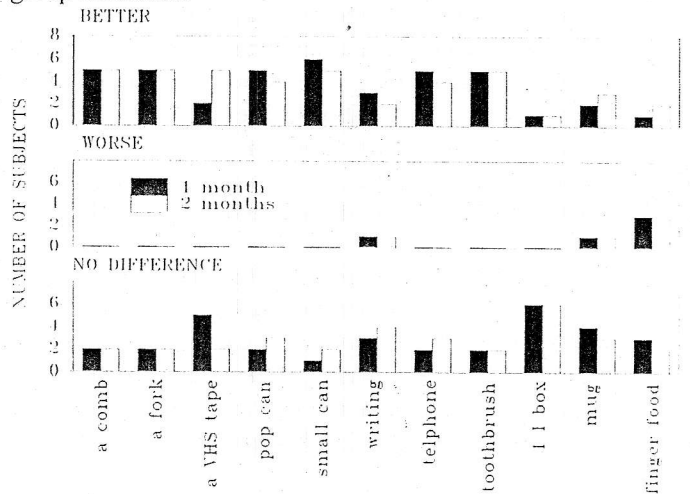


Figure 12: Functioning with the BGS after one and two months. Seven subjects who continued using the device are included in the table

The number of subjects who performed worse was increased over the evaluation period for three tasks (writing, mug and finger food). These tasks were better without the BGS mainly because the material in the hand portion of the garment obstructed finger flexion somewhat. The difference in performing tasks was rather small in most of the subjects which were grouped in "better", and the judgement was based on the time elapsed for the activity. The subjective decision between "better" and "no difference" for using the phone, handling cans, using a mug, and eating finger food was very difficult after six months. The differences were substantial in handling a fork, a comb, and a toothbrush and handling bigger objects such as a VHS tape and a one-liter juice container.

QIF and FIM increased after treatment with the BGS for the subjects who started with a lower score. Scores improved by 25%. The changes in both QIF and FIM occurred after about

six weeks. During the last two weeks the increase in FIM and QIF is rather small.

The upper extremity function test (Table 1) result is given for the seven subjects who continued using the system after the evaluation. This result shows that in all subjects there was an improvement in functioning.

PERIOD	BETTER	WORSE	NO DIFFERENCE
1 month	5	0	2
2 months	6	0	1

Table 1: The UEFT for seven subjects continuing to use the BGS fro daily activity after the evaluation

The subjective statement is that in most patients the tonic component of spasms was decreased, being very beneficial for grasping abilities. The strength of grasping was increased in all subjects similarly to what is reported in Prochazka et al. [8]. The manipulation of bigger objects is enhanced greatly with the BGS.

Subjects complained of difficulties in donning and doffing of the system. A particular difficulty was in getting the correct position of the electrode for hand opening. Two of seven subjects were able to put the BGS on independently, one with little help, and four needed major assistance. The size of electrodes in some cases played major role in avoiding stimulation spillover, being contra productive. The positioning of the electrodes in this case was difficult because with a small change of position the motor effect changed dramatically.

Successful usage of the system was achieved when controlling a push-button switch with the contralateral hand. The initial setting of timings, determining the intervals and delays between the stimulation of and opening, thumb and finger flexors remained basically the same throughout the evaluation.

VI. CONCLUSION

There are a fair number of people with C6-C7 lesions who may benefit from usage of the BGS. The benefits can be good enough to make the BGS a daily-used assistive device. Some technical improvements, specifically in relation to cosmesis, positioning of the electrodes and donning/doffing will increase the number of regular users. Subjects with a strong tonic component of spasticity, compromising the functioning of the hand, benefited mostly. Power grasp and handling bigger objects was greatly improved (e.g., pouring from a container, using a telephone receiver, handling tapes). Slipping of objects remained a problem in most subjects even after prolonged use. We have not noticed a change in skin texture after the study, and the friction coefficient remained very low. It is clear that the functional status of the potential user is the most important factor in deciding whether the BGS should be used as a long-term assistance.

The general conclusion is that the best candidate for the usage of the BGS should be selected among C6 - C7 tetraplegics with a FIM between 25 and 50, eventually up to 75 (out of 126), and a QIF between 0 and 13, eventually up to 27 (out of 56). The second criterion deals with the motivation to get independence, which is almost proportional to the efficiency of grasping. The BGS, alike other similar FES devices, contributes very much as a therapy; however, there are some subjects in whom this type of orthosis is valuable for improved grasping.

BIBLIOGRAPHY

- [1] R.Triolo, R.Nathan, Y.Handa, M.W.Keith, R.R.Betz, S.Carroll and C.Kantor, "Challenges to clinical deployment of upper limb neuroprostheses", *J. Rehab. Res. Develop.*, 33:111-122, 1996.
- [2] P.H.Peckham, J.T.Mortimer and E.B.Marsolais, "Controlled prehension and release in the C₅ quadriplegic elicited by functional electrical stimulation of the paralyzed forearm musculature", *Ann. Biomed. Eng.*, 8:369-388, 1980.
- [3] P.E.Crago, W.D.Memberg, M.K.Usey, M.W.Keith, R.F.Kirsch, G.J.Chapman, M.A.Catorgi and E.J.Perreault, "An elbow extension neuroprosthesis for individuals with tetraplegia", *IEEE Trans. Rehabil. Eng.*, IEEE TRE-6:1-6, 1998.
- [4] Y.Handa and N.Hoshimiya, "Functional electrical stimulation for the control of the upper extremities", *Med. Prog. Techn.*, 12:51-63, 1987.
- [5] N.Hoshimiya, A.Naito, K.Yajima and Y.Handa, "A multichannel FES system for the restoration of motor functions in high spinal cord injury patients: A respiration-controlled system for multijoint upper extremity", *IEEE Trans. Biomed. Eng.*, BME-36:754-760, 1989.
- [6] R.H.Nathan and A.Ohry, "Upper limb functions regained in quadriplegia: A hybrid computerized neuromuscular stimulation system", *Arch. Phys. Med. Rehabil.*, 71:415-421, 1990.
- [7] P.H.Peckham and M.W.Keith, "Motor Prosthesis for restoration of upper extremity function", In: R.B.Stein, P.H.Peckham and D.Popović (Eds.) *Neural Prostheses: Replacing motor function after disease or disability*, Oxford University Press, pp 162-190, 1992.
- [8] A.Prochazka, M.Gauthier, M.Wieler and Z.Kenwell, "The Bionic glove: an electrical stimulator garment that provides controlled grasp and hand opening in quadriplegia", *Arch Phys. Med. Rehabil.*, 78:137-145, 1997.

- [9] S.Reberšek and L.Vodovnik, "Proportionally controlled functional electrical stimulation of hand", *Arch. Phys. Med. Rehab.*, 54:378-382, 1973.
- [10] S.Saxena, S.Nikolić and D.B.Popović, "An EMG-controlled grasping system for tetraplegics", *J. Rehab. Res. Develop.*, 32:17-24, 1995.
- [11] B.Smith, Z.Tang, M.W.Johnson, S.Pourmedhi, M.M.-Gazdik, J.R.Buckett and P.H.Peckham, "An externally powered multichannel, implantable stimulator-telemeter for control of paralyzed muscles", *IEEE Trans. Biomed. Eng.*, BME-45:463-475, 1998.
- [12] D.Popović and M.Popović, "Tuning of a nonanalytical hierarchical control system for reaching with FES," *IEEE Trans. Biomed. Eng.*, BMI-45:203-212, 1998.
- [13] R.H.Nathan and S.Shany, "Commercialization of the Handmaster NMS1R," *Proc. II Annual IFESS Conf.*, Burnaby, B.C., pp. 151-155, 1997.
- [14] E.Moberg, "Surgical treatment for absent single-hand grip and elbow extension in quadriplegia", *J. Bone Surg.*, 57-A:196-206, 1975.
- [15] L.J.Miller, P.H.Peckham and M.W.Keith, "Elbow extension in the C5 quadriplegic using functional neuromuscular stimulation", *IEEE Trans. Biomed. Eng.*, 36:771-780, 1989.
- [16] M.Popović and D.B.Popović, "A new control for reaching in tetraplegics", *J. Electromyography and Kinesiology*, 4:242-253, 1994.
- [17] S.Jović et al. "Improvements of grasping: clinical evaluation of the Bionic Glove", *Proc. II Annual IFESS Conf.*, Burnaby, B.C., pp. 155, 1997.
- [18] M.Ilić, D.Vasiljević and D.Popović, "A programmable electronic stimulator for FES systems," *IEEE Trans. Rehabil. Eng.*, TRE-2:234-239, 1994.
- [19] M.Popović and D.B.Popović, "Belgrade grasping system", *Proc. of the ETRAN Conference*, Vrnjačka Banja, 2-5 Jun, (in print), 1998.
- [20] N.Fišekovic and D.B.Popović, Programmable controller for an electronic stimulator, *J. Aut. Control*, University of Belgrade, 1998 (accepted for publication)
- [21] M.A.Arbib, T.Iberall and D.M.Lyons, "Coordinated control programs for movements of the hand", In the *Hand Function*, (Eds.) A.W.Goodwin and I.Darian-Smith, Springer Verlag, Berlin, pp 111-129, 1985.
- [22] T.Iberall and C.L.MacKenzie, "Opposition space and human prehension", in *Dexterous robot hand*, Eds. S.T.Venkataraman and T.Iberall, Springer Verlag, New York, pp. 32-54, 1990

ACKNOWLEDGEMENT

The work on this project was partly supported through the research grant from the Ministry for science and technology of Serbia. The micro-controller was designed and tested by Mr. Nebojša Fišeković, as part of his MS thesis submitted to the Faculty of Electrical Engineering, Belgrade in 1998. We would like to acknowledge the clinical evaluation of the system to physiatrists Drs. A.Stojanović, D.Vulović and S.Jović, Ph.D. and therapists Mrs. A.Pjanović and S.Radosavljević from the Institute for Rehabilitation "Dr Miroslav Zotović", Belgrade.

Suppression of Noise Contamination in Control Systems with Internal Model

Milić R. Stojić, University of Belgrade, Faculty of Electrical Engineering
Milan S. Matijević, University of Kragujevac, Faculty of Mechanical Engineering

Abstract - Recently, the structure design of digital feedback control systems with internal model attracts the attention of many researchers and control engineers. The basic idea have been presented in seminal papers by late Professor Ya. Z. Tsytkin. The main features of proposed structure consist in high degree of robustness with respect to changes of control plant parameters and in its efficiency of elimination of different kinds of realistic external disturbances. However, the nature of internal model within the control loop may produce an undesired sensitivity to the measuring noise that produce ripple changes of command signal and, consequently, fluctuations of controlled variable. Note that, in the design of high-performance speed- and position-controlled electrical drives, the internal model produces unwanted vibrations of set shaft speed and/or angular position due to quantization noise that contaminates the feedback signal obtained by finite-resolution position sensors.

In this paper, the sensitivity properties of process control system with internal model is analyzed in details with respect to sampling time, noise characteristics, and typical models of control plant. To suppress fluctuations of controlled variable different methods based upon the digital filtering of relevant feedback signals are proposed. The results of analytical investigations are verified by simulation runs that illustrate the noise suppression and effects of suggested modifications of the control scheme on the speed of system response, stability margin, and system ability in taking off the outcome of deterministic external disturbances.

Key words: Internal model control, internal model principle, process control, computer control

I. INTRODUCTION

In control systems, it is commonly required either to keep the control variable on certain desired value or to track the prescribed variable reference signal, as accurately as possible, in the presence an unmeasurable external disturbance. To match these requirements, IMP (Internal Model Principle) and IMC (Internal Model Control) assuring the disturbance absorption are advantageously applied [1-5].

In some sense, many control structures include IMP or IMC; the observer based-systems, for example. However, different new control structures including IMP explicitly, have been recently proposed by Ya.Z. Tsytkin [6]. In [7], Tsytkin compared the control system with IMP and H^∞ and H^2 optimal controllers of non-minimum-phase control plants. In [5] and [8], the adaptive algorithm within the IMP

and synthesis of robust-optimal control system were proposed, respectively. Tsytkin and Nadezhdin [9] utilized IMP for continuous-time control systems. The design of tracking systems with IMP and significantly long process deadtime has been proposed in [10]. In the survey paper [11], Gonzalez and Antskalis reviewed and compared up-to-date control structures utilizing IMP. It has been shown that the Tsytkin control structure with IMP [6] reveals advantage, when compared with the standard IMC suggested by Morari and Zafiriou [12].

Generally, IMP enables the elimination of different kind of external disturbances and improves the system robustness with respect to changes of plant parameters.

This paper gives an analytical procedure for designing of IMP-based controller [8,13] for a wide class of typical processes that have their transfer function characterized by a steady-state gain factor, one time constant, and a transport lag. The particular attention is paid to sensitivity properties of IMC with respect to a measuring noise. A suitable modification of IMP control structure is proposed in order to minimize effects of the noise contamination of measuring signal.

II. CONTROL STRUCTURE WITH INTERNAL MODEL

Fig.1 shows the basic control structure, which includes the internal model within the feedback loop [5,7,8,13]. In the structure, the control plant is described by transfer functions $W(s)$ and $W_f(s)$ derived in the vicinity of certain nominal working regime. Let us suppose that the corresponding pulse transfer function are calculated from (1) as

$$\begin{aligned} W(z) &= Z\left(\frac{1 - e^{-sT}}{s} W(s)\right) = \frac{z^{-1-k} P(z^{-1})}{Q(z^{-1})} \\ W_f(z) &= Z\left(\frac{1 - e^{-sT}}{s} W_f(s)\right) = \frac{P_f(z^{-1})}{Q(z^{-1})} \end{aligned} \quad (1)$$

where $z^{-1-k} P(z^{-1})$ and $Q(z^{-1})$ denote polynomials in z^{-1} which resolve the two-input internal model of the control plant, while polynomials $A(z^{-1})$ and $C(z^{-1})$ (Fig.1) determine the internal model of system external disturbance. These polynomials are used to enable so called disturbance absorption. Other polynomials $P_r(z^{-1})$, $P_y(z^{-1})$ and $R(z^{-1})$ appearing in the structure of Fig.1 are synthesized so to match the desired system stability margin and speed of system continuous-time response. In Fig.1, integer k defines

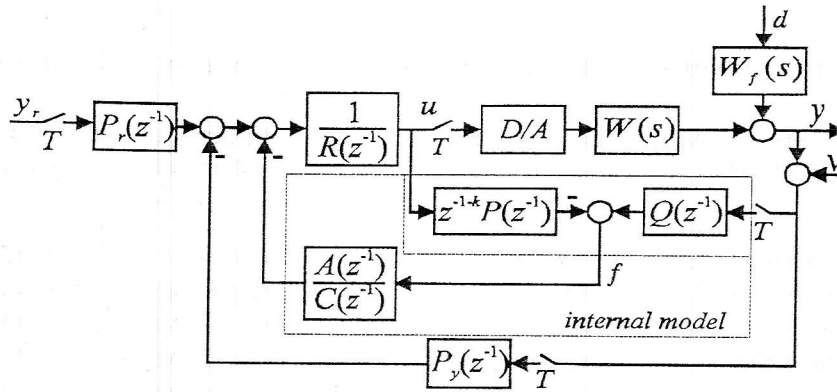


Fig. 1. System structure with internal model

the control plant deadtime, while: y , y_r , u , and d denote respectively the controlled variable (system output), reference signal (system input), command (manipulated variable), and external disturbance. An additive measuring noise is denoted by ν . From Fig. 1, z-transform of the internal

plant model output, i.e., of the disturbance internal model input f can be reduced into the form

$$F(z) = P_f(z^{-1})D(z) \quad (2)$$

Z-transform of the system output is obtained as

$$Y(z) = \frac{z^{-k}P(z^{-1})P_r(z^{-1})}{R(z^{-1})Q(z^{-1}) + z^{-k}P(z^{-1})P_y(z^{-1})} Y_r(z) - \frac{P_r(z^{-1})(C(z^{-1})R(z^{-1}) - z^{-k}P(z^{-1})A(z^{-1}))}{(R(z^{-1})Q(z^{-1}) + z^{-k}P(z^{-1})P_y(z^{-1}))C(z^{-1})} D(z) \quad (3)$$

When compared with other IMC schemes, the control structure in Fig.1 is superior. Namely, the suggested two-input internal model of the control plant has finite duration impulse response determined by orders of polynomials $z^{-k}P(z^{-1})$ and $Q(z^{-1})$. Unlike of the single-input internal models with infinite impulse responses, the use of two-input internal models enables the control of both stable and unstable control plants [13]. Another obstacle of classical control structures with IMP consists in the absence of output feedback [8]. When the absorption principle is precisely implemented, the closed-loop transfer function of the system in Fig.1 does not contain parameters of internal model and thus the system reveals a high degree of robustness [6,8]. Moreover, the synthesis of control structure in Fig.1 is relatively simple and may be reduced to the problem of solving two polynomial equations. The resulting controller is more efficient [6] and of lower order than one proposed in [12].

Notice that the system with IMP may be significantly sensitive on measuring noise. Namely, from equation (2) it can be observed that the output f of the two-input control

plant internal model contains entire information about the system external disturbance. This signal is employed to generate the control component for disturbance compensation. Thus, an added measuring noise affects the internal model and generates the control signal components for disturbance compensation even in the case when the disturbance does not exist. Thus the internal model, due to noise contamination of its input, can produce ripple changes of command signal and fluctuations of the system output. To suppress these undesirable effects, the suitable modification of the control structure in Fig.1 is proposed by inserting digital filter within the control portion of system. In doing so, the modified structure with IMP shown in Fig.2 is obtained.

Another structural modification shown in Fig.3 is possible. This structure gives a slightly better result in suppressing effects of noise contamination. However, the design of system in Fig.3 is more complicated and therefore will not be considered in more details.

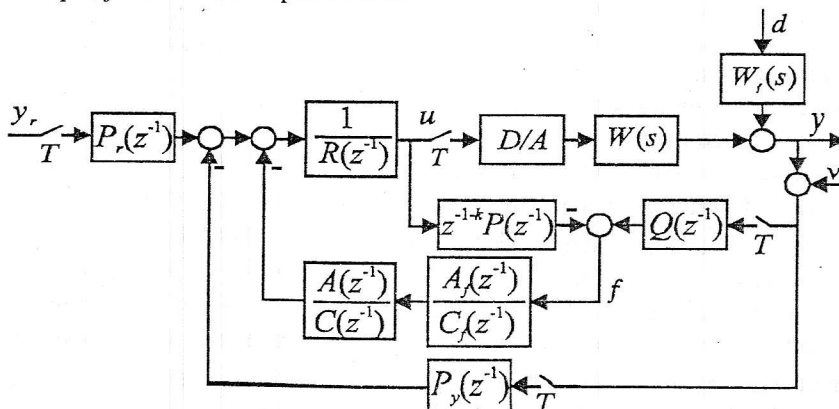


Fig.2. Modified system structure

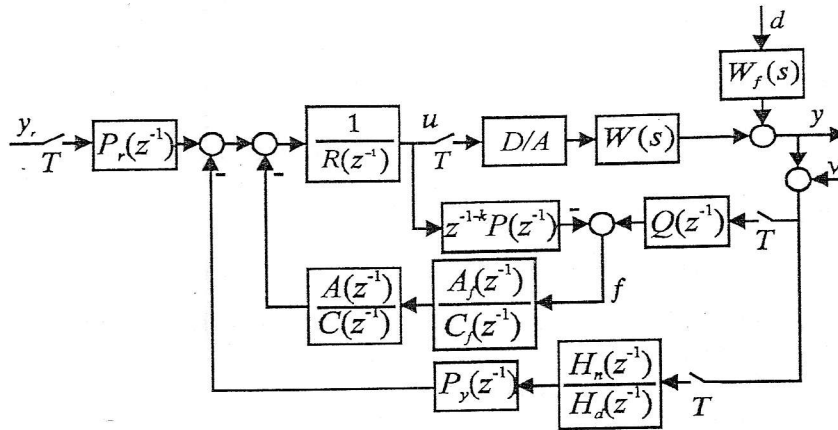


Fig.3. Modified system structure with IMP

III. ABSORPTION PRINCIPLE

Suppose that the external system disturbance is regular, i.e., its $m(k)$ sample may be represented by the finite number m_o previous samples $m(k-1), m(k-2), \dots, m(k-m_o)$ [3]. In such case, there exists polynomial $S(z^{-1})$ of (m_o-1) -order, which satisfy relation

$$(1 - z^{-1}S(z^{-1}))D(z) = 0 \quad (4)$$

where $D(z)$ denotes z -transform of an external disturbance. Relation (4) is called the compensating equation and digital filter $(1 - z^{-1}S(z^{-1}))$ is defined as the absorption filter or the compensating polynomial [7, 8, 13].

The absorption filter is designed for a specified kind of realistic external disturbance. It has the finite impulse response and its pulse sequence becomes identically equal to zero after $n \geq m_o$ sampling periods. Hence, equation (4) may be considered as the necessary and sufficient condition for disturbance absorption. Having the apriori information about

$$z^{-1-k}P(z^{-1})A(z^{-1}) + (1 - z^{-1}S(z^{-1}))B(z^{-1}) = C(z^{-1})R(z^{-1}) \quad (5)$$

where $B(z^{-1})$ denotes polynomial which is to be determined. Polynomials $P(z^{-1}), A(z^{-1}), C(z^{-1})$ are known from the internal model. Polynomials $R(z^{-1})$ and $S(z^{-1})$ resolve the control strategy and disturbance prediction, respectively. Notice, the closed-loop transfer function of the system in Fig.1, derived from equations (3) and (5),

$$\frac{Y(z)}{Y_r(z)} = \frac{z^{-1-k}P(z^{-1})P_r(z^{-1})}{R(z^{-1})Q(z^{-1}) + z^{-1-k}P(z^{-1})P_y(z^{-1})} \quad (6)$$

does not depend upon the internal model.

For minimum-phase control plants, polynomial $R(z^{-1})$ may be adopted as

$$R(z^{-1}) = P(z^{-1}) \quad (7)$$

When the system transient response and steady-state accuracy are specified by the corresponding transfer function $G_{de}(z)$, then, according to (6) and (7), the following relationship is obtained

the kind of disturbance, the prediction polynomial $S(z^{-1})$ is simply determined. For example, for an incline disturbance $d(kT) = a_1 \cdot kT + a_o$, the absorption polynomial becomes $S(z^{-1}) = 2 - z^{-1}$.

Note, the absorption principle is equivalent to IMP and its purpose is to include the disturbance model within the system control structure [6].

IV. CONTROL SYSTEM STRUCTURE SYNTHESIS

The design of the system control structure in Fig.1 may be reduced to the synthesis of polynomials by solving two polynomial equations. First one determines the specified system closed-loop pole spectrum, e.g., the desired system dynamic performance and second one governs the absorption of given kind of system external disturbance.

In virtue of (3) and (4), the system output becomes invariant to external disturbance if the following condition is satisfied.

$$G_{de}(z) = \frac{z^{-1-k}P_r(z^{-1})}{Q(z^{-1}) + z^{-1-k}P_y(z^{-1})} \quad (8)$$

Hence, after specifying $G_{de}(z)$, polynomials $P_r(z^{-1})$ and $P_y(z^{-1})$ that determine the control strategy are immediately calculated from (8).

Polynomials $z^{-1-k}P(z^{-1})$ and $Q(z^{-1})$ that determine the two-input internal model of the system control plant are obtained from the plant transfer function.

Polynomials $A(z^{-1})$ and $C(z^{-1})$, which define the disturbance internal model, are obtained by solving polynomial equation (5). These polynomials enable the absorption of an anticipated disturbance. Namely, $C(z^{-1})$ represents an arbitrary polynomial of lower possible order and polynomials $A(z^{-1})$ and $B(z^{-1})$ are obtained by solving equation (5). The choice of $C(z^{-1})$ significantly affects both the efficiency of disturbance absorption [14] and system filtering ability. If we introduce relation

$$B(z^{-1}) = B^1(z^{-1})R(z^{-1}) \quad (9)$$

then, according to (7) and (9), equation (5) becomes

$$z^{-1-k}A(z^{-1}) + (1 - z^{-1}S(z^{-1}))B^1(z^{-1}) = C(z^{-1}) \quad (10)$$

In the design of control structure in Fig.2, the outlined procedure does not changed essentially. Namely, the digital

$$z^{-1-k}A(z^{-1})A_f(z^{-1}) + (1 - z^{-1}S(z^{-1}))B^1(z^{-1}) = C(z^{-1})C_f(z^{-1}) \quad (11)$$

After selecting the low-pass digital filter of an appropriate bandwidth, the polynomial equation (11) is to be solved. To this end, polynomial $C(z^{-1})$ may be adopted and then polynomials $A(z^{-1})$ and $B^1(z^{-1})$ are calculated from (11).

In practical applications, ripple changes (ringing) of the command signal are undesirable. As it is known [14], the ringing of control variable occurs when the controller transfer function has poles (real or conjugate-complex) inside the left hand side of the unit circle of z -plane. These poles may be eliminated, as in the design of Dahlin's

filter inserted ahead of disturbance internal model does not affect closed-loop system transfer function (6) and thus polynomials $R(z^{-1})$, $P_r(z^{-1})$, and $P_y(z^{-1})$ stay unchanged. However, the polynomial equation (10), which defines the absorption condition, becomes

controller, by substituting $z=1$ into related polynomial factors.

V. EXAMPLE

The outlined design procedure is illustrated by an example of temperature regulation in the water-cooled exothermic process shown in Fig.4 [14].

The process transfer functions are identified as

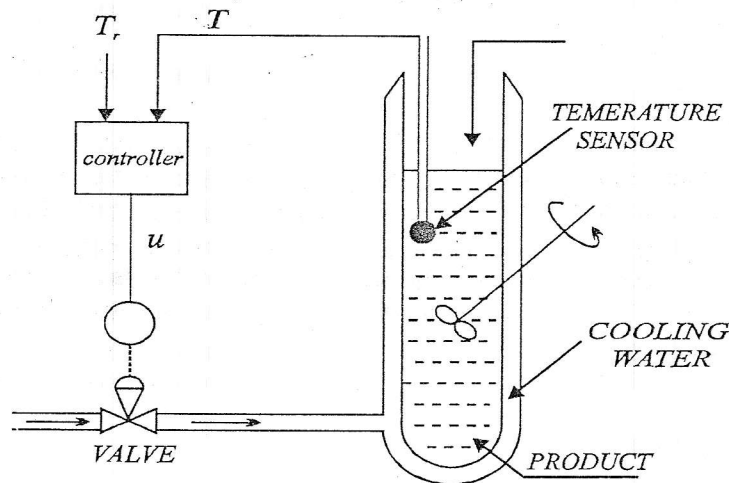


Fig.4. Exothermic process control

$$W(s) = \frac{\Delta T(s)}{Q(s)} = \frac{-0.015 \cdot e^{-2.3s}}{12.55s + 1} \quad \frac{^{\circ}\text{C}}{\text{l/min}} \quad (12)$$

$$W_f(s) = \frac{\Delta T(s)}{D(s)} = \frac{e^{-4.6s}}{12.55s + 1} \quad \frac{^{\circ}\text{C}}{^{\circ}\text{C}}$$

where ΔT is a temperature decrement in $^{\circ}\text{C}$ due to water flow q in l/min and d is an external disturbance due to temperature changes in of cooling water and process environment. In another variant, transfer functions of the same process may be approximated by two time constants and transport lag, i.e.,

$$W(s) = \frac{\Delta T(s)}{Q(s)} = \frac{-0.015 \cdot e^{-1.0s}}{(11.84s + 1)(2.61s + 1)} \quad \frac{^{\circ}\text{C}}{\text{l/min}} \quad (13)$$

$$W_f(s) = \frac{\Delta T(s)}{D(s)} = \frac{e^{-2.0s}}{(11.84s + 1)(2.61s + 1)} \quad \frac{^{\circ}\text{C}}{^{\circ}\text{C}}$$

Time constants and transport lags in (12) are given in minutes.

For a constant reference temperature T_r , the zero steady-state error is required. The system continuous-time step response is required to be governed by closed-loop transfer function with dominant complex-conjugate poles having the relative damping coefficient $\zeta = 1$ and undamped natural frequency $\omega_n = 1$ rad/s. In addition, the system must be able to absorb ramp and slow varying external disturbances.

We consider the process described by (12). Sampling period is assumed to be $T=1.15$ min. Then the process pulse transfer function is determined by $P_f(z^{-1}) = 8.756 \cdot 10^{-2} z^{-5}$, $Q(z^{-1}) = 1 - 0.91244z^{-1}$ and $z^{-1-k}P(z^{-1}) = -1.313 \cdot 10^{-3} z^{-3}$. The same polynomials define the process internal model. According to the desired closed-loop system poles and adopted sampling period, the pulse closed-loop system transfer function is derived in a straightforward manner as

$$G_{dc}(z) = \frac{0.466985}{z^3 - 0.633274z^2 + 0.100259z} \quad (14)$$

From equation (7), one gets $R(z^{-1}) = -1.3134 \cdot 10^{-3}$.

Now, solving equation (8), one obtains polynomials

$$P_y(z^{-1}) = 0.147458 - 2.777647 \cdot 10^{-2} z^{-1} \quad \text{and}$$

$$P_r(z^{-1}) = 0.466985 - 0.130366 z^{-1} - 0.129377 z^{-2}.$$

To enable the absorption of given class of disturbances, we solve equation (10) to obtain the internal model of disturbance as

$$\frac{A(z^{-1})}{C(z^{-1})} = \frac{3.159 - 2.43z^{-1}}{(1 - 0.1z^{-1})^3} \quad (15)$$

Measuring noise v is modeled as a stochastic signal with mean value $\mu=0$ and standard deviation $\sigma=0.01$. Fig.5 shows the pulse sequence of v used in the investigation of the proposed control structure efficiency.

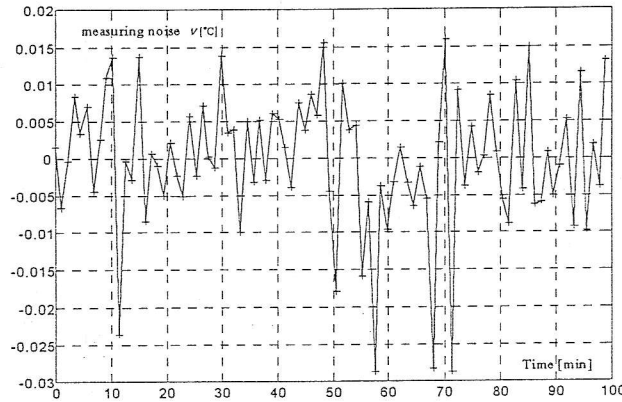


Fig.5. Pulse sequence of noise signal

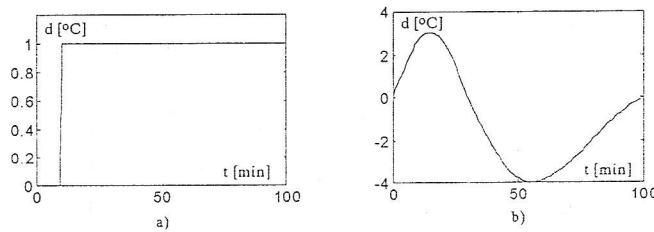


Fig.6. Disturbance signals used in simulation runs

The investigation of system properties was carried out by simulation. Figs.7-9 show the results of simulation runs for the system output (Figs.7-9 (a) and (b)), when the measuring noise is not encountered, and for the system output contaminated by measuring noise v (Figs. 7-9 (c) and

(d)). Effects of measuring noise may be observed by stochastic difference signal obtained as a difference of related pulse sequences of Figs. 7-9 (d) and Figs. 7-9 (b). The difference signal has the standard deviation of $\sigma = 3.271174 \cdot 10^{-2}$.

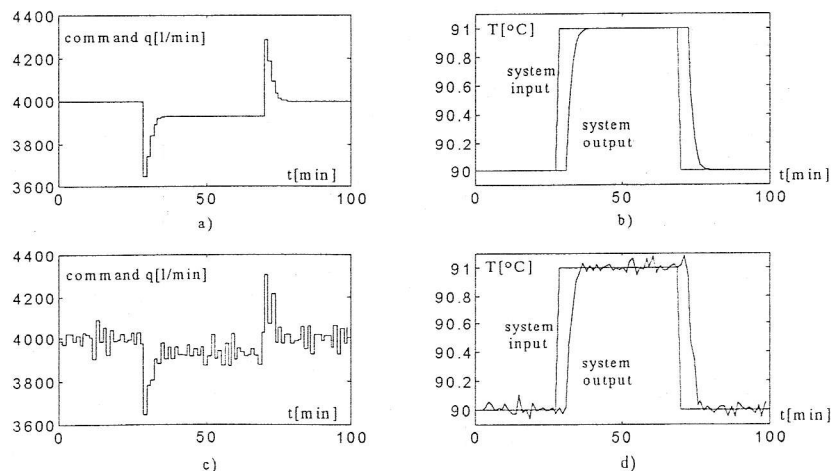


Fig.7. Illustration of control structure operation in the absence of an external disturbance

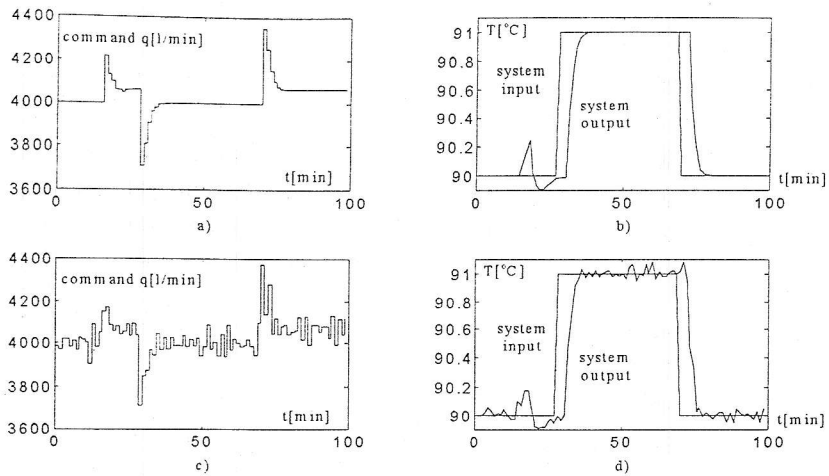


Fig.8. Illustration of control structure operation in the presence of external disturbance shown in Fig.6 (a)

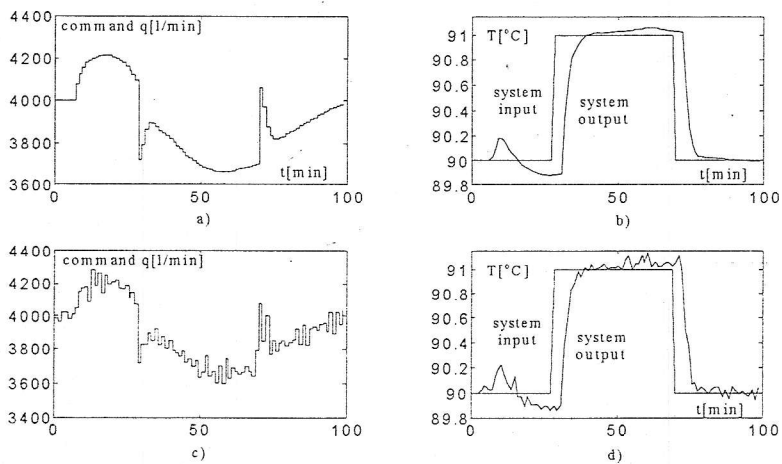


Fig.9. Illustration of control structure operation in the presence of external disturbance shown in Fig.6 (b)

To suppress undesirable effects of the output contamination by measuring noise, the system control structure is modified by introducing the third-order Butterworth digital filter [15] with bandwidth of $f_f=0.2$, $f_s/2=0.2/(2T)=1.45 \cdot 10^{-3}$ Hz and transfer function

$$\frac{A_f(z^{-1})}{C_f(z^{-1})} = \frac{0.0181 \cdot (1+z^{-1})^3}{1-1.76z^{-1}+1.1829z^{-2}-0.2781z^{-3}} \quad (16)$$

Solving polynomial equation (11), one obtains

$$\frac{A(z^{-1})}{C(z^{-1})} = \frac{5.4026313 - 4.6736313z^{-1}}{(1-0.1z^{-1})^3} \quad (17)$$

Effects of proposed modification are visualized by Figs.10-12. Now, the standard deviation of difference signal is reduced to $\sigma = 1.040332 \cdot 10^{-2}$. Hence, the inclusion of digital filter produces positive effects in suppressing measuring noise contamination. In the same time, the efficiency of disturbance absorption is not significantly deteriorated.

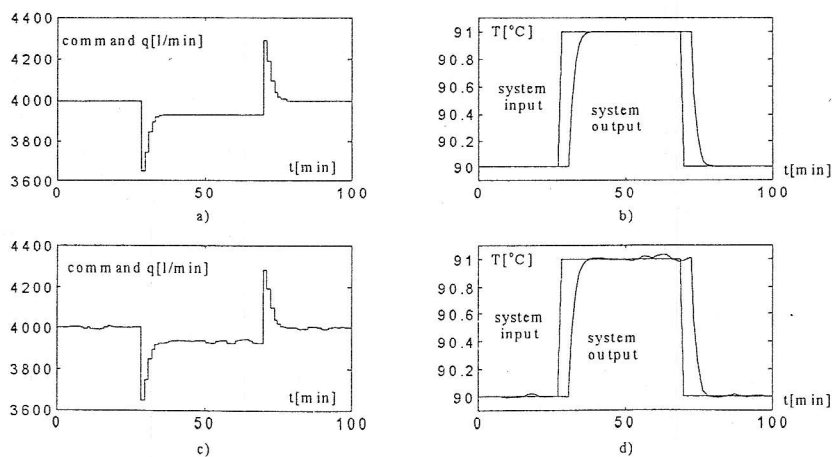


Fig.10. Illustration of control modified structure operation in the absence of external disturbance

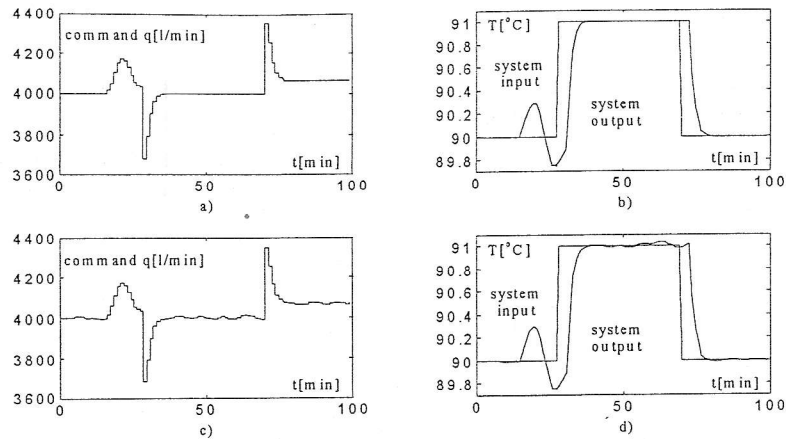


Fig.11. Illustration of modified control structure operation in the presence of external disturbance in Fig.6 (a)

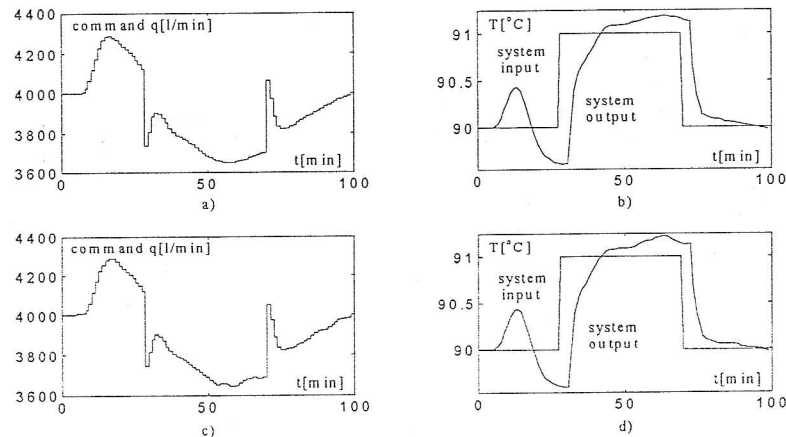


Fig.12. Illustration of modified control structure operation in the presence of external disturbance in Fig.6 (b)

If we modify digital filter (16) into

$$\frac{\lim_{z \rightarrow 1} A_f(z^{-1})}{C_f(z^{-1})} = \frac{0.144791}{1 - 1.76z^{-1} + 1.1829z^{-2} - 0.2781z^{-3}} \quad (18)$$

its filtering abilities slightly aggravate but in turn the solution of polynomial equation (11) becomes easier and the disturbance internal model obtains lower order

$$\frac{A(z^{-1})}{C(z^{-1})} = 5.577684 - 4.577684z^{-1} \quad (19)$$

Moreover, the standard deviation of difference signal becomes $\sigma = 1.1211088 \cdot 10^{-2}$. According to Fig.13, the disturbance absorption is slightly improved.

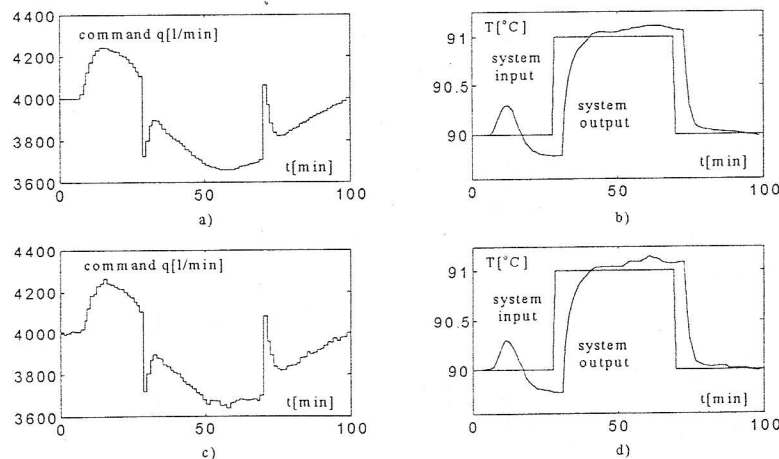


Fig.13. Illustration of modified control structure operation in the presence of external disturbance in Fig.6 (b)

Having smaller sampling period, the disturbance absorption becomes more efficient. Nevertheless, the choice of a new sampling period would require the repeated design

of system control structure. For example, under the same technical requirements concerning the quality of system transient response and for smaller sampling period of $T=0.23$

min, the following polynomials within the system control structure are calculated

$$z^{-1-k}P(z^{-1})=-2.7239671 \cdot 10^{-4} \cdot z^{-11}, \quad Q(z^{-1})=1-0.9818 \cdot z^{-1},$$

$$R(z^{-1})=-2.7239671 \cdot 10^{-4}, \quad A(z^{-1})=3.76573-3.4833 \cdot z^{-1},$$

$$C(z^{-1})=(1-0.1 \cdot z^{-1})^{12}, \quad P_y(z^{-1})=0.126911-0.0859148 \cdot z^{-1},$$

$$P_r(z^{-1})=4.22164 \cdot 10^{-2}+2.5635 \cdot 10^{-2} \cdot z^{-1}+1.4085 \cdot 10^{-2} \cdot z^{-2}+6.1993 \cdot 10^{-2} \cdot z^{-3}+9.5937 \cdot 10^{-2} \cdot z^{-4}-2.389 \cdot 10^{-2} \cdot z^{-5}-$$

$$4.4019 \cdot 10^{-2} \cdot z^{-6}-5.487 \cdot 10^{-2} \cdot z^{-7}-5.94 \cdot 10^{-2} \cdot z^{-8}-5.9754 \cdot 10^{-2} \cdot z^{-9}-5.74546 \cdot 10^{-2} \cdot z^{-10}.$$

Now, the added measuring noise is modeled by the signal with standard deviation of $\sigma=0.01$. The standard deviation of difference signal is now $\sigma=4.4252 \cdot 10^{-2}$. The results of simulation runs are shown in Figs. 14-16.

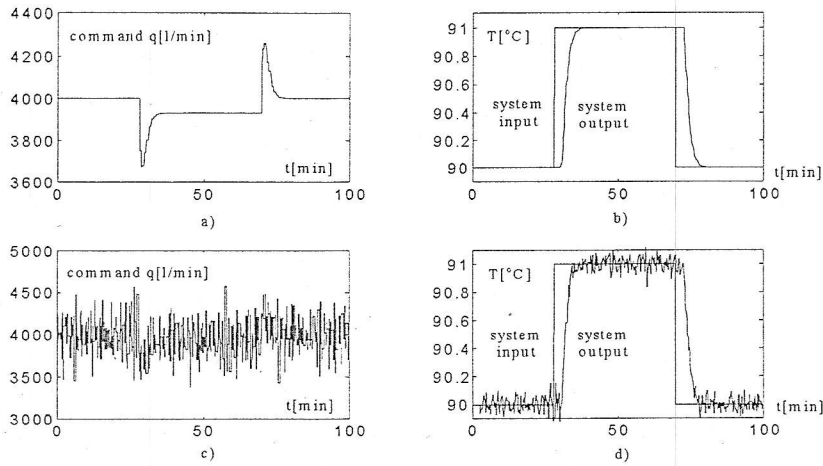


Fig. 14. Illustration of proposed control structure operation in the absence of external disturbance

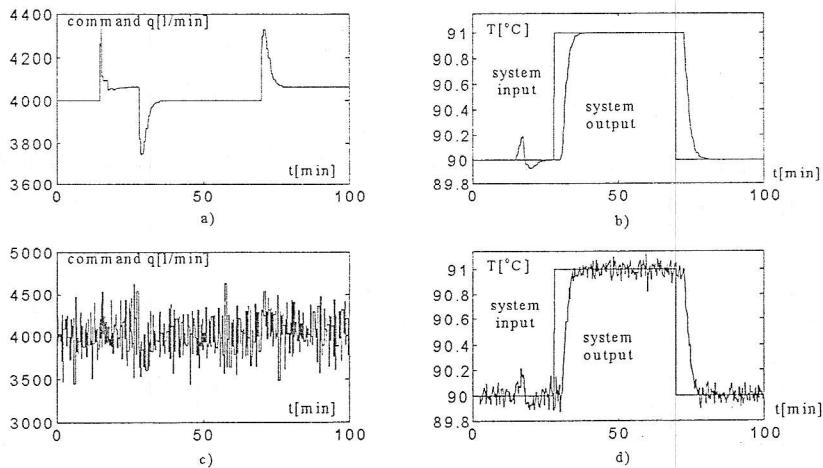


Fig. 15. Illustration of proposed control structure operation in the presence of external disturbance in Fig. 6 (a)

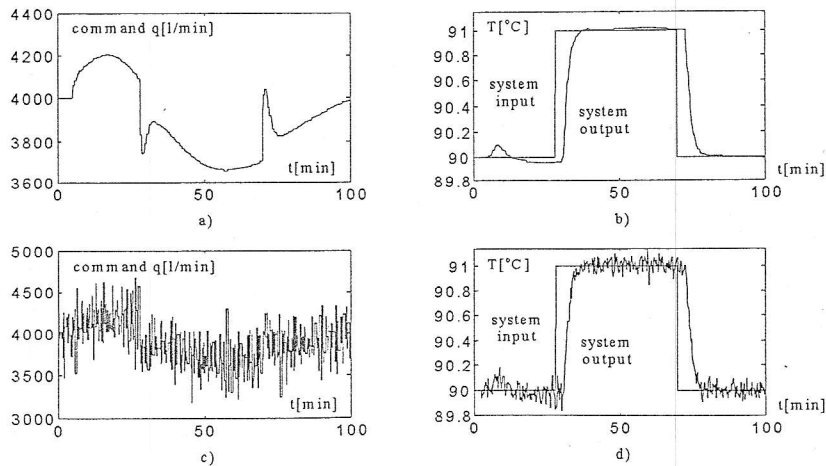


Fig. 16. Illustration of proposed control structure operation in the presence of external disturbance in Fig. 6 (b)

The suggested modification of control structures now is performed by introducing the third-order Butterworth digital filter with bandwidth of $f_f=0.2 \cdot f_s/2 = 0.2/(2T)=7.246 \cdot 10^{-3}$ Hz and transfer function

$$\frac{A_f(z^{-1})}{C_f(z^{-1})} = \frac{0.0181 \cdot (1+z^{-1})^3}{1 - 1.76z^{-1} + 1.1829z^{-2} - 0.2781z^{-3}} \quad (20)$$

With (17), the solution of polynomial equation (11) yields

$$\frac{A(z^{-1})}{C(z^{-1})} = \frac{5.115083 - 4.801273z^{-1}}{(1 - 0.1z^{-1})^{11}} \quad (21)$$

The modified control structure is tested by simulation runs. The simulation results are shown in Figs.17-19. The standard deviation of difference signal now is $\sigma=1.4673111 \cdot 10^{-3}$. This value is 30 times lower than in the case wherein the digital filter is excluded.

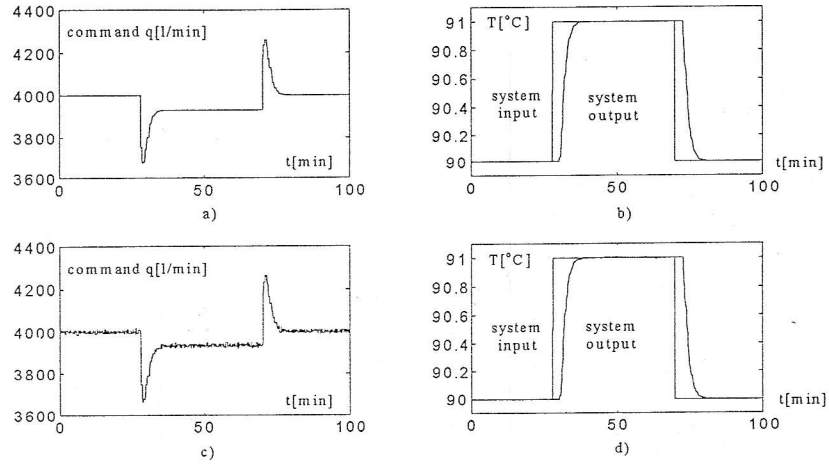


Fig.17. Illustration of proposed control structure operation in the absence external disturbance

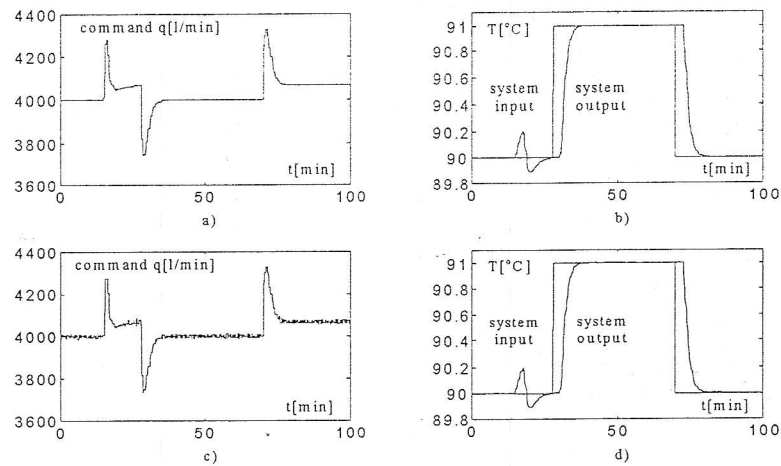


Fig.18. Illustration of proposed control structure operation in the presence of external disturbance in Fig.6 (a)

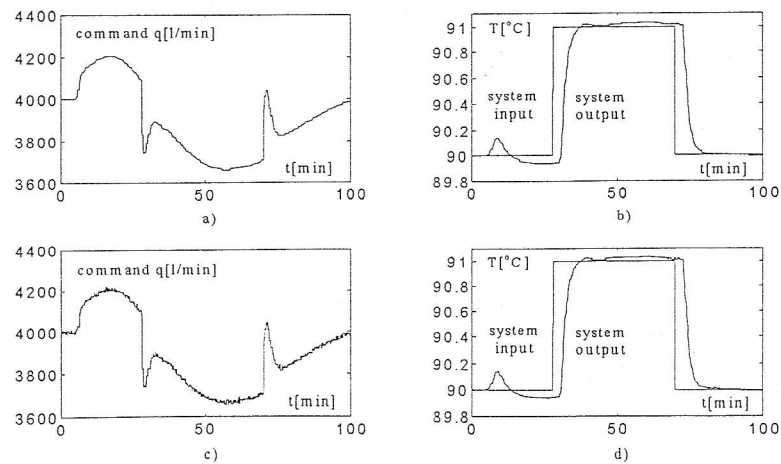


Fig.19. Illustration of proposed control structure operation in the presence of external disturbance in Fig.6 (b)

VI. CONCLUSIONS

The developed procedure enables the design of system with the prescribed dynamic performance and ability to compensate an anticipated class of external disturbances. As it is shown, the control structure based upon IMP may become highly sensitive to a measuring noise, which gets worse the overall system performance. The shortcoming may be significantly reduced by applying the suggested modified control structure, which in turn slightly deteriorates the system ability to absorb external disturbance. The appropriate choice of the sampling period and low-pass digital filter is of great importance for efficiency of proposed modified control algorithm; otherwise, the suppressing of noise contaminating may reduce the system abilities in disturbances absorption. Notice that the outline design procedure may be applied in straightforward manner for control of a wide class of minimum-phase processes.

The utility of proposed algorithm has been tested by numerous simulation runs. It is shown that the choice of appropriate control law is of great importance for system efficiency in both the quality of system transient response and efficiency in disturbance absorption. Namely, the command signal in a system with IMP comprises two separated components; first one, generated by disturbance internal model, absorbs the external disturbance and the second one, generated by system controller, governs the desired system continuous-time response, and these components are adjusted independently. However, the disturbance internal model may produce by its nature a significant sensitivity of the control system with IMP with respect to measuring noise and therefore the insertion of digital filter within the system control structure has been proposed in order to suppress the noise contamination of system output. But, filtering abilities of the modified disturbance internal model and its efficiency in disturbance absorption are two opposite requirements that may be balanced by an appropriate choice of sampling period. Namely, with a great sampling rate the efficiency of disturbance absorption is improved, but the system sensitivity to measuring noise may become impermissible.

REFERENCES

- [1] Кулебакин В.С., "О поведении непрерывно возмущаемых автоматизированных линейных систем", Докл. АН СССР 1949. Т.68. №5. с. 73-79.
- [2] Кулебакин В.С., "Операторное К(Д) изображение функций и его практическое применение", Тр. ВВИА им. Жуковского 1958. Вып. 695. с. 59.
- [3] Шеннон К., "Математическая теория дифференциального анализатора", Работы по теории информации и кибернетике. М: Издательство иностр. литер. (ИИЛ), 1983. с. 709-728.
- [4] В.А. Francis and W.M. Wonham, "The internal model principle for linear multivariable regulators", *Appl. Math. Opt.*, vol. 2, pp. 170-194, 1975.
- [5] Цыпкин Я.З., "Адаптивно инвариантные дискретные системы управления", *Автом. и Телемех.* 1991. №5. с. 96-121.
- [6] Tsytkin Ya.Z. and Holmberg U., "Robust stochastic control using the internal model principle and internal model control", *Int. J. Control*, vol. 61, №4, p 809-822, 1995.
- [7] Цыпкин Я.З., "Оптимальные дискретные системы управления неминимально-фазовыми объектами", *Автом. и Телемех.* 1991. №11. с. 96-118.
- [8] Цыпкин Я.З., "Синтез робастно оптимальных систем управления объектами в условиях ограниченной неопределенности", *Автом. и Телемех.* 1992. №9. с. 139-159.
- [9] Tsytkin Ya.Z., and Nadezhdin P.V., "Robust continuous control systems with internal models", *Control Theory and Advanced Technology*, 1993., 9.
- [10] Tsytkin Ya.Z., "Robust internal model control", *50th Anniversary Issue of DSCD, ASME Transactions*, 115., №2(B), pp. 419-425., 1993.
- [11] Gonzalez O.R., Antsaklis P.J., "Internal models in regulation, stabilization and tracking", *Int. J. Control* 1991, V. 53, №2. P. 411-430.
- [12] Morari M., Zafiriou E., *Robust Process Control*, Englewood Cliffs, N. J.: Prentice Hall
- [13] Цыпкин Я.З., "Новые классы дискретных периодических систем управления", *Автом. и Телемех.* 1994. №12. с. 76-92.
- [14] Stojić M.R., *Digitalni sistemi upravljanja*, Nauka, Beograd, 1994.
- [15] Draganović L.J.S., *Elementi i sistemi automatskog upravljanja-principi gradnje*, LOLA Institut, Beograd, 1996

AN APPROACH TO THE DESIGN OF A SELF-TUNING CONTROLLER USING STATE SPACE APPROACH

Branko Kovačević, Željko Đurović and Ljubiša Mišković
Faculty of Electrical Engineering, University of Belgrade, Yugoslavia

Abstract

A new class of self-tuning controllers that makes use of state space innovations model and single stage performance criterion, with a cross weighting term of the systems state and inputs, has been considered in the paper. The new advantage of a such type of controllers include relative simplicity of their derivation and implementation. It has been also shown that the proposed controller may represent an efficient tool for tracking as prespecified reference state trajectory of nonlinear and nonstationary type systems in the presence of stochastic disturbances with unknown statistics.

Key Words: adaptive control, self-tuned regulators, neighboring suboptimal control, stochastic systems.

I INTRODUCTION

The problem of adaptive control of linear discrete-time stochastic systems with unknown model parameters have drawn wide attention in recent years. Two groups of optimization based adaptive controllers have been widely studied in the literature. The first one makes use of the state space representation of the concerned system coupled with the linear quadratic Gaussian (LQG) optimal control theory and a sequential parameter estimation technique, in order to obtain an adaptive filtered state feedback controller [1,3-6,16,19,20]. The optimal adaptive control algorithms so obtained have the advantage of being globally stable, of being applicable to any finite dimensional controllable and observable system, and of providing with an effective control of the errors in the state trajectories. These are, however, achieved at the cost of a rather large computational burden, which makes it difficult to implement these algorithms real-time for some practical systems. The second group makes use of the input-output representation of the system coupled with the minimization of a generalized output error variance [7-9,11,12,15,23]. The main advantage of a such type of controllers, named self-tuning controllers, include relative simplicity of their derivation and implementation. However, the performance index selected for this approach does not minimize the errors in the state trajectories, as may be required in some applications. Also, the global stability of the controlled system requires the inverse system to be stable, which may exclude some non-minimum phase type systems. Finally, the self-tuning controller design tends to become complicated for multivariable systems.

In this paper we propose a new class of state space self-tuning controllers that represents a combination of the mentioned approaches. The proposed controller makes use of the steady state innovations model, in observer canonical form, of the concerned system coupled with a

single stage quadratic performance index with a cross-weighting term of the system states and inputs. The state estimator gain matrix is computed directly using the equivalent auto regressive moving average with exogenous input (ARMAX) representation of the adopted state space model, and the parameter estimation algorithm. Such a generalized quadratic performance index is used to exert adequate control influence on the system states over the entire sample period, and not just at sampling instants. For example, such a cross-weighting often helps to reduce the inter-sampling ripple in the dead beat control of known system [6]. Thus, here it is proposed to extend the idea of cross-weighting between the control inputs and the system states to adaptive control. Furthermore, the choice of a single stage performance index, coupled with the innovations state-space model, helps us to decrease the computational requirements, and simplify the adaptive feedback controller implementation. In this way, the controller gain matrix is obtained by solving an algebraic equation, and not a matrix Riccati equation, as is the case with the optimal LQG controller, while the state estimator gain is computed directly using a parameter estimation algorithm. To demonstrate the effectiveness of the proposed controller, we design the controller for a missile, representing a higher nonlinear and nonstationary type system. In this application, the controller is used to track a prespecified nominal state space trajectory in the presence of stochastic disturbances with unknown statistics.

II PROBLEM FORMULATION

Let us consider the system

$$x(k+1) = \Phi x(k) + \Psi u(k) + \Gamma w(k) \quad (1a)$$

$$y(k) = Hx(k) + v(k) \quad (1b)$$

where $x(k) \in R^n$ is the state, $u(k) \in R^m$ is the input and $y(k) \in R^p$ is the output of the system, $\{w(k)\}$ and $\{v(k)\}$ represent the disturbance terms and Φ, Ψ, Γ and H are the system matrices. Let us also make the following assumptions: (A1) the upper bounds of the dimensions n, m and p are known; (A2) the system matrices are constant, but unknown, and constitute a stable controllable and observable plant (1); (A3) the disturbances $\{w(k)\}$ and $\{v(k)\}$ are stationary zero mean white Gaussian sequences with unknown, but bounded, covariances $Q = E\{w(k)w^T(k)\}$ and $R = E\{v(k)v^T(k)\}$, respectively; (A4) the initial state $x(0)$ is a Gaussian random variable with known mean $\hat{x}(0) = E\{x(0)\}$ and covariance

$P(0) = E\{(x(0) - \hat{x}(0))(x(0) - \hat{x}(0))^T\}$; (A5) the random variable $x(0)$ and the noises $\{w(k)\}$ and $\{v(k)\}$ are independent of each other for all $k \geq 0$.

Let us introduce the single stage performance index

$$J(u) = E\{L[x(k+1), u(k)]\} \quad (2a)$$

where the criterion, or risk, function $L(\cdot)$ has the explicit form

$$L[x(k+1), u(k)] = \begin{bmatrix} x(k+1) & u(k) \end{bmatrix} \begin{bmatrix} W & S \\ S^T & U \end{bmatrix} \begin{bmatrix} x(k+1) \\ u(k) \end{bmatrix} \quad (2b)$$

Note that the expectation is taken over the distributions of the random variables concerned, and W and S are constant, bounded and non-negative definite weighting matrices ($W \geq 0, S \geq 0$), while U is constant, bounded and positive definite weighting matrix ($U > 0$).

The control problem in question may be then stated as follows: given the system model (1) under the assumptions (A1)-(A5), find the sequence $\{u(k), k > 0\}$ so as to asymptotically drive the expected value of the state $E\{x(k)\}$ to the origin of the state space, while minimizing the performance index (2).

It should be noted that the right hand side of eq. (2) represents the expected value of a general quadratic in the state $x(k+1)$ and the input $u(k)$. If the desired value of the state is null, that is, if we consider the so-called regulation problem, then the performance index (2) includes the state error variance, so that the control obtained by minimizing (2) will be referred to as the minimum state error variance (MSEV) control.

We now introduce the set of past observations

$$Y(k-1) = \{y(0), y(1), \dots, y(k-1)\}; k > 0 \quad (3)$$

and rewrite the right hand side of (2a) in the form

$$J(u) = E_{Y(k-1)} \left\{ E_{x(k+1), u(k)} \left\{ L[x(k+1), u(k)] | Y(k-1) \right\} \right\} \quad (4)$$

where the first expectation is taken over the distribution of the past set of data and the inner expectation is taken over the distributions of $x(k+1)$ and $u(k)$ conditioned on the past data set in (3). As is well known [2-6,11], minimum value of the performance index (2) may be achieved by minimizing the inner expectation alone

$$J_1(u) = E\{L[x(k+1), u(k)] | Y(k-1)\} \quad (5)$$

To facilitate the derivation of the desired adaptive MSEV control, let us consider first the case where the performance index (5) is to be minimized for the stochastic system (1) with all the model parameters and noise variances known.

III MINIMUM STATE VARIANCE ERROR CONTROL OF KNOWN SYSTEM

This is a single stage stochastic optimal control problem which may be easily solved by making use of the variational calculus. In order to do so, note first that the right hand side of (5) may be rewritten, after making use of (1a), as

$$J_1(u) = E\left\{ \left[x^T(k) \Phi^T + u^T(k) \Psi^T + w^T(k) \Gamma^T \right] W \times \right. \\ \left. \times [\Phi x(k) + \Psi u(k) + \Gamma w(k)] + u^T(k) U u(k) + \right. \\ \left. + 2 \left[x^T(k) \Phi^T + u^T(k) \Psi^T + w^T(k) \Gamma^T \right] S u(k) | Y(k-1) \right\} \quad (6)$$

To find the value of $u(k)$ that minimizes the performance index (6), we make use of the first order necessary condition

$$\text{grad}_u J_1(u) = 0 \quad (7)$$

To evaluate the gradient explicitly, we make use of the rules for differentiation of the inner product and the quadratic form with respect to vector quantities

$$\frac{\partial}{\partial a} (b^T a) = \frac{\partial}{\partial a} (a^T b) = b; \quad \frac{\partial}{\partial a} (a^T A a) = A a + A^T a \quad (8)$$

On evaluating the gradients of the inner products and the quadratic forms in (6) by using the rules (8), and taking into account the eq. (7), we then obtain

$$E\left\{ 2 \left(\Psi^T W \Phi + S^T \Phi \right) x(k) | Y(k-1) \right\} \\ + E\left\{ 2 \left(\Psi^T W \Psi + U + 2 \Psi^T S \right) u(k) | Y(k-1) \right\} = 0 \quad (9)$$

Here is used the fact that some terms in (6) are independent of the input $u(k)$ and, thus, does not contribute to the gradient. Since the matrix $(\Psi^T W \Psi + U + 2 \Psi^T S)$ is invertible under the assumption on U , we may solve the equation (9) to get the following MSEV control law

$$u(k) = M \hat{x}(k); \quad \hat{x}(k) = E\{x(k) | Y(k-1)\} \quad (10a)$$

where we have defined the matrix M by the relation

$$M = -(\Psi^T W \Psi + U + 2 \Psi^T S)^{-1} (\Psi^T W \Phi + S^T \Phi) \quad (10b)$$

and have used the notation $\hat{x}(k)$ for the conditional expectation $E\{x(k) | Y(k-1)\}$. Of course, $\hat{x}(k)$ represents the minimum variance one-step-ahead prediction of the state $x(k)$ and may be generated by using the well known Kalman predictor [11,3,10,13,15,19,20]

$$\hat{x}(k+1) = \Phi \hat{x}(k) + \Psi u(k) + \Phi K(k) e(k) \\ y(k) = H \hat{x}(k) + e(k) \quad (11)$$

where $\{e(k)\}$ is the innovations sequence and $K(k)$ is the optimal Kalman gain matrix. For known systems, assuming the knowledge of the measurement noise covariance R , the Kalman gain matrix may be computed from the relation

$$K(k) = P(k)H^T(HP(k)H^T + R)^{-1} \quad (12)$$

Here R is the covariance of $\{v(k)\}$, and $P(k) = E\{(x(k) - \hat{x}(k))(x(k) - \hat{x}(k))^T | Y(k-1)\}$ is the covariance of the error $\tilde{x}(k) = x(k) - \hat{x}(k)$ in the prediction $\hat{x}(k) = E\{x(k) | Y(k-1)\}$, which may be obtained by solving the Riccati equation with assumed initial condition $\hat{x}(0)$

$$P(k+1) = \Phi \left[P(k) - P(k)H^T(HP(k)H^T + R)^{-1} \times HP(k) \right] \Phi^T + \Gamma Q \Gamma^T \quad (13)$$

with Q being the covariance of $\{w(k)\}$.

Equation (10b) shows that the controller gain matrix M may be determined by solving an algebraic relation, and that the main computational burden arises from the need to multiply the various matrices involved in (10b) and to invert the $m \times m$ matrix $(\Psi^T W \Psi + U + 2\Psi^T S)$. Note that the dimension of $u(k)$ is usually much lower than that of $x(k)$ so that the inversion in this case may not be computationally very expensive. However, the Riccati equation (13) is required to be solved for generating the optimal state prediction $\hat{x}(k)$. In the next section, we shall show that in the case of an unknown system an asymptotic state prediction may be achieved after a direct estimation of the parameters of the innovations model (11), without requiring an explicit knowledge of the noise covariances.

IV ADAPTIVE MINIMUM STATE VARIANCE ERROR CONTROL

Let us consider now the case where all the system parameters of the model (1) are unknown and need to be estimated recursively before the control algorithm may be implemented. To ensure identifiability, we replace the model (1) by the steady state innovations model in observer canonical form

$$\hat{x}(k+1) = \Phi \hat{x}(k) + \Psi u(k) + \bar{\Gamma} e(k) \quad (14a)$$

$$y(k) = Hx(k) + e(k) \quad (14b)$$

where the matrices Φ and H are assumed to have the following form

$$\Phi = \begin{bmatrix} -a_1 & & & & \\ & \ddots & & & \\ & & I_{n-1 \times n-1} & & \\ & & & \ddots & \\ & & & & -a_n \end{bmatrix}; H^T = \begin{bmatrix} 1 \\ 0 \\ \vdots \\ 0 \end{bmatrix} \quad (14c)$$

with Ψ and $\bar{\Gamma}$ being the general $n \times 1$ vectors, respectively. Let us assume that these matrices are given by

$$\Psi = \begin{bmatrix} \Psi_1 \\ \vdots \\ \Psi_n \end{bmatrix}; \bar{\Gamma} = \Phi K = \begin{bmatrix} \bar{\gamma}_1 \\ \vdots \\ \bar{\gamma}_n \end{bmatrix} \quad (14d)$$

Note that there is no loss of generality in such a canonical choice of the matrices Φ and H in view of the assumed observability property of the system. Note also that the matrix H has no unknown element, while the number of unknown elements in Φ is reduced to n only. In addition, the vectors Ψ and $\bar{\Gamma}$ may have all non-zero elements which need to be estimated along with the n non-zero elements of Φ .

The problem of parameter estimation of observer state space form (14) may be solved by taking advantage of the fact that the model (14) may be equivalently expressed in the form of a n dimensional autoregressive moving average model with exogenous input, the so-called ARMAX model, given below by [17,18,21,22]:

$$A(q^{-1})y(k) = B(q^{-1})u(k) + D(q^{-1})e(k) \quad (15a)$$

where q^{-1} is the unit delay operator. The polynomials A , B and D have the following forms

$$A(q^{-1}) = 1 + \sum_{i=1}^n a_i q^{-i}; B(q^{-1}) = \sum_{i=1}^m b_i q^{-i} \quad (15b)$$

$$D(q^{-1}) = 1 + \sum_{i=1}^n d_i q^{-i}$$

The coefficients a_i, b_i and $d_i; i = 1, \dots, n$ are easily obtained from the elements of the matrices Ψ and $\bar{\Gamma}$; that is [17,18]

$$\Psi_i = b_i; \bar{\gamma}_i = d_i - a_i; i = 1, \dots, n \quad (16)$$

It is easy to check that the assumption (A2) implies that the polynomials A and D are stable (they have all their roots inside the unit circle). Moreover, it is possible to express the ARMAX form (16) in the following linear regression form

$$y(k) = Z^T(k)\Theta + e(k) \quad (17a)$$

where Θ is the vector of unknown parameters given as

$$\Theta^T = [a_1, \dots, a_n, b_1, \dots, b_n, \bar{\gamma}_1, \dots, \bar{\gamma}_n] \quad (17b)$$

and $Z(k)$ is the regression vector containing appropriate set of past outputs, inputs and innovations

$$Z^T(k) = [-y(k-1), \dots, -y(k-n), \\ u(k-1), \dots, u(k-n), e(k-1), \dots, e(k-n)] \quad (17c)$$

Once the regression model (17) and (18) is obtained, a recursive estimation of the parameter vector Θ may be achieved using a number of alternative algorithms [17,18]. Here, we have made use of the pseudo-linear regression algorithm [21,22]

$$\hat{\Theta}(k) = \hat{\Theta}(k-1) + G(k)\varepsilon(k) \quad (18a)$$

$$\varepsilon(k) = y(k) - Z^T(k)\hat{\Theta}(k-1) \quad (18b)$$

$$G(k) = T(k-1)Z(k) \\ \times [1 + Z^T(k)T(k-1)Z(k)]^{-1} \quad (18c)$$

$$T(k) = T(k-1) - T(k-1)Z(k)Z^T(k)T(k-1) \\ \times [1 + Z^T(k)T(k-1)Z(k)]^{-1} \quad (18d)$$

These equations are initialized with an assumed initial estimate $\hat{\Theta}(0)$ and initial covariance $T(-1)$ and may be expected to converge to the correct parameter values under certain conditions. Namely, if the polynomials A and D are stable, and the polynomial D satisfies the strictly real-positive condition $\text{Re}\{1/D(q^{-1}) - 1/2\} > 0$, then it is possible to show that the parameter estimation algorithm (18) yields the following convergence result

$$P\left\{\lim_{k \rightarrow \infty} \Theta(k) = \Theta_0\right\} = 1$$

where Θ_0 is the true parameter vector.

Note that the parameter estimates $\hat{\Theta}(k)$ yield the corresponding estimates $\hat{\Phi}(k)$, $\hat{\Psi}(k)$ and $\hat{\Gamma}(k)$ of the matrices Φ , Ψ and $\bar{\Gamma}$ of the innovations model (14). Thus, the adaptive MSEV controller that minimizes the performance index (5) is obtained easily from (10a) and (10b) by replacing the system matrices by their estimated values. The state estimate $\hat{x}(k)$ in (10a) is obtained from the adaptive Kalman predictor (11), where the unknown system matrices Φ , Ψ and $\bar{\Gamma} = \Phi K$ are replaced by their estimates $\hat{\Phi}(k)$, $\hat{\Psi}(k)$ and $\hat{\Gamma}(k)$, respectively. The block scheme of the adaptive MSEV controller is given in Fig. 1.

It must be pointed out that the innovations sequence $\{e(k-1); k = 1, 2, 3, \dots\}$ is usually unmeasurable and, therefore, this sequence must be replaced by its estimate, given by (14b), in the regression vector (17c). Furthermore, the proposed adaptive state feedback controller is analogous in form to the LQG theory based optimal adaptive controller. However, a considerable reduction of the computational requirement has been achieved by the MSEV controller, at the cost of some performance loss, since a single stage quadratic

performance index has been minimized. The major computational requirements of the MSEV controller arises from the parameter estimation algorithm (18), which is central to the implementation of any form of adaptive controller. It is possible to show that the MSEV controller for known system will be globally asymptotically stable provided the triple $\{\Phi, \Psi, H\}$ is completely controllable and observable, and that the weighting matrices are chosen so that $W \geq 0, U > 0$ and $W - SU^{-1}S^T \geq 0$, [11]. Thus, it is important to note that the choice of weighting matrices W , S and U is not completely arbitrary and, in practice, these matrices must be bounded, constant and must satisfy assumption that the matrix $W - SU^{-1}S^T$ is positive, semi-definite, as well as that $\Psi^T S$ is a symmetric positive semi-definite matrix, in order to ensure stability.

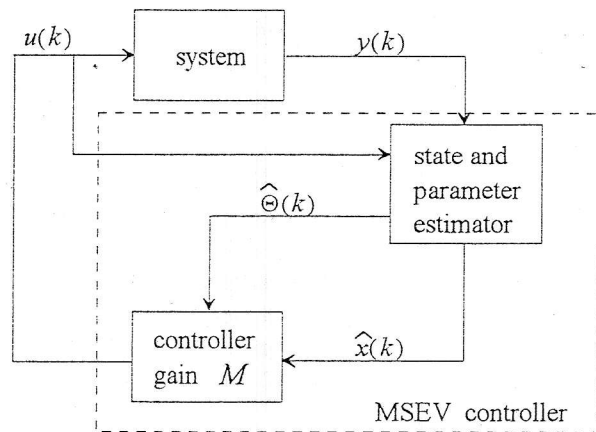


Fig. 1. An adaptive MSEV controller

V NEIGHBORING MINIMUM STATE ERROR VARIANCE CONTROLLER

The method discussed in the paper may be extended in order to design estimated state feedback controllers for nonlinear nonstationary systems with non-zero reference inputs. Some results along these lines have been discussed in the following. A scheme for a such implementation of the MSEV controller is shown in Fig. 2.

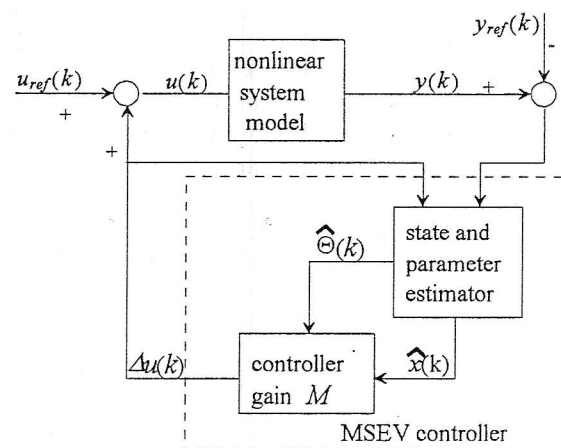


Fig. 2. A neighboring adaptive MSEV controller

Here $u_{ref}(k)$ and $y_{ref}(k)$ define a deterministic reference, or nominal, trajectory.

In practice, the reference trajectory is obtained either by developing a complex nonlinear mathematical models of the concerned system or by simulating about some reasonable operating conditions. Before we continue the discussion, consider the following example of a missile control around the state reference trajectory exposed in the literature [14]. A missile motion is described by 12 standard nonlinear differential equations given below

a) *Dynamical translatory equations in body axes:*

$$\dot{u} = -\frac{\rho V^2}{2} [C_D \cos(\alpha) \cos(\beta) + C_Y \cos(\alpha) \sin(\beta) + C_L \sin(\alpha)] + T/m - g \sin(\Theta) - qv + rv \quad (19)$$

$$+ C_L \sin(\alpha)] + T/m - g \sin(\Theta) - qv + rv$$

$$\dot{v} = -\frac{\rho V^2}{2} [-C_D \sin(\beta) + C_Y \cos(\beta)] + g \sin(\phi) \cos(\Theta) - ru + pw \quad (20)$$

$$\dot{w} = -\frac{\rho V^2}{2} [-C_D \sin(\alpha) \cos(\beta) - C_Y \sin(\alpha) \sin(\beta) + C_L \cos(\alpha)] - g \cos(\Theta) \sin(\phi) - pv + qu \quad (21)$$

$$+ C_L \cos(\alpha)] - g \cos(\Theta) \sin(\phi) - pv + qu$$

b) *Dynamical angular equations in body axes:*

$$\dot{p} = C_1 \frac{1}{2} \rho V^2 S d / A \quad (22)$$

$$\dot{q} = \left(C_m \frac{1}{2} \rho V^2 S d / B + (C - A) r p \right) / B \quad (23)$$

$$\dot{r} = C_n \frac{1}{2} \rho V^2 S d / C + ((A - B) p q) / C \quad (24)$$

c) *Kinematical (Euler) equations:*

$$\dot{\phi} = p + (r \cos(\phi) + q \sin(\phi)) \tan(\Theta) \quad (25)$$

$$\dot{\Theta} = q \cos(\phi) - r \sin(\phi) \quad (26)$$

$$\dot{\psi} = (r \cos(\phi) + q \sin(\phi)) / \cos(\Theta) \quad (27)$$

d) *Transformation of ground speed from body to Earth coordinates*

$$\dot{X} = u \cos(\Theta) \cos(\psi) + v(\sin(\psi) \sin(\Theta) \cos(\psi) - \cos(\phi) \sin(\psi)) + w(\cos(\phi) \sin(\Theta) \cos(\psi) + \sin(\phi) \sin(\psi)) \quad (28)$$

$$\dot{Y} = u \cos(\Theta) \sin(\psi) + v(\sin(\phi) \sin(\Theta) \sin(\psi) + \cos(\phi) \cos(\psi)) + w(\cos(\phi) \sin(\Theta) \sin(\psi) - \sin(\phi) \cos(\psi)) \quad (29)$$

$$\dot{Z} = -u \sin(\Theta) + v \sin(\phi) \cos(\Theta) + w \cos(\phi) \cos(\Theta) \quad (30)$$

The absolute value of missile speed V , angle of attack α and angle of sideslip β are given by

$$V = \sqrt{u^2 + v^2 + w^2} \quad (31)$$

$$\alpha = \tan^{-1}(w/u); \beta = \tan^{-1}(v/u) \quad (32)$$

The parameters A , B and C in eqs. (22)-(24) are time varying, since they are dependent on the missile mass and the drag force, while the aerodynamic coefficients C_D , C_Y , C_m , C_L and C_l represent the functions of angles α and β , the angular velocities p , q , r and the angles δ_A , δ_E and δ_R . The last three angles are the input variables satisfying the bounded condition $|\delta| \leq 0.2 \text{ rad}$. Thus, in the nonlinear state space equation

$$\dot{x}(t) = f(x(t), u(t)) \quad (33)$$

where $x(t) \in R^{12}$ is the state vector defined by

$$x(t) = [u, v, w, p, q, r, \phi, \psi, \theta, X, Y, Z]^T \quad (34)$$

and $u(t) \in R^3$ is the control defined by

$$u(t) = [\delta_A, \delta_E, \delta_R]^T \quad (35)$$

where the three elements stand for aileron, elevator and rudder, respectively. The reference, or nominal, trajectory is specified in the (X, Z) plane, taking into account the flight conditions and the real capabilities of the concerned missile (see, Fig. 3).

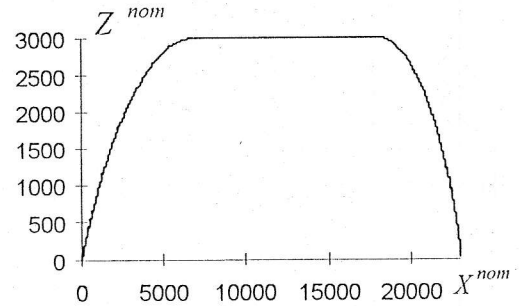


Fig. 3. The nominal trajectory

Additionally, we need to calculate the nominal control $u_{nom} = [\delta_A^{nom}, \delta_E^{nom}, \delta_R^{nom}]$ across the reference trajectory Z^{nom} . However, since the trajectory is defined in the vertical plane ($Y = 0$), it is natural to choose $\delta_R^{nom} = 0$ and $\delta_A^{nom} = 0$. The nominal control δ_E^{nom} is calculated using the strategy of predictive control. Namely, it is assumed that the control signal $\delta_E(t)$ is constant within the several sampling periods (the sampling period is chosen to be $T = 0.5s$), and then the nominal control is calculated so to minimize the deflection from the specified nominal state trajectory; that is

$$\delta_E^{nom}(kT) = \arg \min_{\delta_E} \left(Z((k+n)T) - Z^{nom}((k+n)T) \right)^2 \quad (36)$$

Here $Z((k+n)T)$ denotes the value of Z -coordinate at the instant $(k+n)T$ obtained by solving the nonlinear state-space equation (30) under the condition that the control signal $\delta_E(t)$ is constant over the n consecutive sampling periods $k, k+1, \dots, k+n-1$, respectively, and $\delta_R = \delta_A = 0$. For performing this task one can use, for example, the Runge Kutta method of the fourth or fifth order. Furthermore, one can use a gradient type procedure for solving the optimization problem (36) (this problem reduces to the task of finding the minimum of a scalar function Z of a scalar argument X). Of course, the horizon of prediction n represents a free parameter which must be chosen in advance. A smaller value of n will result into the control signal δ_E very close to the prespecified bounds $\pm 0.2 \text{ rad}$, the so-called bang-bang control signal, in order to minimize as soon as possible the deflections from the nominal trajectory. On the other hand, higher values of n will result into the control signal with smaller dynamics, which is not influenced too much by the given control bounds. However, this will yield a rather large deflections from the given nominal state trajectory. Figs. 4 and 5 depict the control signal δ_E for different values of the prediction horizon, while Fig. 6 shows the corresponding deflections from the nominal trajectory (see, Fig. 3).

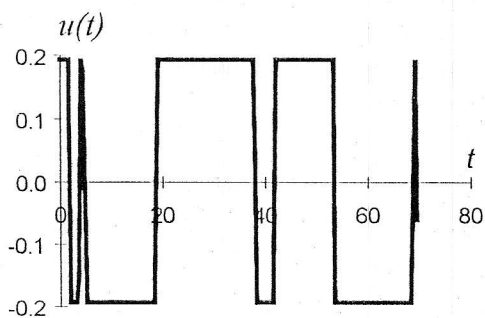


Fig. 4. The control signal for the prediction horizon $n = 2$

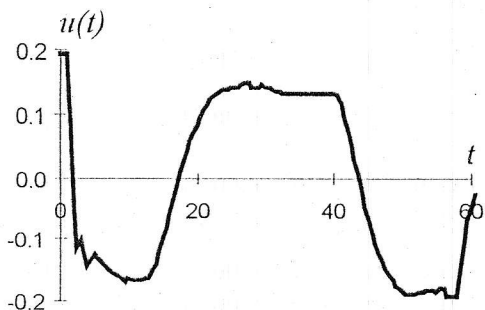


Fig. 5. The control signal for the prediction horizon $n = 8$

Thus, the choice of n represents a compromise between two opposite requirements concerning the values and dynamics of the nominal control input, and the corresponding errors in tracking the prespecified referent state trajectory. As a result of this brief experimental

analysis, we choose $n=4$. The calculated nominal control for the chosen horizon of prediction n is given in Fig. 7.

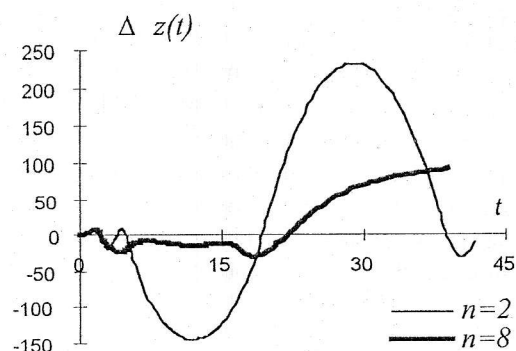


Fig. 6. Deflection from the nominal trajectory for different prediction horizons

Thus, we have defined the 12'th order nonlinear system with the one input $u_{nom}(t) = \delta_E^{nom}(t)$ and the one output $y_{nom}(t) = Z^{nom}(t)$. To perform the control task, in the sense that the system output $y(k) = Z(k)$ in Fig. 2 is to be forced by the input $u(k)$ to follow or track the reference output, $y^{nom}(k) = Z^{nom}(k)$ (see, Fig. 3), in the presence of additive measurement noise, we may use the MSEV controller (Fig. 2).

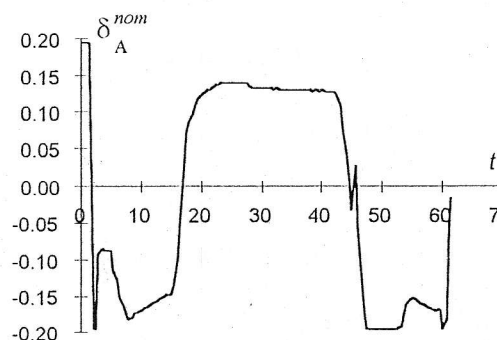


Fig. 7. The nominal control for the chosen horizon of prediction $n = 4$

The measurement noise is supposed to be zero-mean stationary white Gaussian sequence with the variance $\sigma_0^2 = 50$. The output signal $y(k) = Z(k)$ corresponding to the nominal input δ_E^{nom} is corrupted by the samples of specified measurement noise. As mentioned before, the design of MSEV controller is based on the ARMAX model (15a) of the order n . It is adopted that the order of the ARMAX model is the same as the order of the system model under consideration; that is $n = 12$. Furthermore, the weighting matrices W , S and U also represent the free parameters in the MSEV design. These matrices have to be chosen in advance, taking into account the ratio of the absolute values of the control signal $u = \delta_E$ and the elements of the state vector in (34), as well as the given physical bounds on the control input and the requirements for the global asymptotical stability of the controller. In

practice, these matrices can be chosen by simulation. As a result of a such analysis, we choose

$$W = \text{diag}\{0,0,1,0,0,0,0,0,0,0,0\} \quad (37)$$

$$S = 0.02[1,1,1,1,1,1,1,1,1,1,1]^T \quad (38)$$

$$U = 1000 \quad (39)$$

where $\text{diag}\{\cdot\}$ denotes the diagonal matrix. Fig. 8. depicts the errors in tracking the nominal state trajectory, while Fig. 9 shows the corrections of the input signal $\Delta u(k)$ (see, Fig. 2).

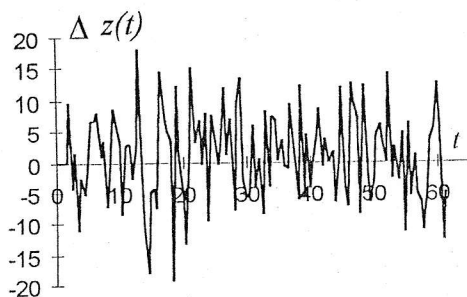


Fig. 8. The errors in tracking the nominal state trajectory

The estimated ARMAX model parameters are given in Fig. 10. The obtained results have shown that the MSEV controller has good tracking performances and possesses rather good immunity towards disturbances.

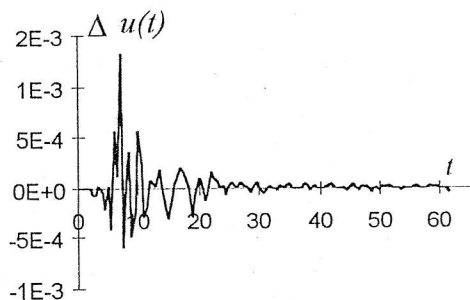


Fig. 9. The correction of the input sequence

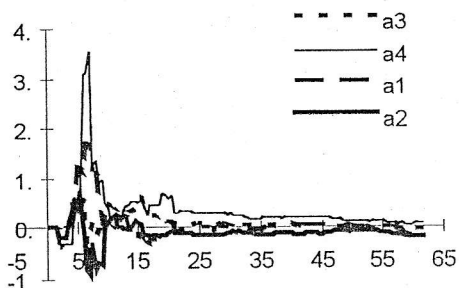


Fig. 10. The estimated ARMAX model parameters

VI CONCLUSION

A new form of the self-tuning controller has been proposed in the paper, based on the use of an innovations model in the observer canonical form, coupled with the

minimization of a single stage quadratic performance index that includes a cross-weighting on the system states and the inputs. This leads to an estimated state feedback type control law which is analogous to the optimal adaptive control law. However, the proposed controller is computationally simpler than the optimal one, since no Riccati equation need be solved either for the filter gain or for the controller gain. Making use of the equivalence of the canonical observer and the ARMAX forms of the system model, the filter gain matrix is estimated as a part of the model parameter vector, while the controller gain matrix is computed from an algebraic relation. It should be noted that the computational simplicity is a direct consequence of the single stage criterion and the direct estimation of the filter gain in the estimation algorithm through the use of the innovations model. It is not a consequence of the cross-weighting term in the performance index, but this term results in the generalization of the controller form and yields a more effective control of the adaptive system. It has been also shown that the proposed controller may represent an efficient tool for tracking a prespecified reference state space trajectory in the case of nonlinear and nonstationary system model characterized by the presence of stochastic disturbances.

REFERENCES

- [1] Anderson, B.D.O. and J.B.Moore (1979), *Optimal filtering*, Prentice Hall, New Jersey.
- [2] Anderson, B.D.O. and J.B. Moore (1971), *Linear optimal control*, Prentice Hall, New Jersey.
- [3] Astrom, K.J. (1970), *Introduction to stochastic control theory*, Academic Press, New York.
- [4] Astrom, K.J. (1983), "Theory and applications of adaptive control: A survey", *Automatica*, vol. 19, No. 5, pp. 471-486.
- [5] Astrom, K.J. and B. Wittenmark (1990), *Adaptive Control*, Addison-Wesley, New York.
- [6] Astrom, K.J and B. Wittenmark (1990), *Computer controlled systems*, Prentice Hall, New Jersey.
- [7] Clarke, D.W. and P.J. Gawthrop (1975), "A self-tuning controller", *Proc. IEE, Pt.D.*, vol. 122, No. 6, pp. 999-934.
- [8] Clarke, D.W. and P.J. Gawthrop (1979), "Self-tuning control", *Proc. IEE, Pt D.*, vol. 126, No. 6, pp. 633-640.
- [9] Desai, P. and A.K. Mahalanabis (1991), "On the design of self-tuned regulators using state space approach", *Cont. Th. Advan. Tech.*, vol. 7, No. 3, pp. 473-490.
- [10] Gelb, A. (1974), *Applied optimal estimation*, MIT Press, Cambridge.
- [11] Goodwin, G.C. and K.S. Sin (1984), *Adaptive filtering, prediction and control*, Prentice Hall, New Jersey.

- [12] Grimble, M.J. (1981), "A control-weighted minimum variance controller for non-minimum phase systems", *Int. J. Control*, vol. 33, No. 4, pp. 751-762.
- [13] Jazwinsky, A.H. (1970), *Stochastic processes and filtering theory*, Academic Press, New York.
- [14] Kolfman, M. and S. J. Merhav (1991), "Autonomously aided strapdown attitude reference system", *J. Guidance*, vol. 14, No. 6, pp. 1164-1172.
- [15] Lewis, F. L. (1986), *Optimal estimation with an introduction to stochastic control theory*, John Wiley, New York.
- [16] Lewis, F. L. (1992), *Applied optimal control and estimation*, Prentice Hall, New Jersey.
- [17] Ljung, L. and T. Soderstrom (1983), *Theory and practice of recursive identification*, MIT Press, Cambridge.
- [18] Ljung L. (1987), *System identification: theory for the user*, Prentice-Hall, New Jersey.
- [19] Meditch, J.S. (1969), *Stochastic optimal linear estimation and control*, McGraw-Hill, New York.
- [20] Stengel, R.E. (1986), *Stochastic optimal control*, John Wiley, New York.
- [21] Tsytkin, Ya. Z. (1983), *Foundations of the theory of learning systems*, Academic Press, New York.
- [22] Tsytkin, Ya. Z. (1984), *Foundations of the informational theory of identification*, Nauka, Moscow.
- [23] Warwick, K. (1981), "Self-tuning regulators: a state space approach", *Int. J. Control*, vol. 33, No. 5, pp. 839-858.

An abridged version of this paper has been presented at the XLII ETRAN Conference, Vrnjačka Banja, June 2-5, 1998.

COMPARATIVE ANALYSIS OF THE VISUAL NAVIGATION ALGORITHMS

Stevica Graovac, *Faculty of Electrical Engineering, University of Belgrade*

Abstract: A survey of the characteristic visual navigation algorithms as well as their comparative analysis from the motion parameters estimation accuracy point of view, have been given in this paper. Two basic groups of these algorithms were considered. One of them is based on an optical flow measurement, while the other one is related to the extraction and tracking of the object features. TV camera is assumed as the sensor used in both cases. The comparison has been made using the computer generated test images of a terrain

1. INTRODUCTION

Automatic navigation of objects in space is a complex task of automatic control nature. It consists from acquisition of information about the object's position (originating from the sources of different type), their processing in order to eliminate the noise as well as in generating of the appropriate commands enabling the changes of object's position in order to follow the specified trajectory.

Any type of the overall accuracy analysis of the automatic navigation procedures should include the consideration of particular influences of these three constituent parts. Initially, the nature of basic signals coming from inertial sensors, radio devices or electro-optical sensors (as it is in this particular case) should be analyzed carefully in order to identify all influences of existent imperfections and noises deteriorating the basic information. Processing of these signals is dominantly directed toward the improvement of the basic information quality, but the number of required calculations related to coordinate frame transformations are included also. The overall amount of required processing directly affects the processing time needed, leading to the another problem of dynamic nature: the influence of noise could be well eliminated, but the time required for this becomes not negligible introducing the problem of command delay. Finally, object's motion control is essentially a dynamic problem, meaning that there exist a number of other sources of delay affecting the overall accuracy of a navigation task.

The examples of visual navigation procedures are considered in this paper. This type of navigation is completely passive one. It is based on dynamic tracking of images of objects inside the scene. Supposing that the absolute positions of reference objects is known in advance it is possible to reconstruct the motion parameters of the moving object carrying the TV camera analyzing the sequence of frames produced by it.

The analysis is focused here to the image processing algorithms, their sensitivity to the image noise and final effects on the automatic navigation accuracy.

The basic concept of visual navigation procedure is explained in the second part of paper. The algorithms based on optical flow measurement (operating on the whole picture) are also explained there.

The algorithms based on feature extraction, characterized by the fact that after some kind of image segmentation just characteristic features of one or more reference objects are tracked, are considered in the third part of paper.

The fourth part consists of comparison of overall accuracy obtained by these two classes of visual navigation procedures. The results have been obtained using the same sequence of computer generated images of terrain.

The paper is concluded by the consideration of other error sources which can be treated as common ones, as well as with the suggestions for further ways of analyses and verifications of visual navigation algorithms.

2. BASIC CONCEPTS OF VISUAL NAVIGATION

The navigation based on gathering of visual information from electro-optical sensors is an attractive discipline of research and development nowadays. Rapidly growing performances of modern computer hardware enable numerous applications of this concept in industry (robots and manipulators), for different variants of obstacle avoidance task (low flying helicopters), for automatic docking - connecting of two moving objects (docking on the moving platform, linking up of two space modules), for realization of specified flight trajectory based on terrain following (remotely piloted vehicles), etc.

The basic advantages of this concept are the facts that it is fully *autonomous* (not based on active external sources of information) and *passive* (in comparison with other active systems based on radar and laser devices, the power consumption is much less as well as the probability of discovering). The basic disadvantage consists in *high sensitivity on visibility conditions* (wherever they are out of control).

The overall complexity of such a system is determined dominantly by the following two factors: 1) The number of motion degrees of freedom of the controlled object; 2) The amount of a priori information about scene elements' positions. According to the first fact, the applications are ranging from planar motion (two linear degrees of freedom) with rigidly fixed TV camera, up to the control of object's flight (three linear + three rotational degrees of freedom) with separate system of angular positioning of the platform carrying the camera relative to the body of object (usually two additional rotational degrees of freedom). The overall number of motion parameters which have to be estimated from sequence of images is correlated with the complexity of motion. Based on second criterion, the

applications are extending from a priory known positions and shapes of the scene objects up to the situation where the scene is completely unknown and the objects of interest are to be reconstructed.

The basis for all visual navigation procedures is the fact that the sequence of scene images obtained by the sensor mounted on the moving object is characterized by light variations at every picture element (pixel). These are produced as a result of changes in position of scene elements relative to moving object, motion of the object carrying the TV camera, relative position of the camera, light reflections from the scene elements and the position of light source.

Assuming that the position of light source as well as the reflections from the scene elements are constant during the observed sequence, light variations at every pixel are dependent on relative position changes only.

Where the sensor is fixed (known position and orientation) the motion parameters of moving objects inside its field of view can be reconstructed (*tracking*). If the scene elements are fixed while the object carrying the sensor is moving, its motion parameters can be determined (*navigation*). The space relationships are defined in general case by the scheme shown on Fig. 1.

The picture produced by TV camera carries the source information which is usually modeled as the light intensity distribution in its focal plane $E(x_I, y_I)$. The light intensity, E , is expressed as "level of gray" at particular pixel.

It is assumed usually that X_C axis of coordinate frame fixed to the camera passes through the origin of the 2D coordinate frame in focal plane and that the later one is parallel with the vertical plane $O_C Y_C Z_C$ at the focal distance, f .

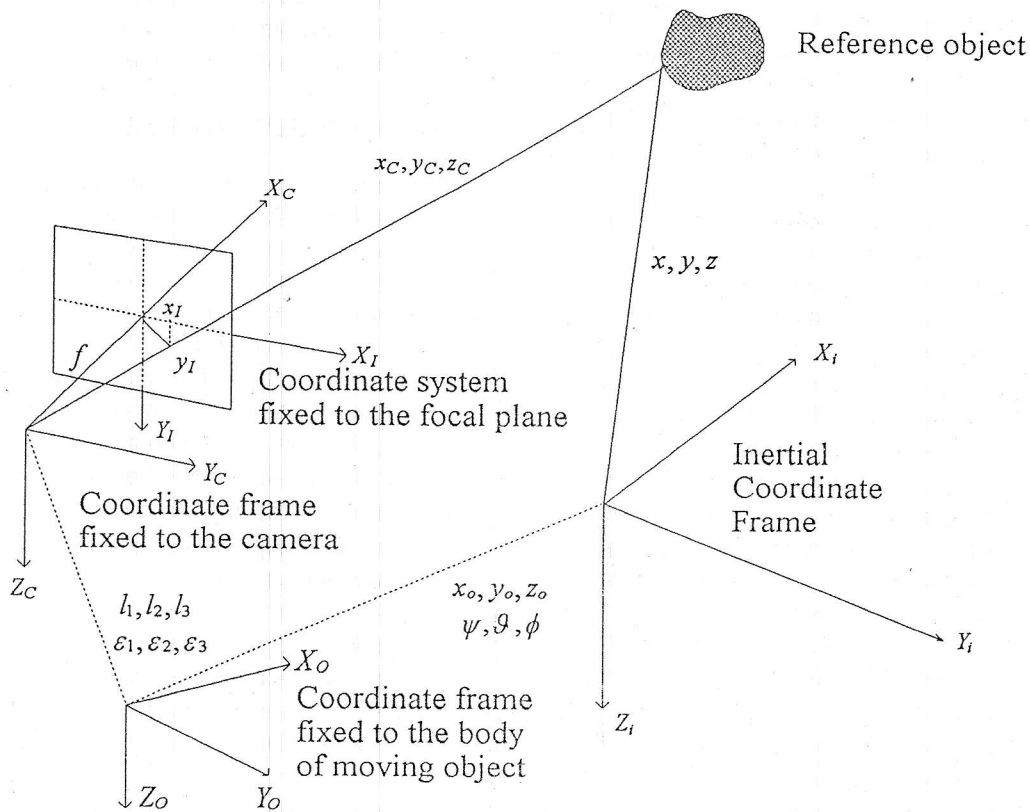


Fig. 1. Space relationships characterizing visual navigation

The origin of the coordinate frame fixed to the camera is placed in center of the optical system, at the point determined by coordinates l_1, l_2, l_3 relative to the origin of the coordinate frame fixed to the body of moving object. Angular position of the camera relative to the body axes of moving object is determined by the set of Euler angles $\epsilon_1, \epsilon_2, \epsilon_3$, corresponding to the sequence of elementary rotations about: Z_C, Y_C, X_C .

Body fixed coordinate frame is defined according to standard aircraft convention (the origin is at center of mass, X_O - along longitudinal axis, foreword, Y_O - in direction of right wing and Z_O - vertically downward, producing the right handed one).

Body orientation relative to the inertial coordinate frame is determined by the set of Euler angles of yaw (ψ), pitch (θ) and roll (ϕ). The linear position of moving

object in inertial coordinate frame is defined by the triple (x_o, y_o, z_o) .

The position of reference object (some of its characteristic points) is represented in inertial coordinate frame by the coordinates x, y, z , while the same point in camera fixed coordinate frame is represented by x_C, y_C, z_C . The characteristic point is projected in image plane at position (x_I, y_I) defined as:

$$\frac{x_I}{f} = \frac{y_C}{x_C}; \quad \frac{y_I}{f} = \frac{z_C}{x_C} \quad (1)$$

If the same point is represented in body fixed coordinate frame via triple x_R, y_R, z_R , then:

$$\begin{bmatrix} x_C \\ y_C \\ z_C \end{bmatrix} = T_1 \begin{bmatrix} x_R - l_1 \\ y_R - l_2 \\ z_R - l_3 \end{bmatrix}; \quad (2)$$

while the transformation matrix T_1 is given as the product of elementary transformations: $T_1 = T_{\varepsilon_3} T_{\varepsilon_2} T_{\varepsilon_1}$

Position vector of a reference object in body fixed coordinate frame is now

$$\begin{bmatrix} x_R \\ y_R \\ z_R \end{bmatrix} = T_2 \begin{bmatrix} x - x_o \\ y - y_o \\ z - z_o \end{bmatrix}, \quad T_2 = T_\phi T_\vartheta T_\psi \quad (3)$$

Therefore, the navigation algorithm consists in the following: Based on measurements of reference object's image position in focal plane (x_I, y_I) , known values (l_1, l_2, l_3) and measured ones $(\varepsilon_1, \varepsilon_2, \varepsilon_3)$, the position of the reference object in body fixed coordinate frame (x_R, y_R, z_R) is reconstructed. (1-2). Based on measurements of (ψ, ϑ, ϕ) and known position of the reference object in inertial coordinate frame (x, y, z) , the required position vector of the moving object (x_o, y_o, z_o) is reconstructed then. (3)

Obviously, the fact that three-dimensional space is projected into the image plane (1), makes it impossible to estimate the coordinate x_K just by one measurement.

This problem is generally solved in different ways (by stereo vision - using two or more cameras, by tracking more of characteristic points on one or more objects, or by the appropriate processing of sequence of images which is usually called "dynamic vision").

Many of the existing algorithms are based on the last mentioned approach. The basis characterizing these algorithms consists in measurement of the changes in optical flow in two consecutive images: Let $E_1(x_I, y_I)$ and $E_2(x_I, y_I)$ be two consecutive images (light intensity distributions) corresponding to the same scene. Assuming the constant reflection conditions as well as the constant position of the light source, the *correspondence hypothesis* is expressed in the following form:

$$E_1(x_I, y_I) = E_2(x_I + \Delta x_{I2}, y_I + \Delta y_{I2}) \quad (4)$$

$$E_2(x_I, y_I) = E_1(x_I - \Delta x_{I1}, y_I - \Delta y_{I1}) \quad (5)$$

If the same object is present in both images:

$$(\Delta x_{I1} = -\Delta x_{I2}, \Delta y_{I1} = -\Delta y_{I2}),$$

and by expansion in Taylor series one obtains:

$$E_1 - E_2 = \mathbf{g}_2^T \mathbf{d} + \frac{1}{2} \mathbf{d}^T \mathbf{H}_2 \mathbf{d} + \dots,$$

$$E_2 - E_1 = -\mathbf{g}_1^T \mathbf{d} + \frac{1}{2} \mathbf{d}^T \mathbf{H}_1 \mathbf{d} - \dots \quad (6)$$

The included notations stand for: \mathbf{d} - displacement vector, \mathbf{g} - light intensity gradient vector, and \mathbf{H} - Hessian matrix:

$$\mathbf{d} = \begin{bmatrix} \Delta x_I \\ \Delta y_I \end{bmatrix}; \quad \mathbf{g} = \begin{bmatrix} \partial E / \partial x_I \\ \partial E / \partial y_I \end{bmatrix};$$

$$\mathbf{H} = \begin{bmatrix} \partial^2 E / \partial x_I^2 & \partial^2 E / \partial x_I \partial y_I \\ \partial^2 E / \partial y_I \partial x_I & \partial^2 E / \partial y_I^2 \end{bmatrix}$$

In the final expression defining the required vector \mathbf{x}_o :

$$\mathbf{x}_o = \mathbf{x} - \mathbf{T}_2^T (\mathbf{T}_1^T \mathbf{x}_C + \mathbf{1}) \quad (7)$$

the vector \mathbf{x}_C appears as unknown and it can be calculated using the difference in light intensities $E_2 - E_1$ and gradients \mathbf{g}_1 and \mathbf{g}_2 .

It should be noted here that two basic problems characterize this type of algorithms: 1) Calculation of gradients is the noise sensitive operation; 2) If the task is reformulated as the requirement for reconstruction of scene structure (which is typical for obstacle avoidance applications), i.e., determination of array of vectors \mathbf{x} for known \mathbf{x}_o , the calculations should be done for all image pixels, leading to extremely high processing time requirements.

While the second problem is most frequently solved by an heuristic definition of some gradient threshold which should be exceeded as the requirement for subsequent calculations (because the high value of gradient is always the sign of discontinuities, i.e., the existence of the object on the homogeneous background), the first one is an inherent disadvantage, independently on application. Therefore, some of the estimation procedures must be applied, either for gradients, [1], or for \mathbf{x} vector itself, [2].

For the purposes of this analysis the approach used in [1] was used. It was assumed there that the light intensity distribution can be factorized in following manner:

$$E = e_1(x_I) / e_2(y_I) \quad (8)$$

so the partial derivatives' estimations can be expressed as:

$$\frac{\partial \hat{E}}{\partial x_I} = \hat{e}_2 \frac{d\hat{e}_1}{dx_I}, \quad \frac{\partial \hat{E}}{\partial y_I} = \hat{e}_1 \frac{d\hat{e}_2}{dy_I}, \dots \quad (9)$$

Now, the problem can be solved as the sequence of two one-dimensional estimation problems. N-dimensional

vector p is defined in first step, as the state of the linear dynamic process along x direction:

$$\frac{d}{dx_I} p = Ap + BE \quad (10)$$

The output of this process is defined as:

$$r = Cp + DE, \quad r = e_2 \left[\hat{e}_1 \quad \frac{d\hat{e}_1}{dx_I} \quad \frac{d^2\hat{e}_1}{dx_I^2} \right] \quad (11)$$

Similarly, the partial derivatives along y direction are estimated in the second step.

3. ALGORITHMS BASED ON OBJECT'S FEATURES EXTRACTION AND TRACKING

While the previous algorithms are convenient even for the navigation where the scene is unknown, the second group which will be considered is based on extraction of characteristic features of known reference objects. The feature could be just one point (ex., centroid), a number of characteristic points (ex., corners), straight or curved line, or segment of the surface characterizing the shape of object. After the position of features are initially determined in one image, based on some appropriate approach of correlation nature, these positions are tracked in all subsequent images. Based on this, the displacement is calculated directly and it is used in order to reconstruct moving object's motion parameters.

Independent on fact whether the image is previously binarized or multiple level gray picture is used, the existent noise affects the calculation of displacement and the overall accuracy. This noise is usually modeled as additive one, while physically it dominantly includes the thermal noise of the camera as well as the image variations due to camera vibrations

Noise $v_N(x_I, y_I)$ in image registered at time NT , on position (x_I, y_I) , is modeled as temporally and spatially stationary, white, Gaussian, of zero mean value and independent on pixel intensity:

$$E[v_i(x_I, y_I) \cdot v_j(x_I + \Delta x_I, y_I + \Delta y_I)] = \begin{cases} \sigma^2 & \text{za } \Delta x_I, \Delta y_I = 0, \quad i = j \\ 0 & \text{in all other cases} \end{cases} \quad (12)$$

The operator E stands for mathematical expectation.

The model of noisy image can be defined now as:

$$I(x_I, y_I) = E(x_I, y_I) + v(x_I, y_I) \quad (13)$$

If, as the most general case, the subset consisting of n_T pixels has been defined as the feature (ex., rectangle $n_T = n_x n_y$) the aim would be to estimate the displacement $(\Delta x_I, \Delta y_I)$ maximizing the similarity of the actual image and previous one, ie., minimizing the criterion given as sum of squared light intensity differences:

$$J = \frac{1}{n_T} \sum [I_N(x_I + \Delta x_I, y_I + \Delta y_I) - I_{N-1}(x_I, y_I)]^2 \quad (14)$$

The quality of displacement estimate can be improved if the information coming from different type of sensor are included in proper way. For example, in [3], prediction derived from Kalman state estimator applied on inertial sensors' signals was used as the initial guess of the displacement value minimizing J in (14), accelerating the overall numerical procedure in such way.

The other extreme example inside this class of algorithms is dominantly used in context of tracking of moving objects. This one is based on tracking of the position of just one characteristic point. The starting step is the extraction of object's image by some image segmentation procedure. Contrast based segmentation consists in determination of one or two light intensity thresholds optimally extracting subset of pixels belonging to the object of interest.

As a result of this procedure the binary picture consisting of two classes of pixels is obtained. One of them includes the object pixels while the other one represents the rest of picture (background). Light intensity variations across the object surface, as well as the insufficiently sharp object edges, are the usual reasons why the binarized picture should be additionally filtered using morfological filters. After these steps, the determination of the characteristic point position follows (ex., object's center of mass - centroid), and the required displacement is finally obtained as the difference of two consecutive centroid positions. Errors in the estimation of centroid position caused by image noise are minimized again by some optimal estimation procedure incorporating the dynamic model of object's motion, [4].

4. APPLICATION RESULTS OF VISUAL NAVIGATION ALGORITHMS

Testing of two typical algorithms belonging to the mentioned two groups was made using the sequence of computer generated images (Fig. 2) which is a part of material used for pilot's training [5].

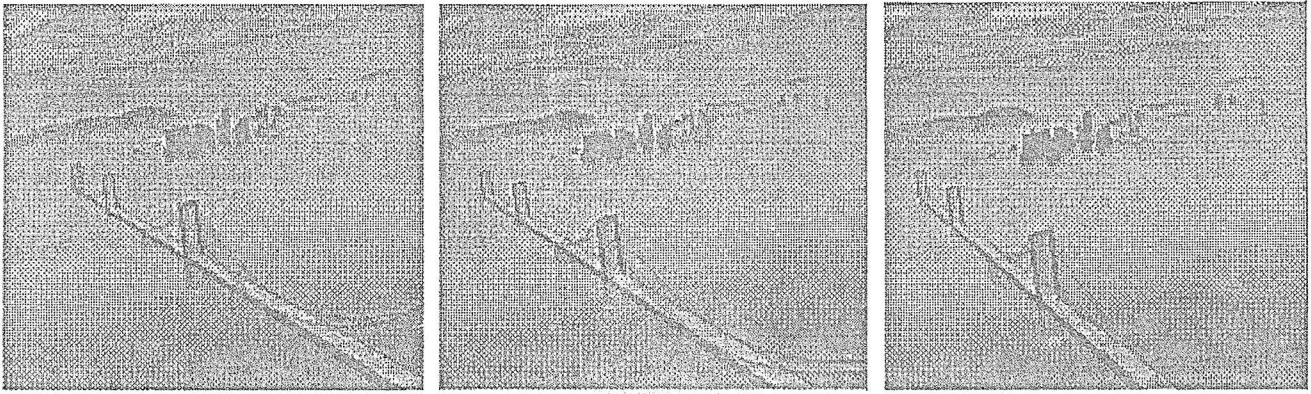


Fig. 2. Sequence of test images

The closest bridge holder was used as the reference object (gate of the size 60X80 pixels). Five frames (shifted by $\Delta T=0.5$ s) are given on Fig. 3.

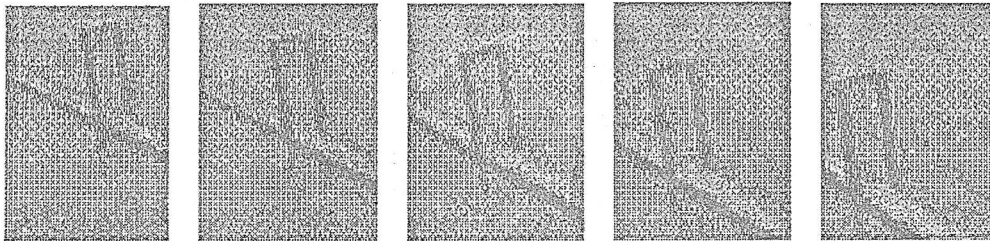


Fig. 3. Sequence of five frames including reference object

The following assumption has been made: Inertial coordinate frame (ICF) is defined with X axis along the nearer edge of the bridge, Y axis lies at the crossing of the road plane and holder plane, directed rightward, Z axis is defined as vertical, along the nearer holder pier, directed downward.

The object carrying the camera is moving horizontally, at unknown altitude, with linear velocity $V = 250$ m/s, and the azimuth angle of $\Psi = 30^\circ$. The yaw angle is assumed as $\psi = 10^\circ$, while the roll angle is $\varphi = 15^\circ$. Camera is fixed in the vertical plane of the object under the angle $\varepsilon_2 = -30^\circ$. Kinematic parameters of the moving object are constant during the observed sequence of two seconds.

The task consists in determination of the coordinate x_c of the bridge pier base (the origin of ICF) measured in camera coordinate frame (CCF). Based on this estimation and listed assumptions, the position of the moving object in ICF can be calculated directly. Calculations were made for pairs of consecutive frames, for the original images (normalized in range (0-1)) and for noisy ones. In the later cases, the zero mean Gaussian noise of standard deviations of 0.01 and 0.1 was artificially added. Having in mind that the original images are of low dynamic character (they simulate the fog ambient) the influence of added noise is high. Fig. 4. illustrates the light intensity histograms for original image and the noisy one ($\sigma = 0.01$).

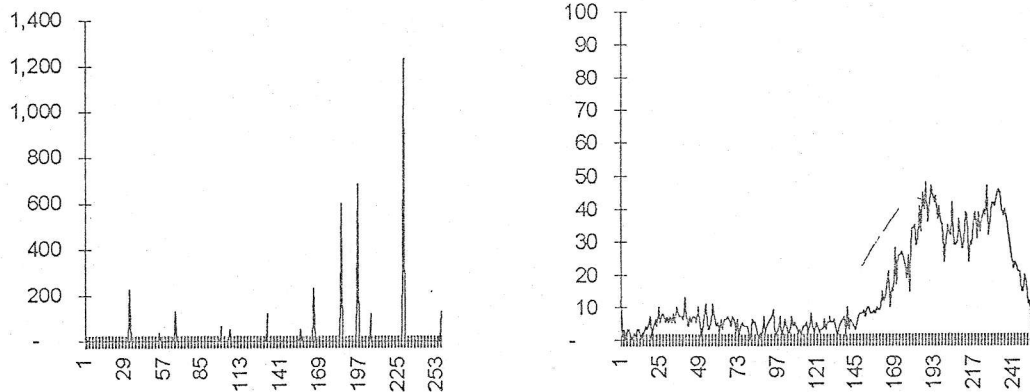


Fig. 4. Light intensity histograms of original and noisy images

Using the software package MATLAB-IMAGES, the programs for calculation of required coordinate have been made. One of them uses the optical flow measurement as the basis, while the other one is based on the estimation of displacement of the gate encompassing the reference object.

The first order Taylor expansion was used in the first case. For the estimation of the light intensity and appropriate gradients along x_I i y_I , (10-11), it was adopted: $A = C = -7$ i $B = D = 7$. Table I consists of estimations of x_C for three pairs of consecutive frames.

Table I: *Estimations obtained using the optical flow measurements*

	Original	Noise ($\sigma = 0.01$)		Noise ($\sigma = 0.1$)	
	X_C	$E(X_C)$	$dev(X_C)$	$E(X_C)$	$dev(X_C)$
1-2	957	912	120	919	237
2-3	849	843	132	801	249
3-4	768	660	105	690	180

The pixels characterized by the light intensity variation in two frames which had been less than 0.1, were eliminated during these calculations. Because it was impossible to extract just one pixel as the representative of the coordinate origin, the surrounding gate of dimensions 7×7 was considered. In order to eliminate the influence of pixels with small light intensity variation inside the gate, the maximums along the rows were calculated and after that, the median of these values was used as the measure of the range. Based on ten calculations for each pair of images, the mean values and standard deviations have been determined.

Analyzing the results obtained in the case of original images, one can see the relatively good estimation which could be proved following the range decrements (from the object's kinematics it is known that the range decrement should be -101 m). Without the complete knowledge of the kinematic parameters it is not possible to say whether these estimations are well or not. However, the very large variations can be seen for noisy images (even for the case of small noise, the standard deviation is approximately 120 m). The number of analyzed frame pairs is small, not allowing the precise conclusions, but it is sufficient to illustrate the basic problem: the extremely high sensitivity of this type of algorithms on the image noise.

The second class of visual navigation algorithms was analyzed on the same task and for the same sequence of frames, using the algorithm in which the displacement between two consecutive frames is determined by the minimization of the criterion (14). The contents of the whole gate of dimensions 11×11 around the coordinate origin was defined as the feature representing the reference object. While the displacements along x_I and y_I were previously calculated indirectly (via intensity differences and gradients), here they are determined directly. The gate

center was at position [36,41] in first frame. The maximum of similarity has been found in the following frames on positions [31,47], [26,53] and [21,59], for frames 2, 3 and 4, respectively.

Based on these results and assumed motion parameters, the sequence of values for x_C coordinate was estimated as: [997, 900, 793]. One can see the very good estimate of range dynamics (the error is 4%). Moreover, even for the Gaussian noise of standard deviation 0.2, the estimates of the gate center position do not vary more than one pixel. In this particular case that means (for assumed motion parameters and field of view) less than $1/3^\circ$, or approximately 5% of relative error in estimation of x_C . This result is extremely better than those shown in Table I.

CONCLUSION

The basic principles of visual navigation algorithms as well as the analysis of their sensitivity relative to image noise were presented in this paper. It was shown that the algorithms based on optical flow measurements are extremely noise sensitive. For the particular example of computer generated sequence of terrain images, even the very small Gaussian noise ($\sigma=0.01$) made the application impossible. Satisfactory results obtained for noiseless images (consisting from 16 discrete levels of gray) might be the sign that the preceding image segmentation could be the way of improving the accuracy.

In the case where the displacement of the reference object is obtained directly, the much higher robustness has been shown. In both cases, the overall accuracy is highly dictated by the image resolution and by the available information about the moving object's kinematics obtained from the sensors of different nature.

LITERATURE

- [1] P.K.A. Menon, G.B. Chatterji, B. Sridhar: "Electro-Optical Navigation for Aircraft", IEEE Trans. On Aerospace and Electronic Systems, Vol. AES-29, pp. 825-832, July '93.
- [2] B. Sridhar, G.B. Chatterji: "Vision-Based Obstacle Detection and Grouping for Helicopter Guidance", Journal of Guidance, Control, and Dynamics, Vol 17, No. 5, pp. 908 - 915, Sept-Oct. 1994.
- [3] Y. Oshman, B. Menis: "Maximum a Posteriori Image Registration/Motion Estimation", Journal of Guidance, Control, and Dynamics, Vol 17, No. 5, pp. 1115 - 1123, Sept-Oct. 1994.
- [4] Y. Bar-Shalom, H.M. Shertukde, K.R. Pattipati: "Use of Measurements from an Imaging Sensor for Precision Target Tracking", IEEE Trans. On Aerospace and Electronic Systems, Vol. AES-25, pp. 863-871, Nov. '93.
- [5] EVANS & SUTHERLAND, Visual Systems Solutions, CD-ROM, Vol. I, 1996.

An abridged version of this paper has been presented at the XLII ETRAN Conference, Vrnjačka Banja, June 2-5, 1998.

ИСПОЛЬЗОВАНИЕ НОВЫХ МАГНИТНЫХ МАТЕРИАЛОВ ПРИ ПОСТРОЕНИИ ДАТЧИКОВ МАГНИТНЫХ И МЕХАНИЧЕСКИХ ВЕЛИЧИН

Виталий Ничога, *отдел отбора и обработки стохастических сигналов
Физико-механического института Национальной академии наук Украины*
Олег Сокол-Кутыловский, *отдел физики магнитных явлений
Института геофизики Уральского отделения Российской академии наук*

Абстракт - В докладе рассмотрены возможности использования аморфных и нанокристаллических ферромагнитных сплавов для построения датчиков магнитных и механических величин. Проанализирован их принцип действия, схемные и конструктивные реализации, а также приведены некоторые результаты экспериментальных исследований.

1. ВВЕДЕНИЕ

Важнейшим звеном многих информационно-измерительных систем, которое в значительной степени определяет их качество, является аналоговый первичный преобразователь - датчик физических величин, который осуществляет линейное и высокоточное преобразование измеряемой величины в промежуточный параметр, например, электрическое напряжение, которое затем легко поддается дальнейшему усилению, анализу и обработке [6, 7, 8]. Такие функции выполняют рассматриваемые и анализируемые в докладе датчики для измерения вектора магнитной индукции, а также механических величин (силы, смещения, кручения и вибрации). Эти датчики используют физические явления, которые происходят в аморфных и нанокристаллических ферромагнитных сплавах под воздействием магнитного поля и механических деформаций. Изучение и анализ этих явлений, построение на этой основе нового класса относительно малогабаритных датчиков различных физических величин является перспективным направлением не только в прикладной физике, но и в технике измерений магнитных и механических величин.

2. ПРИНЦИПЫ ДЕЙСТВИЯ МАГНИТОУПРУГОГО ДАТЧИКА МАГНИТНОГО ПОЛЯ

Среди известных магнитоупругих датчиков магнитного поля наилучшие характеристики имеют датчики на основе аморфных ферромагнетиков с компенсированной продольной магнитострикцией и поперечной наведенной магнитной анизотропией [1-4].

На Рис.1 показана типовая конструкция магнито-

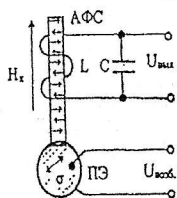


Рис.1. Магнитоупругий датчик магнитного поля с упругим возбуждением

упругого датчика магнитного поля с акустическим возбуждением аморфного ферромагнитного сердечника.

Датчик состоит из пьезокерамического или кварцевого преобразователя ПЭ, механически соединенного с ним сердечника - полоски из аморфного ферромагнитного сплава АФС с компенсированной магнитострикцией и поперечной магнитной анизотропией, и из выходного колебательного LC-контура, настроенного на рабочую частоту датчика. Катушка L выходного LC-контура расположена на сердечнике АФС в области пучности его колебаний, но не соприкасается с ним. Датчик работает следующим образом. С помощью пьезокерамического преобразователя ПЭ в аморфном ферромагнитном сердечнике создаются упругие гармонические колебания σ с частотой ω , равной или кратной собственной частоте преобразователя ПЭ. В результате магнитоупругого взаимодействия в аморфном ферромагнитном сердечнике с поперечной магнитной анизотропией во внешнем магнитном поле H_x возникают колебания вектора намагниченности. Продольная составляющая вариации вектора намагниченности вызывает в катушке L, охватывающей сердечник, э.д.с. индукции, величина которой пропорциональна продольной составляющей внешнего магнитного поля H_x .

Выходное напряжение $U_\omega(t)$ на частоте возбуждения ω может быть найдено из следующего выражения:

$$U_\omega(t) = 2\mu_0 M_s SN\omega Q\varphi_m \left(H / H_a \right) \left[1 - (H / H_a)^2 \right]^{1/2} \cdot \cos \omega t,$$

где $\mu_0 = 4\pi \times 10^{-7}$ Гн/м - магнитная постоянная; M_s - намагниченность насыщения; S - площадь поперечного сечения сердечника; N - количество витков катушки индуктивности; Q - добротность выходного LC-колебательного контура; φ_m - максимальный угол поворота вектора намагниченности под действием упругих колебаний, который пропорционален углу сдвига; H - внешнее магнитное поле и H_a - магнитное поле анизотропии.

На Рис.2 показаны экспериментальная (точки) и вычисленная по выражению для $U_\omega(t)$ (сплошная кривая) зависимости амплитуды выходного напряжения магнитоупругого датчика с сердечником из аморфного сплава $Fe_3Co_{70}Si_{13}B_{10}$ с компенсированной продольной магнитострикцией и поперечной наведенной магнитной анизотропией. Некоторое отличие вычисленной кривой от экспериментальных точек объясняется тем, что при выводе выражения для $U_\omega(t)$ полагалось, что вектор намагниченности не выходит из плоскости ферромагнитной ленты.

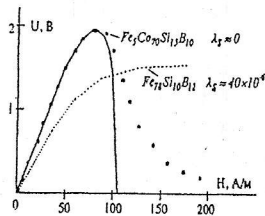


Рис.2. Зависимость амплитуды выходного напряжения магнитоупругого датчика от величины магнитного поля

Здесь же показана аналогичная зависимость для магнитоупругого датчика с сердечником из магнитоупругого аморфного сплава $Fe_{78}Si_{10}B_{12}$ (пунктирная кривая). Чувствительность магнитоупругого датчика с сердечником из аморфного сплава с компенсированной продольной магнитоупругостью и поперечной наведенной магнитной анизотропией при амплитуде напряжения возбуждения на пьезопреобразователе 1В составляет от 5 до 50 мкВ/нТл, что почти в два раза выше, чем в датчике из магнитоупругого аморфного сплава.

3. МАГНИТОИМПЕДАНСНЫЙ И МЕХАНОИМПЕДАНСНЫЙ ЭФФЕКТЫ - ОСНОВА ПОСТРОЕНИЯ ДАТЧИКОВ МАГНИТНЫХ И МЕХАНИЧЕСКИХ ВЕЛИЧИН.

Принцип действия этих датчиков базируется на использовании так называемого гигантского магнитоимпедансного эффекта (ГМИЭ) в некоторых ферромагнитных сплавах. Сущность этого эффекта заключается в том, что при прохождении переменного тока через ленты, пленки и микропровода из аморфных ферромагнитных сплавов под действием постоянного продольного магнитного поля происходит существенное изменение их импеданса. Этот ГМИЭ вызвал большой интерес у исследователей магнитных материалов и у разработчиков измерительной техники. Предполагается, что на его основе могут быть созданы датчики магнитного поля, например, для устройств автоматизации, аппаратуры считывания сигналов с магнитных дисков для хранения информации, а также датчики механических величин, например, силы, смещения, кручения и вибрации [9].

Основная схема наблюдения магнитоимпедансного эффекта в проводниках из аморфных ферромагнитных сплавов показана на Рис.3. Генератор высокой частоты G через ограничивающий резистор R переменного тока нагружен на проводник из аморфного сплава. Измеряется падение напряжения U переменного тока на этом ферромагнитном проводнике, которое при неизменной амплитуде электрического тока пропорционально импедансу Z проводника. При $R \gg Z$ изменение падения напряжения на ферромагнитном проводнике можно считать изменением его импеданса. Под действием внешнего продольного магнитного поля H_x падение переменного напряжения $U(H_x)$ изменяется и, соответственно, изменяется импеданс $Z(H_x)$ ферромагнитного проводника. На Рис.4 показано относительное изменение падения напряжения на ленте

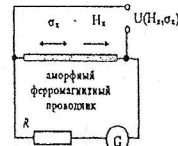


Рис.3. Основная схема измерения магнитоимпедансного эффекта

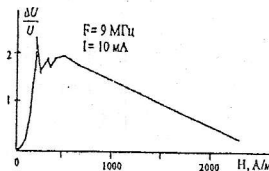


Рис.4. Зависимость относительного изменения падения напряжения на ленте из аморфного сплава от величины внешнего магнитного поля

аморфного сплава $Fe_{78}Si_{10}B_{12}$ после отжига ленты в поперечном магнитном поле.

Импеданс аморфного ферромагнитного проводника изменяется не только под действием внешнего постоянного продольного поля, но и при воздействии на проводник механического напряжения σ_x . То есть падение переменного напряжения $U(H_x, \sigma_x)$ на аморфном проводнике является функцией внешнего магнитного поля H_x и механического напряжения σ_x (Рис.3), причем влияние механического напряжения на изменение максимальной величины импеданса может преобладать над действием продольного магнитного поля. На Рис.5 приведены экспериментальные зависимости, показывающие влияние растягивающего механического напряжения на падение электрического напряжения (или импеданс) на ленте аморфного ферромагнитного сплава $Fe_3Co_{70}Si_{13}B_{10}$. Следует отметить, что изгиб ленты и ее кручение также вызывают изменение амплитуды напряжения на проводнике.

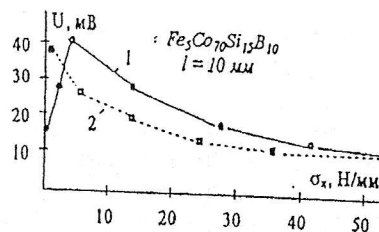


Рис.5. Зависимость падения напряжения на ленте из аморфного сплава от величины растягивающего механического напряжения

Сплошная кривая 1 на Рис.5 соответствует ненапряженной ленте (лента после отжига), а пунктирная кривая 2 - ленте с внутренними механическими напряжениями (лента без термообработки).

Максимальное значение изменения падения напряжения (или соответствующее изменение импеданса) в аморфных сплавах с поперечной и

продольной наведенной магнитной анизотропией под действием магнитного поля и механического напряжения имеет примерно один порядок. При этом, в подавляющем большинстве случаев, в лентах аморфных ферромагнитных сплавов механическое напряжение оказывает большее влияние на максимальную величину изменения импеданса, чем воздействие внешнего магнитного поля.

4. НЕКОТОРЫЕ РЕЗУЛЬТАТЫ ЛАБОРАТОРНЫХ ИССЛЕДОВАНИЙ

Лабораторные макеты магнитоупругих датчиков магнитного поля на базе сердечников из аморфных сплавов имеют следующие основные характеристики:

- при частоте возбуждения $200 \text{ кГц} \pm 1 \text{ МГц}$ диапазон частот измеряемого магнитного поля может быть от 0 до $1 \pm 10 \text{ кГц}$;
- порог чувствительности на частотах выше 1 Гц составляет $10 \pm 30 \text{ нТл} \cdot \text{Гц}^{-0.5}$ при длине аморфного сердечника датчика $5 \pm 10 \text{ мм}$;
- чувствительность до 150 мкВ/нТл ;
- потребляемая датчиком электрическая мощность 1 мВт ;
- диапазон измеряемых магнитных полей $\pm 2,5 \cdot 10^{-4} \text{ Тл}$;
- масса датчика в сборе (без электроники) может составлять $5 \pm 10 \text{ г}$.

Погрешности датчика по переменному току в основном определяются электронной схемой, а в постоянном магнитном поле определяются сдвигом петли гистерезиса и зависят от магнитных характеристик аморфного сплава и его доменной структуры после термообработки.

Преимущества датчика - малые размеры, низкая потребляемая мощность, постоянство чувствительности в рабочем диапазоне частот.

К недостаткам датчика следует отнести повышенную чувствительность к акустическим шумам и вибрациям, недостаточно низкий порог чувствительности и низкую технологичность изготовления элементов датчика.

На Рис.6 приведена блок-схема трехкомпонентного датчика магнитной индукции [5] с порогом чувствительности по полю не хуже $0,01 \text{ нТл} \cdot \text{Гц}^{-0.5}$ в интервале частот $10 \pm 300 \text{ Гц}$.

Представленный измеритель состоит из блока датчиков БД для измерения трех компонент поля, усилителей У, фазовых детекторов ФД, электронных регуляторов ЭР, генератора возбуждения ГВ и коммутатора каналов КК. В свою очередь каждый из 3-х датчиков состоит из: 1 - пьезопреобразователя, 2 - сердечника из аморфного ферромагнитного сплава, 3 - приемной катушки, 4 - катушки обратной связи, 5 - медного экрана, 6 - изолирующей прокладки.

Отличительной особенностью описанного измерителя является то, что для уменьшения нелинейности его выходной характеристики в схему введена в каждом канале отрицательная обратная связь по магнитному полю, состоящая из катушки обратной связи 4 и электронного регулятора ЭР.

Гигантский магнитоимпедансный эффект, который описан в предыдущем разделе, позволяет также создать

разнообразные датчики магнитного поля. При этом это могут быть в первую очередь датчики для измерения магнитных полей средней интенсивности.

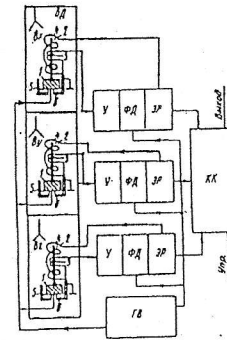


Рис.6. Блок-схема трехкомпонентного датчика магнитной индукции с упругим возбуждением

В качестве примера на Рис.7 показана конструкция магнитоимпедансного датчика, предназначенного для съема информации с магнитного диска.

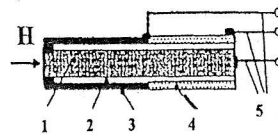


Рис.7. Магнитоимпедансный датчик для считывания информации с магнитного диска

Магнитоимпедансный элемент 1 в этом датчике выполнен на аморфном ферромагнитном проводнике диаметром $5 \pm 30 \text{ мкм}$, который покрыт диэлектрическим покрытием 2, на которое с одной стороны нанесено неферромагнитное покрытие 3, а с другой - резистивное покрытие 4. Выводы 5 служат для подключения питающего генератора и измерительного прибора согласно схеме, представленной на Рис.1.

Чувствительность лучших магнитоимпедансных датчиков постоянного магнитного поля составляет $0,5 \pm 20 \text{ мкВ/нТл}$ на узком участке возрастающей ветви характеристики при подходе к максимуму изменения импеданса. На спадающей ветви характеристики чувствительность на один-два порядка ниже.

К недостаткам датчика магнитного поля на основе магнитоимпедансного эффекта относятся чувствительность к механическим воздействиям, большая величина гистерезиса, необходимость в магнитном поле смещения или соответствующем механическом напряжении.

К положительным моментам можно отнести возможность создания датчика без использования катушек индуктивности, относительную простоту датчика. Магнитоимпедансные датчики магнитного поля могут найти достойное применение в различных технических устройствах при работе в диапазоне средних магнитных полей от $2 \cdot 10^{-5}$ до $2,5 \cdot 10^{-2} \text{ Тл}$.

Имеющаяся сильная зависимость импеданса проводника из аморфного ферромагнитного сплава от приложенного к этому проводнику механического напряжения (растяжения, сжатия, кручения, изгиба и их

комбинации, например, точечное давление на участок аморфной ферромагнитной ленты) позволяет создать малогабаритные датчики механических величин, которые не содержат катушек индуктивности (Рис.8)

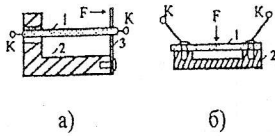


Рис.8. Некоторые конструкции чувствительного элемента датчиков силы: а) с упругим и б) с жестким креплением аморфного проводника

В обоих возможных вариантах конструкции датчиков силы, давления или смещения аморфный ферромагнитный проводник 1 закреплен на диэлектрической жесткой подложке 2. К концам ферромагнитного проводника припаяны контакты К-К. Механические усилия передаются на ферромагнитный проводник либо через упругий элемент крепления 3 (Рис.8а), либо непосредственно через толкатель (Рис.8б).

Разрешающая способность магнитоимпедансного датчика по механическому напряжению на участке подъема импеданса $\sim 10^4 \div 10^5 \text{ Н/м}^2$. Это значительно меньше, чем в магнитоупругом датчике силы на основе аморфного сплава. Максимальное значение механического напряжения на конце участка характеристики достигает $\sim 3 \cdot 10^8 \text{ Н/м}^2$.

Магнитоимпедансные датчики имеют выходной сигнал в виде амплитуды переменного напряжения высокой частоты и поэтому могут иметь плоскую амплитудно-частотную характеристику в диапазоне частот от 0 до единиц МГц. Серьезным преимуществом механических датчиков на основе магнитоимпедансного эффекта перед тензорезисторами является их высокая температурная стабильность. В отличие от магнитоэлектрических механических датчиков механические датчики на основе магнитоимпедансного эффекта могут иметь значительно более высокую чувствительность, так как максимум изменения сигнала $\Delta U/U$, соответствующий $\Delta I/I$ или $\Delta \sigma/\sigma$ имеет место на начальном участке характеристики магнитоимпедансного эффекта, когда $\Delta I/I$ в результате продольной магнитоэлектрики составляет лишь сотые доли от величины магнитоэлектрики насыщения.

К недостаткам механических датчиков на основе механоимпедансного эффекта можно отнести влияние внешних магнитных полей, влияние электрического соединения и элементов крепления.

5. ВЫВОДЫ

1. Показана возможность создания малогабаритных датчиков магнитных полей при использовании магнитоупругого взаимодействия в ферромагнитном сплаве с компенсированной магнитоэлектрикой. Дальнейшие исследования в этой области имеют огромную перспективу и позволят в ближайшем времени разработать датчики, конкурентоспособные,

например, с индукционными датчиками для измерения весьма слабых магнитных полей.

2. Впервые обоснованы технические решения, позволяющие создать разнообразные датчики механических величин на основе механоимпедансного эффекта в аморфных и нанокристаллических ферромагнитных сплавах.

ЛИТЕРАТУРА

- [1] О.Л.Сокол-Кутыловский, "Магнитоизмерительные преобразователи на основе магнитоупругого взаимодействия в аморфных ферромагнетиках", *Измерительная техника*, 1991, № 1, с. 35-37.
- [2] P.I. Nikitin, A.N.Grigorenko, O.L. Sokol-Kutylovskij, A.K. Zvezdin, M.K. Zvezdin, "Magnetic-field Sensors for Non-disturbing and Wide-band Measurements", *Sensors and Actuators*, vol. A32, 1992, pp.671-677.
- [3] A. Pantinakis, D.A. Jackson, "High-sensitivity Low-frequency Magnetometer Using Magnetostrictive Primary Sensing and Piezoelectric Signal Recovery", *Electronics letters*, vol.22, 1986, № 14, pp.737-738.
- [4] M.D. Mermelstein, "A Magnetoelastic Metallic Glass Low Frequency Magnetometer", *IEEE Trans. Magn.* vol.28, 1992, №1, pp.36-56.
- [5] О.Л.Сокол-Кутыловский, "Трехкомпонентный преобразователь магнитной индукции", *Дефектоскопия*, 1989, № 4, с.83-85.
- [6] В.Ничога, "Измерение весьма слабых низкочастотных магнитных полей в геофизических и космических исследованиях", *Отбор и обработка информации*, вып. 9, 1993, с.70-77.
- [7] V.Tsybulsky, V.Nichoga, A.Gnatyuk, P.Dub, A.Yasinovy, "Wide-band Component Converters for Magnetic Field Measurement in Space", in *Proc. of the IV-th International Seminar on Manufacturing of Scientific Space Instrumentation*, vol.VIII, 1989, pp.3-14.
- [8] V.Nichoga, P.Dub, "High Sensitive Microlocal Sensors for Investigation and Control of Electromagnetic Compatibility of Precision Electrotechnical and Electronic Devices", in *Proc. of the I-th International Symposium on Microelectronics Technologies and Microsystems*, 1997, pp.37-42.
- [9] О.Л.Сокол-Кутыловский, "Исследование магнитоупругого взаимодействия в аморфных ферромагнетиках с целью их применения в магнитных и механических датчиках", *Автореферат диссертации на соискание ученой степени доктора технических наук*, Екатеринбург, 1997, 40 с.

Abstract- The possibilities of application of amorphous and nanocrystalline alloys for elaboration of magnetic and mechanical sensors are considered in the paper. The functioning principle and the scheme and constructive realization of such sensors are analyzed. Some results of experimental investigations are presented.

Application of New Magnetic Materials for
Elaboration of Magnetic and Mechanical Sensors
Vitalij Nichoga, Oleg Sokol-Kutylovskij

COMPARATIVE ANALYSIS OF MS LATCHES AND FLIP-FLOPS FOR HIGH-PERFORMANCE AND LOW-POWER VLSI SYSTEMS

Vladimir Stojanovic and Vojin Oklobdzija*
University of Belgrade, Yugoslavia, *Integration, Berkeley, CA, USA

Abstract - In this paper we propose a set of rules for consistent estimation of the real performance and power features of the latch and flip-flop structures. A new simulation and optimization approach is presented, targeting both high-performance and power budget issues. The analysis approach reveals the sources of performance and power consumption bottlenecks in different design styles. Certain misleading parameters have been properly modified and weighted to reflect the real properties of the compared structures. Furthermore, the results of the comparison of representative latches and flip-flops illustrate the advantages of our approach and the suitability of different design styles for low-power and high-performance applications.

1. INTRODUCTION

Interpretation of published results comparing various latches and flip-flops has been very difficult because of different simulation methods used for generation and presentation of results. Certain approaches, [1], [2], etc., did not illustrate real performance and power features of the presented structures. The main reason for that was the improper consideration and weighting of relevant parameters. In this paper we establish a set of rules in order to make comparisons fair and realistic: first, definition of the relevant set of parameters to be measured and rules for weighting their importance; and second, a set of relevant simulation conditions, which emphasise the parameters of interest. The primary goal of simulation and optimisation procedures was the best compromise between power consumption and performance, given that the limitation in performance is usually imposed by the available power budget.

2. ANALYSIS

2.1. Power Considerations

Data activity rate, α , presents the average number of output transitions per clock cycle. We have applied four different data sequences where: ...010101010..., $\alpha = 1$, reflects maximum internal dynamic power consumption; however, depending on the structure, the sequence ...111111... can in some cases dissipate more power. Pseudo-random sequence with equal probability of all transitions (data activity rate $\alpha = 0.5$) is considered to reflect the average internal power consumption given the uniform data distribution. Sequence: ...111111..., $\alpha = 0$, reflects the power dissipation of precharged nodes while ...000000..., $\alpha = 0$, reflects leakage power consumption and power spent on internal clock processing.

Dynamic power consumption can be estimated by:

$$P_d = fC_{eff}V_{dd}^2 \quad , \quad \text{where } C_{eff} = \sum_{i=1}^N \alpha_i k_i C_i \quad (1)$$

- α_i is the switching probability of node i (in regard to the clock cycle)
- k_i is the swing range coefficient of node i ($k_i = 1$ for rail to rail swing)
- C_i is the total capacitance of node i
- f is the clock frequency
- V_{dd} is the rail to rail voltage range (supply voltage)

Fig. 1 describes differences in switching activity, and therefore power consumption, for different design styles. Capacitances C_{total} , $C_{precharge}$ and C_{out} are calculated taking into account the C_i and k_i coefficient of each node in the circuit.

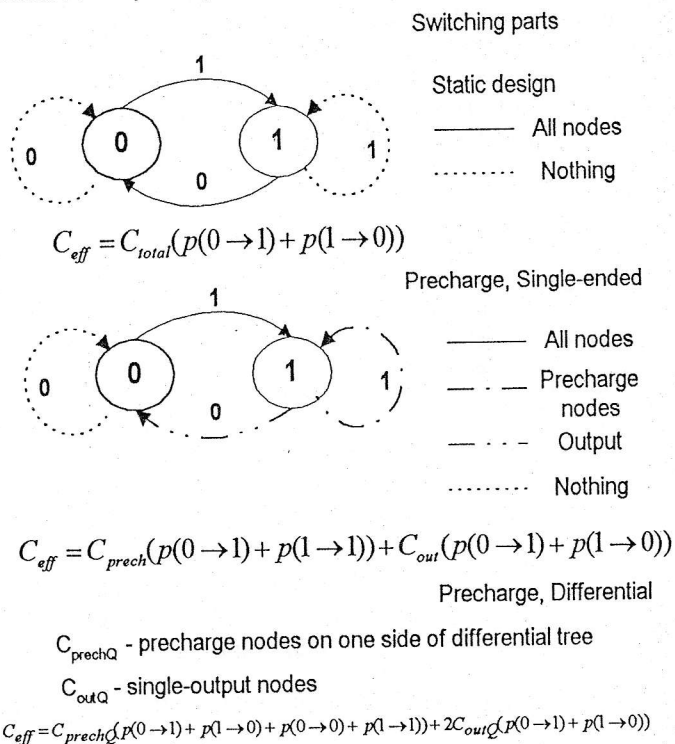


Fig. 1. Sources of internal, dynamic power consumption

Semi-Dynamic structures are generally composed of dynamic (precharged) front-end and static output part. Thus we designated two major effective capacitances: $C_{precharge}$ and C_{out} , each representing the corresponding part of the circuit. It is shown on Fig. 1 that these two capacitances have different charging and discharging activities.

Total effective precharge capacitance of semi-dynamic, differential structures is comprised of two effective capacitances of the same size: $C_{prechargeQ}$ and $C_{prechargeQb}$, which

actually represent the two complementary halves of the precharged differential tree.

We used the .MEASURE average power statement in HSPICE to measure the power dissipation of interest. Results were compared with the earlier power measurement method presented in [3] and showed the same level of accuracy.

There are three main sources of power dissipation in the latch:

- *Internal power dissipation* of the latch, including the power dissipated for switching the output loads
- *Local clock power dissipation*, presents the portion of power dissipated in local clock buffer driving the clock input of the latch
- *Local data power dissipation*, presents the portion of power dissipated in the logic stage driving the data input of the latch

The parameter *Total power* refers to the sum of all three measured kinds of power.

2.2. Timing

Stable region, Fig. 2, is the region of Data-Clk (the time difference between the last transition of Data and the latching Clock edge) axis in which *Clk-Q* delay does not depend on Data-Clk time. As Data-Clk decreases, at certain point, *Clk-Q* delay starts to rise monotonously and ends in failure. This region of Data-Clk axis is the *Metastable region*. *Metastable region* is defined as the region of unstable *Clk-Q* delay, where the *Clk-Q* delay rises exponentially as indicated by Shoji in [7]. Changes in Data that happen in the *Failure region* of D-Clk are not transferred to the outputs of the circuit.

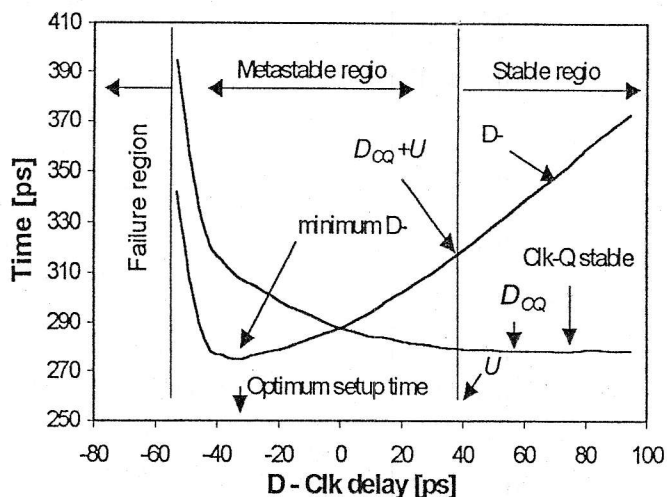


Fig. 2. StrongArm110 flip-flop, Stable, Metastable and Failure regions

The question arises of how much we can let the *Clk-Q* delay be degraded in the Metastable region and still have the increase in performance (due to the minimum in *D-Q*) and insured reliability?

D_{∞} , [6], is the value of *Clk-Q* delay, Fig. 2, in the *Stable region*, and U , [6], is the minimum point on D-Clk axis which is still a part of the *Stable region*.

In *Metastable region* *D-Q* curve has its minimum as we move the last transition of data towards the latching edge of the clock. It is clear that beyond that *minimum D-Q* point it is no longer applicable to evaluate the Data closer to the rising edge of the clock. We refer to D-Clk delay at that point as the

optimum setup time, the limit beyond which the performance of the latch is degraded and the reliability is endangered.

Our interest is to minimize the *D-Q* delay (or $D_{\infty} + U$, as defined by Unger and Tan, [6]) which presents the portion of time that the flip-flop or Master-Slave structure takes out of the clock cycle. Since $D_{\infty} + U > \text{minimum } D-Q$ (as defined in Fig. 2) it is obvious that the cycle time will be reduced if it is allowed for the change in Data to arrive no later than the *Optimum setup time* before the trailing edge of the clock.

In the light of the reasons presented above, we accepted the *minimum D-Q* delay as the *Delay* parameter of a flip-flop or Master-Slave latch.

Metastable region consists of Setup and Hold zones. Last data transition can be moved all the way to the optimum setup time. First or late data transition is allowed to come after the hold zone.

Hybrid design technique, [9], [13], [14], shifts the reference point of hold and setup time parameters from the rising edge of the clock to the falling edge of the buffered clock signal which ends the transparency period. In this way the setup and hold times measured in reference to the rising edge of the clock (as conventionally defined for flip-flops) are functions of the width of transparency period since their real reference point is the end of that period (just like in custom transparent latches).

3. SIMULATION

3.1. Test Bench

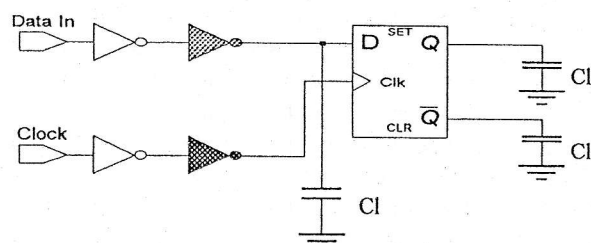


Fig. 3. The simulation test bench

Buffering inverters on Fig. 3 provide realistic Data and Clock signals, while themselves fed from ideal voltage sources. Capacitive loads simulate the fan-out signal degradation. Since buffering inverters dissipate power even without any external load (due to their internal capacitances) we made the corrections of measured power of the shaded inverters, Fig. 3, by interpolating the power over the wide range of loads. In case of the Data inverter, the correction took into account not only the inverter's intrinsic capacitance, but also the load Cl.

Parameters of the MOS model used in our simulations are shown in Table 1. For given technology, load capacitance $Cl = 200\text{fF}$ equals the load of 22 minimal inverters ($w_p/w_n = 3.2u/1.6u$). Dependence of power consumption on clock frequency appeared to be nearly linear (since the throughput was increased accordingly), so we decided to fix the frequency at 100MHz.

Table 1. MOS transistor model parameters

Technology:

Channel length	2 μm
Min. gate width	1.6 μm
Max. gate width	22 μm
$V_{tp,n}$	0.7V

MOSFET Model:

Level 28 modified BSIM Model

MOS Gate Capacitance Model:

Charge Conservation Model

Conditions:

Nominal $V_{dd}=2\text{V}$, $T=25^\circ\text{C}$

Nominal conditions	# of T's.	Total gate width [μ]	Internal power [μW]	Clock power [μW]	Data power [μW]	Total power [μW]	Delay [ps]	PDP_{tot} [fJ]
PowerPC	16	185	56	46	5	107	266	28
HLFF	20	162	126	18	3	148	199	29
SDFE	23	167	178	27	2	207	187	39
mC^2MOS	24	170	114	15	6	136	292	40
SA-F/F	19	214	137	18	3	158	272	43
StrongArm	20	215	141	18	3	162	275	45
K6 ETL	37	246	330	15	5	349	200	70
SSTC	16	147	134	22	4	160	592	95
DSTC	10	136	172	22	4	198	629	125
SSTC*	16	86	132	14	1	146	898	131
DSTC*	10	76	172	13	1	185	1060	196

4. TRANSISTOR WIDTH OPTIMIZATION

All structures were optimized both in terms of speed and power. We used the Levenberg-Marquardt optimization algorithm embedded in HSPICE. The search direction of this algorithm is the combination of the Steepest Descent and the Gauss-Newton method. A variety of other optimization algorithms is available today, like the ones presented by Yuan and Svensson, in [11] and [12]. Both algorithms will eventually lead to good results when applied to logic structures, but they do not take into account the setup time parameter and therefore the effective time taken from the cycle.

First step is the optimization of both Clk-Q delay and Total power, which essentially presents the optimization in terms of PDP with the addition of the Total power parameter. Next step is the calculation and correction of the minimum $D-Q$ taken as the Delay parameter. The problem arises in how to calculate the Delay and find the minimum PDP_{tot} in one step. Several iterations are needed to achieve satisfying results.

New automated tools are needed especially because the existing ones consider the Clk-Q delay as a relevant parameter for the optimization. If we try to optimize MS latch in terms of the classical PDP ($\text{Clk-Q} * \text{Internal Power}$) the result will be minimal Master latch optimized for low power, and Slave latch optimized for both speed and power. The "optimized" structure will have excessively large setup time thus requiring the larger clock cycle to meet the timing requirements. The reason for such result is that the optimizer does not "see" the real performance through Clk-Q delay.

5. RESULTS

We have chosen a set of representative latches and flip-flops which have been designed for use either in high-performance or in low-power processors.

Results of the simulations are shown in Table 2. Power dissipation parameters presented in Table 2 are for the pseudo-random data sequence with equal probability of all transitions.

The point of minimum Power-Delay Product exists and presents the point of optimal energy utilization. PDP_{tot} parameter is the product of the Delay and Total power parameters. We have chosen the PDP_{tot} as the overall performance parameter for comparison in terms of speed and power.

Main advantages of PowerPC 603 MS latch, Fig. 8, presented in [4], are short direct path and low-power feedback.

Table 2. General Characteristics

But, it has a big clock load which greatly influences the total power consumption on chip.

Modification of standard dynamic C^2MOS MS latch, Fig. 16, has small clock load, achieved by the local clock buffering, and low-power feedback assuring fully static operation. It is slower than PowerPC 603 MS latch. The faster pull-up in PowerPC 603 MS latch is achieved by the use of complementary pass-gates, which are less robust. Unlike classical C^2MOS structure, mC^2MOS is robust to clock slope variation due to the local clock buffering.

Milestones of hybrid-design technique are HLFF, Fig. 11, [9] and SDFE, Fig. 12, [13]. SDFE is the fastest of all the presented structures. The significant advantage over HLFF lies in very little performance penalty for embedded logic functions. SDFE's larger front-end increases the clock load, but is needed to charge large effective precharge capacitance. The size of this capacitance causes increased power consumption for data patterns with more "ones".

K6 Edge-Triggered-Latch, Fig. 13, [14], is dynamic, self-resetting, differential, hybrid structure. It is very fast but has very high power consumption independent on the data pattern.

Precharged sense-amplifier stage SA-F/F, Fig. 14, [10], and the flip-flop used in StrongArm110, Fig. 15, [8]. Have the speed bottleneck in output S-R latch stage. Uneven rise and fall times not only degrade speed but also cause glitches in succeeding logic stages, which increases total power consumption. The additional transistor in StrongArm FF, only provides fully static operation, with little penalty in power and delay.

SA-F/F, StrongArm110 FF, and self-reset stage in K6 ETL have a very useful feature of monotonous transitions at the outputs, which drive fast domino logic, [14], [15]. These structures also have very small clock load.

The SSTC* and DSTC* MS latches, Fig. 9 and Fig. 10, were simulated with minimized Master latch, as proposed in [5], and optimized Slave latch.

Using our optimization approach we got approximately 40% better results, in terms of PDP_{tot} .

Minimized Master latch in SSTC* and DSTC* suffers from substantial voltage drop at the outputs, due to the capacitive coupling effect between the common node of the Slave latch and the floating high output driving node of the Master latch. The optimized Master latch consumes more power than the minimized one but minimizes the portion of short circuit power dissipated in the Slave latch. With this

tradeoff, power remains the same and setup time is significantly reduced which leads to much better PDP_{tot} . However, the presented capacitive coupling effect along with the problems associated with the glitches at the data inputs, noted by Blair in [16], result in much worse performance and power features compared with other presented latches, even for the optimized structures SSTC and DSTC.

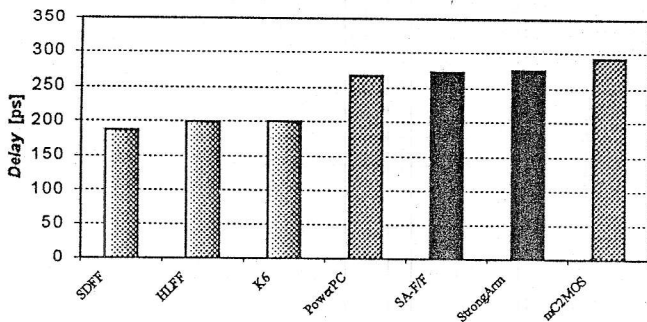


Fig. 4: Overall Delay comparison

For systems where high-performance is of primary interest, within available power budget, single-ended, hybrid, semi-dynamic designs present very good choice, given their features of negative setup time, and small internal delay. They have comparable power dissipation to Static MS latches, but much better performance.

Low-power pass-gate style used in PowerPC 603 and modified C²MOS style are good choices for designs where speed is not of primary importance.

Fig. 5 presents the ranges and distribution of PDP_{tot} for different data patterns. Symbol ■ designates the point of power dissipation (PDP_{tot}) for average activity data pattern.

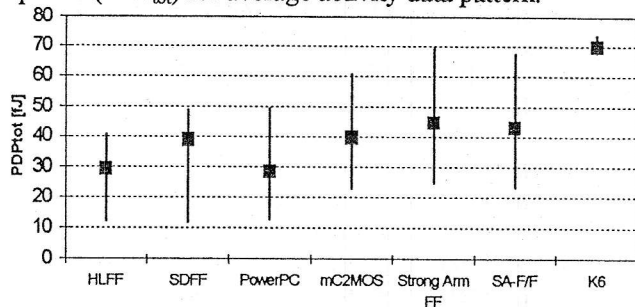


Fig. 5. Ranges of PDP_{tot}

Detailed timing parameters of the presented structures are shown in Table 3.

On the basis of our comparisons, differential structures appear to be worse than single-ended ones.

Differential structures switch for all data patterns and have doubled input and output capacitive load. Differential latches based on DCVS logic style suffer from uneven rise and fall times which can cause glitches and short-circuit power dissipation in succeeding logic stages.

Despite all described disadvantages, differential structures have the unique property of differential signal amplification. In case where logic in the pipeline operates with reduced voltage swing signals these latches have the role of signal amplifiers, i.e. swing recovery circuits, [10]. Thus, the logic in the pipeline is the party that saves power and not the latches themselves. Overall power dissipation of such pipeline structures is decreased, but latches themselves are not ideal low-

power structures, when tested solely. This is the reason why they appear to have a bad compromise between power and delay in comparison with other single-ended structures. Since the future of low-power systems lies in reduced signal swing, the importance of differential logic and latching structures is increasing.

Nominal conditions	Clk-Qhl [ps]	Clk-Qlh [ps]	Min. D-Qhl [ps]	Min. D-Qlh [ps]	Opt. Setup time [ps]
HLFF	195	191	199	155	-21
PowerPC	145	139	266	220	79
SDFE	176	176	187	143	-21
mC ² MOS	193	188	292	282	92
Strong Arm	262	162	275	171	-35
SA-F/F	262	162	272	168	-35
K6 ETL		168		200	-4
SSTC	97	301	374	592	267
DSTC	98	318	375	629	263
SSTC*	150	393	639	898	476
DSTC*	200	500	716	1060	480

Table 3. Timing parameters

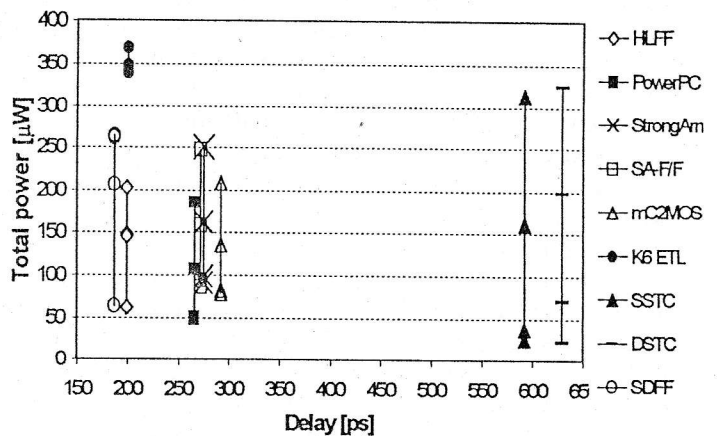


Fig. 6. Total Power range vs. Delay

On Fig. 6, hybrid structures show the best performance, as they really should, due to the negative setup time. If only $Clk-Q$ parameter is taken as the valid performance indicator, the positive setup time of the MS structures is hidden and they become comparable, if not better than hybrid ones. This is illustrated on Fig. 7, where PowerPC 603 MS latch becomes the “fastest”, mC²MOS MS latch becomes as “fast” as HLFF and DSTC and SSTC MS latches become comparable to other structures in terms of “speed”.

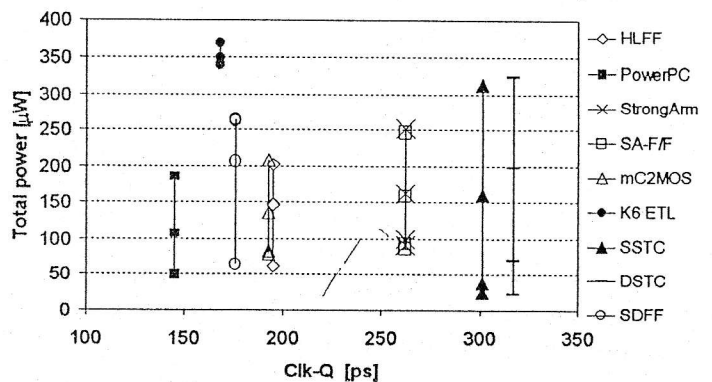


Fig. 7. Total Power range vs. $Clk-Q$

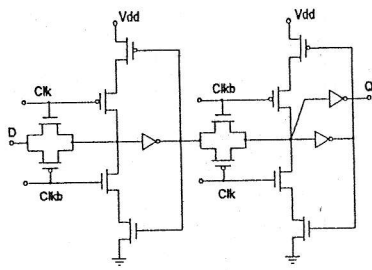


Fig. 8. PowerPC 603 MS latch

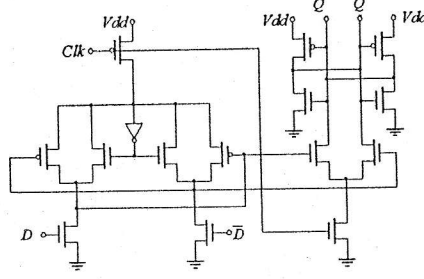


Fig. 9. SSTC MS Latch

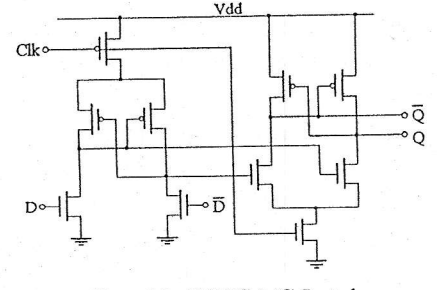


Fig. 10. DSTC MS Latch

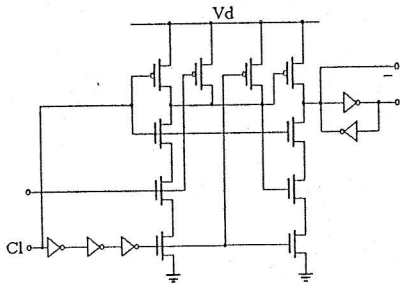


Fig. 11. HFFF

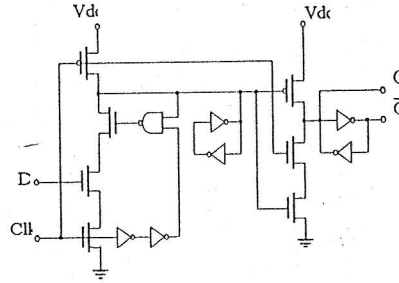


Fig. 12. SFFF

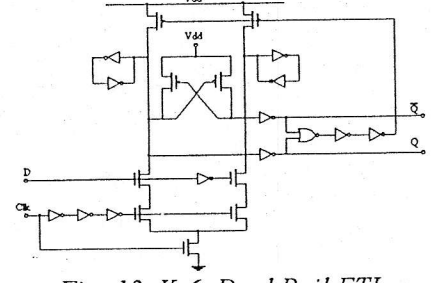


Fig. 13. K-6, Dual Rail ETL

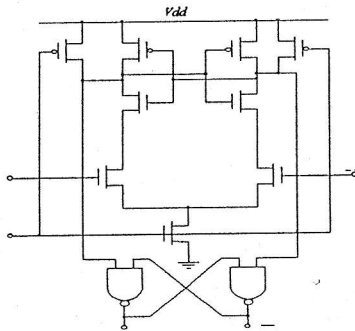


Fig. 14. SA-F/F

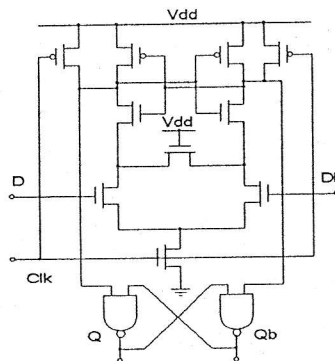


Fig. 15. SArm110 Flip-Flop

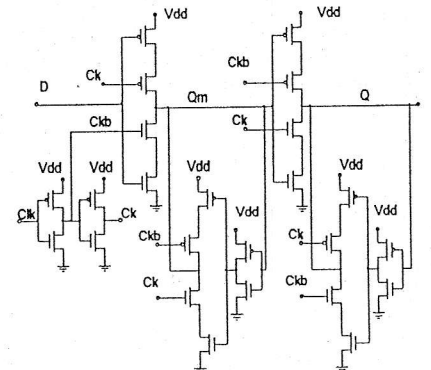


Fig. 16. mC²MOS Latch

The amount of power consumed for driving the clock inputs of each structure is shown on Figure 17.

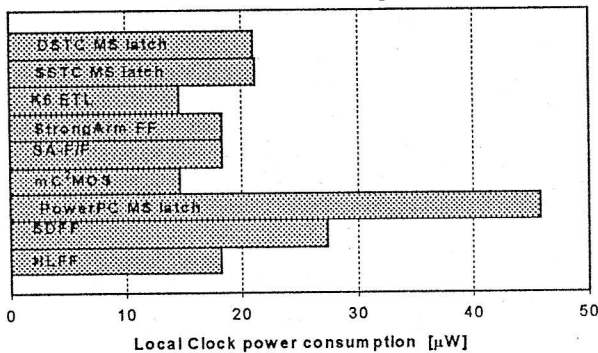


Figure 17. Local Clock power consumption

6. CONCLUSION

The problem of consistency in analysis of various latch and flip-flop designs was addressed. A set of consistent analysis approach and simulation conditions has been introduced. We strongly feel that any research of the latch and flip-flop design techniques for high-performance systems should take those parameters into account. The problems of the transistor width optimization methods have also been described. Some hidden weaknesses and potential dangers in terms of reliability of

previous timing parameters and optimization methods were brought to light.

7. ACKNOWLEDGEMENTS

Authors would like to thank Mr. Stanisha Okobdzija for his useful comments and help in language aspects of the document, to Mr. Borivoje Nikolic, Ph.D. student, UC Davis, for sharp comments and ideas on simulation and analysis procedures.

REFERENCES

- [1] U. Ko., et al., "Design techniques for high-performance, energy-efficient control logic," *ISLPED Digest of Technical Papers*, Aug. 1996
- [2] J. Yuan and C. Svensson, "Latches and flip-flops for Low Power Systems," in A. Chandrakasan and R. Brodersen, *Low Power CMOS design*, 233-238, IEEE Press, NJ 1998.
- [3] G. J. Fisher, "An Enhanced Power Meter for SPICE2 Circuit," *IEEE Transactions on Computer-Aided Design*, vol. 7, no. 5, Oct. 1986.
- [4] G. Gerosa, et al., "A 2.2 W, 80 MHz Superscalar RISC Microprocessor," *IEEE Journal of Solid-State Circuits*, vol. 29, no. 12, December 1994., 1440-1452.
- [5] J. Yuan and C. Svensson, "New Single-Clock CMOS

- Latches and Flipflops with Improved Speed and Power Savings," *IEEE Journal of Solid-State Circuits*, vol. 32, no. 1, January 1997.
- [6] S.H. Unger and C. Tan, "Clocking Schemes for High-Speed Digital Systems," *IEEE Transactions on Computers*, vol. C-35, No 10, October 1986
- [7] M. Shoji, *Theory of CMOS Digital Circuits and Circuit Failures*, Princeton University Press, Princeton NJ, 1992.
- [8] J. Montanaro, *et al.*, "A 160-MHz, 32-b, 0.5-W CMOS RISC microprocessor," *IEEE Journal of Solid-State Circuits*, vol. 31, no. 11, 1703-14., Nov. 1996.
- [9] H. Partovi, *et al.*, "Flow-through latch and edge-triggered flip-flop hybrid elements," *ISSCC Digest of Technical Papers*, Feb. 1996.
- [10] M. Matsui, *et al.* "A 200 MHz 13 mm² 2-D DCT Macrocell Using Sense-Amplifier Pipeline Flip-Flop Scheme," *IEEE Journal of Solid-State Circuits*, vol. 29, no. 12, 1482-91, Dec. 1994.
- [11] J. Yuan and C. Svensson, "CMOS Circuit Speed Optimization Based on Switch Level Simulation," *Proceedings of International Symposium on Circuits and Systems*, ISCAS 88, 1988.
- [12] J. Yuan and C. Svensson, "Principle of CMOS circuit power-delay optimization with transistor sizing," *Proceedings of International Symposium on Circuits and Systems*, ISCAS 96, vol.1, 1996.
- [13] F. Klass, "Semi-Dynamic and Dynamic Flip-Flops with embedded logic," *Digest of Technical Papers*, 1998 Symposium on VLSI Circuits, Honolulu, HI, USA, 11-13 June 1998.
- [14] D. Draper, *et al.*, "Circuit techniques in a 266-MHz MMX-enabled processor," *IEEE Journal of Solid-State Circuits*, vol. 32, no. 11, 1650-64., Nov. 1997.
- [15] B.A. Gieseke, *et al.*, "A 600 MHz superscalar RISC microprocessor with out-of-order execution," *ISSCC Digest of Technical Papers*, 176-7, 451, Feb. 1997.
- [16] G.M. Blair, "Comments on New single-clock CMOS latches and flip-flops with improved speed and power savings," *IEEE Journal of Solid-State Circuits*, vol. 32, no. 10, pp. 1610-11., Oct. 1997.

OPTICAL D-FIBRE SENSOR FOR BIOTECHNOLOGICAL APPLICATIONS

F A Muhammad*, H S Al-Raweshidy**, and J M Senior**

* *Department of Electrical and Electronic Engineering University of Hertfordshire, Hatfield,*

Herts, AL10 9AB, UK.

** *Department of Electrical and Electronic Engineering, The Manchester Metropolitan*

University, Chester Street, Manchester M1 5GD, UK.

Abstract

In contrast to previous bulk optic approaches this letter describes a novel all-fibre polarimeter for chemical sensing using D-fibre. The polarimeter is a single fibre sensor and less sensitive to environmental fluctuation in comparison with the two fibre interferometric sensor. Theoretical sensitivity calculations are developed using a finite difference method in order to provide design parameters to assist in implementation of the polarimeter. The overall retardation stability of this D-fibre polarimeter was measured to be $0.35 \times 2\pi$ rad/m/K and the phase change corresponding to the antibody protein (α HCG and α HSA) monolayers was $0.42 \times 2\pi$ demonstrating the benefits of the technique for use in biotechnological applications.

1. Introduction

Recently there has been a considerable interest in the development and use of optical fibres in the field of biosensors especially due to the possibility of *in vivo*

use [1-4]. The main advantages of single fibre optodes (optrodes) are their compactness, flexibility of use, and their extremely small size. Other potential advantages are their mechanical flexibility, their immunity to electromagnetic field variations, inexpensive construction, transmission of only low-energy radiation and good biocompatibility, so application in a catheter is one of the possibilities. Optical sensor systems range from non invasive, fast responding on-line sensors based on turbidometric methods to continuously functioning chemo- or bio-optodes. In most of the optical-fibre biochemical sensors used nowadays the fibre is only used as the lightguide from source to sensing element, which is attached at the fibre end [3]. An effective method, however, involves the use of the fibre itself as the sensing element as well as the lightguide. In this letter the feasibility of using polarisation allowed to adsorb onto 10 cm length of the D-fibre. The advantages of a polarimetric sensor compared to the two arm interferometric sensor are its simplicity and low

sensitivity to environmental fluctuations. The trade-off, however, for the polarimeter is that of lower sensitivity to the refractive index changes on the surface [4].

2. Theoretical Analysis

Dyott and Schrank [5] have shown that D-shaped cross-sectional fibre can be obtained by pulling fibre from a preform having a polished flat. The fundamental advantage of D-fibre is the closeness of the core to the flat surface of the fibre, and hence a D-fibre can be constructed which allows ready access to the evanescent field of the guided light. In the theoretical analysis it is assumed that two orthogonally polarised modes can propagate (i.e. the quasi-TE and the quasi-TM mode). The velocity of the two modes is slightly different by the virtue of the asymmetric shape of the D-fibre and its elliptical core. Moreover greater access to the bulk of the evanescent field on the surface can be achieved with smaller d-distances (flat surface/core distance). Any change in the refractive index near the surface of the D-fibre can modulate the propagation characteristics of these two modes. The sensitivity change in the refractive index profile of the two modes is different due to their differing penetration depths. Consequently any biochemical process on the D-fibre flat will modulate the polarisation of the light passing through the fibre [6].

The waveguide analysis is based on a well-established finite difference (FD) method programme which has been developed and used for several years and has been shown to produce reliable and accurate results for both planar and circular fibre geometries [7,8]. The basis of the procedure is to replace the wave equations by finite difference relations in terms of the field at discrete points. The Rayleigh Quotient is used to establish the effective refractive index n_e of the mode after each iteration [7,8].

The sensitivity of the D-fibre as an evanescent wave sensor strongly depends on three parameters; namely, the d-distance, the core diameter, and the core/cladding index difference (Δn). In [7,8] it was concluded that maximum sensitivity can be achieved by increasing (Δn) and by reducing the core diameter and d-distance taking into consideration the practical limitations. Here the calculations are limited to the commercially available D-fibre which was used in the experiments comprising a

2x4 μm core ellipse, with $\Delta n=0.036$, and $\lambda=1.33\mu\text{m}$.

The FD programme was used to model the exact shape of the D-fibre rather than using a planar waveguide approximation [6]. The programme was executed for the above parameters to evaluate the effective refractive index (n_e) for both modes. The normalised birefringence B is related to the effective refractive indices of the quasi-TE mode n_e^x , and quasi-TM mode n_e^y following [7]:

$$B = n_e^x - n_e^y \quad \dots\dots\dots (1)$$

Inserting values for the D-fibre into (1) yielded $B=4.18 \times 10^{-4}$ which was in good agreement with the actual value of the fibre. This value corresponded to approximately 0.85 nm penetration depth difference between the two modes according to:

$$d_p = 1/k_o \sqrt{n_e^2 - n_{cl}^2} \quad \dots\dots\dots (2)$$

where d_p is the penetration depth, $k_o = 2\pi/\lambda$ and n_{cl} is the cladding refractive index. The biochemical sensitivity of the D-fibre sensor depends upon the difference in penetration depth of the evanescent fields of the modes at the fibre flat. Hence the extent of the biochemical response depends upon the d-distance. Moreover it is clear that the protective silica layer and most of the cladding layer have to be removed in order to provide greater evanescent field penetration.

The geometrical birefringence calculated as a function of d-distance using (1) and the FD programme is shown in Fig. 1 (characteristic a). The outer layer (buffer solution) is assumed to have refractive index of 1.33 (water). It may be observed from Fig. 1 (characteristic a) that the maximum birefringence is achieved when the d-distance is zero and only at d-distances less than 1.5 μm does the birefringence significantly deviate from the large cladding thickness value of 2×10^{-4} . Furthermore the biochemical sensitivity behaviour can be calculated in similar manner. An adsorption of biological macromolecules

such as antibodies, with refractive index 1.45 and thickness 4 nm, was assumed [3]. Using Fig. 1 (characteristic a) the resulting increase in phase change $\Delta\Phi$ from the protein monolayer adsorption was calculated as a function of d-distance according to $\Delta\Phi = \Delta B L k_o$, where L is the D-fibre sensor length (interaction length) and ΔB is the change in birefringence caused by the process to be monitored. The increase in phase change against refractive index is presented in Fig. 1 (characteristic b). Characteristics (a and b) in Fig. 1 exhibit a similar trend and it is clear that the maximum phase change (sensitivity) can be achieved at minimum practically achievable d-distance. In addition, the phase dependence on the biochemical layer refractive index per centimetre interaction length of D-fibre was also calculated and it is depicted in Fig. 2. Moreover it is apparent from this characteristic that the phase retardation increases when using higher refractive index biochemicals.

3. Experimental Measurements

A block schematic of the D-fibre polarimeter is shown in Fig. 3. The light source comprised a temperature-stabilised pigtailed single-mode laser diode operating at a wavelength of 1300 nm. In order to obtain a biochemically sensitive polarimeter part of the cladding of the D-fibre has to be removed [7,8]. This was achieved by chemical etching (using a HF/NH₄F solution) a 10 cm interaction length of the fibre thus

providing the sensing element; the etching process being monitored on-line by counting fringes. The fibre was then removed from the solution after around half the time had elapsed for the signal to be completely faded. Hence, a fibre exhibiting half the maximum sensitivity but with a relatively high signal throughput was obtained. The remaining d-distance at half maximum birefringence was estimated to be $0.22 \mu\text{m}$ using Fig. 1 (characteristic a).

In the experiment the fibre was placed in a cuvette which was filled with a buffer solution ($n=1.33$). After a stabilisation period, the buffer was replaced by the antibody-protein (αHCG and αHSA) resulting in an adsorption process. The concentration was chosen to be high enough (4×10^{-7} Molar) to result in a monolayer of antibody-proteins on the D-fibre surface. By applying simple fringe counting measurement a phase change caused by the antibody protein monolayers of $0.42 \times 2\pi$ with $0.01 \times 2\pi$ measurement resolution was obtained which is shown in Fig. 4.

4. Conclusions

This letter demonstrates that the presence of a layer of proteins can be sensitively detected via phase change measurements using polarisation maintaining D-shaped optical fibre in an all-fibre polarimetric configuration. The adsorption of the antibodies (αHCG and αHSA) have shown to produce a phase

change of $0.42 \times 2\pi$ on a 10 cm interaction length. In order to be able to design and implement the polarimeter, a finite difference analysis have been carried out. The analysis have also been used to adjust the D-fibre parameters (index difference, d-distance, and core diameter) since the biochemical sensitivity depends strongly upon the intrinsic D-fibre parameters. Further sensitivity improvement can be achieved by using longer interaction lengths and using specially tailored D-fibre for this application using the developed FD program.

References

- [1] R G Eenink, H E de Bruijn, R P H Kooyman and J Greve, "Fibre-fluorescence Immunosensor Based on Evanescent Wave Detection", *Analytica Chimica Acta*, 1990, Vol. 238, pp 317-321.
- [2] P Claudon, M Donner, J F Stoltz, "Potential Interest of Optical Fibres as Immunosensors: Study of Different Antigen Coupling Methods", *Journal of Materials Science: Materials in Medicine*, 1991, Vol. 2, pp 197-201.
- [3] M S Abdel-Latif, A Suleiman, G G Guilbault, "Fibre-Optic Sensors: Recent Developments", *Analytical Letters*, 1990, Vol. 23, No. 3, pp 375-399.
- [4] F Maystre, R Dandliker, "Polarimetric Fibre Optical Sensor Using a Fabry-Perot Structure",

- Applied Optics, 1990, Vol. 28(11), pp 1995-2000.
- [5] Dyott and Scrank, "Self-locating Elliptically Cored Fibre with an Accessible Guiding Region", *Electronic Letters*, 1982, Vol. 18, No. 22, pp 980-981.
- [6] R G Heideman, A Blikman, R Koster, R P H Kooyman, "Polarimetric Optical Fibre Sensor for Biochemical Measurements", *SPIE Chemical and Medical Sensors*, 1991, Vol. 1510, pp. 131-137.
- [7] F A Muhammad and G Stewart, "Polarised finite difference analysis of D fibre and application for chemical sensing", *Int. Jour. of Optoelectronics*, 1992, Vol. 7, No. 6, pp. 705-721.
- [8] B Culshaw, F A Muhammad, G Stewart, S Murray, D Pinchbeck, J Norris, S Cassidy, D Williams, I Crisp, M Wilkinson, R V Ewyk, and A McGhee, "Evanescent wave methane detection using optical fibre", *Electronics Letters*, 1992, Vol. 28, No. 24, pp 2232-2234.

Figure Captions

- Fig 1. The birefringence variation (characteristic a) and phase retardation (characteristic b) as a function of d-distance.
- Fig 2. Phase variation against the refractive index n_4 .
- Fig 3. Experimental set-up.
- Fig 4. α HSA and α HCG adsorption shown as phase change measurement against time.

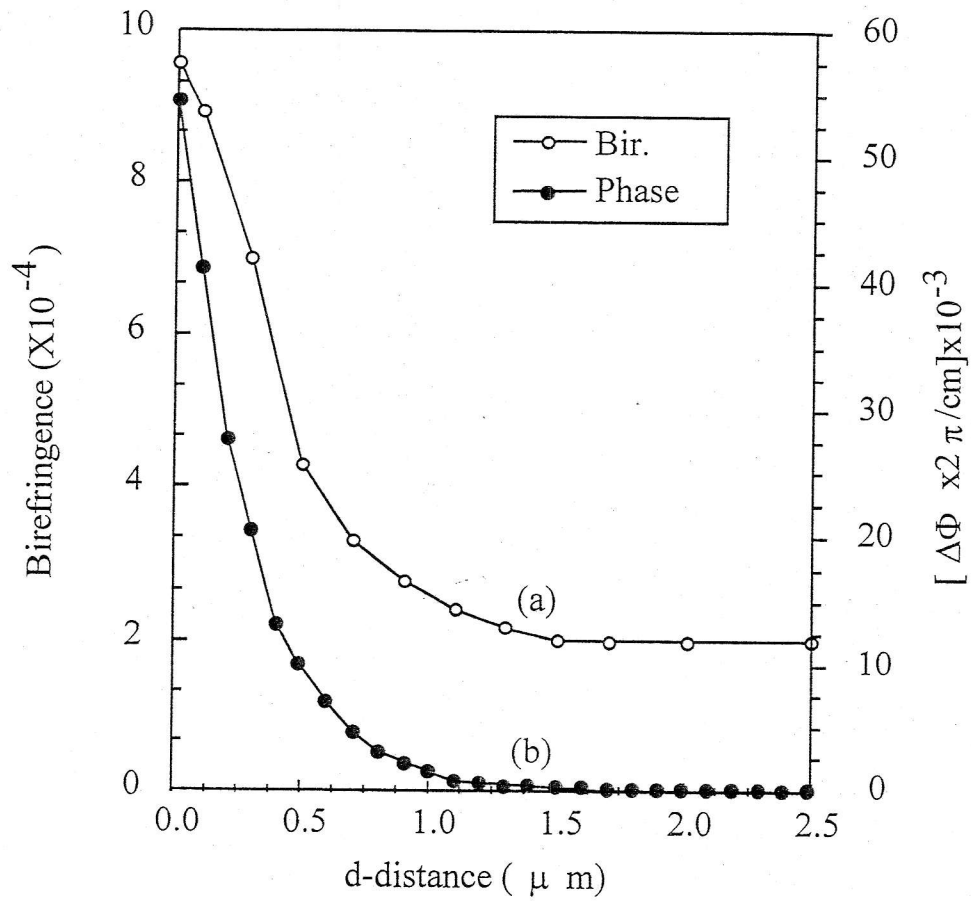


Fig 1. The birefringence variation (characteristic a) and phase retardation (characteristic b) as a function of d-distance.

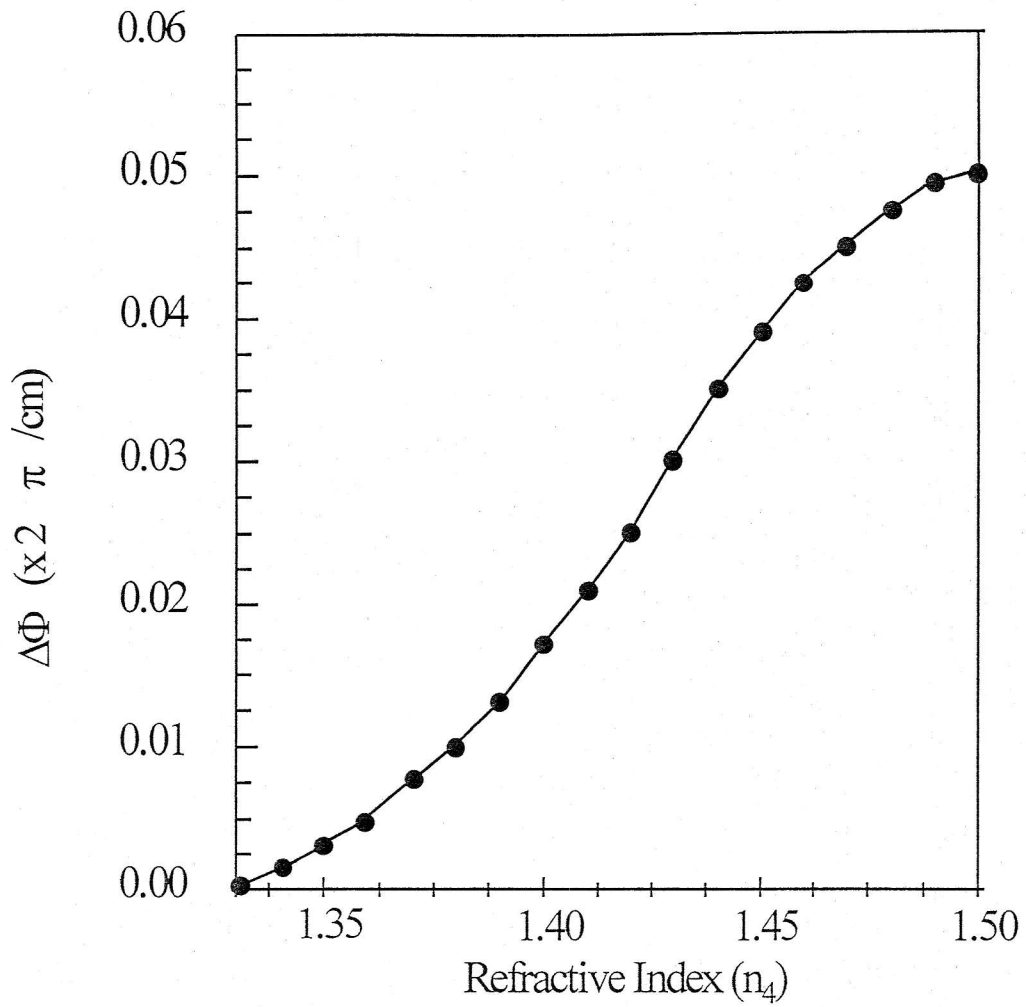


Fig 2. Phase variation against the refractive index n_4 .

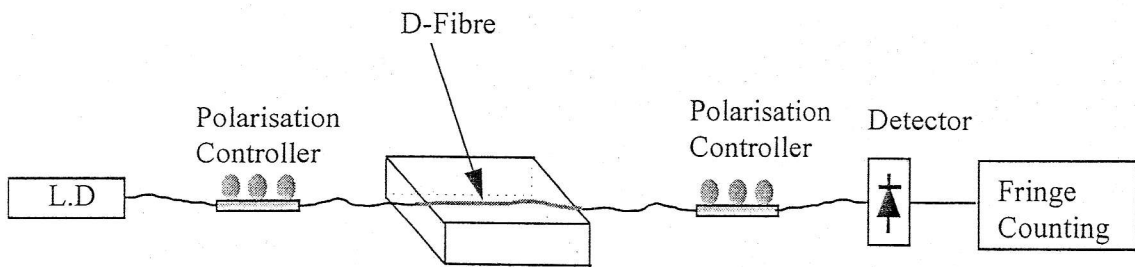


Fig 3. Experimental set-up.

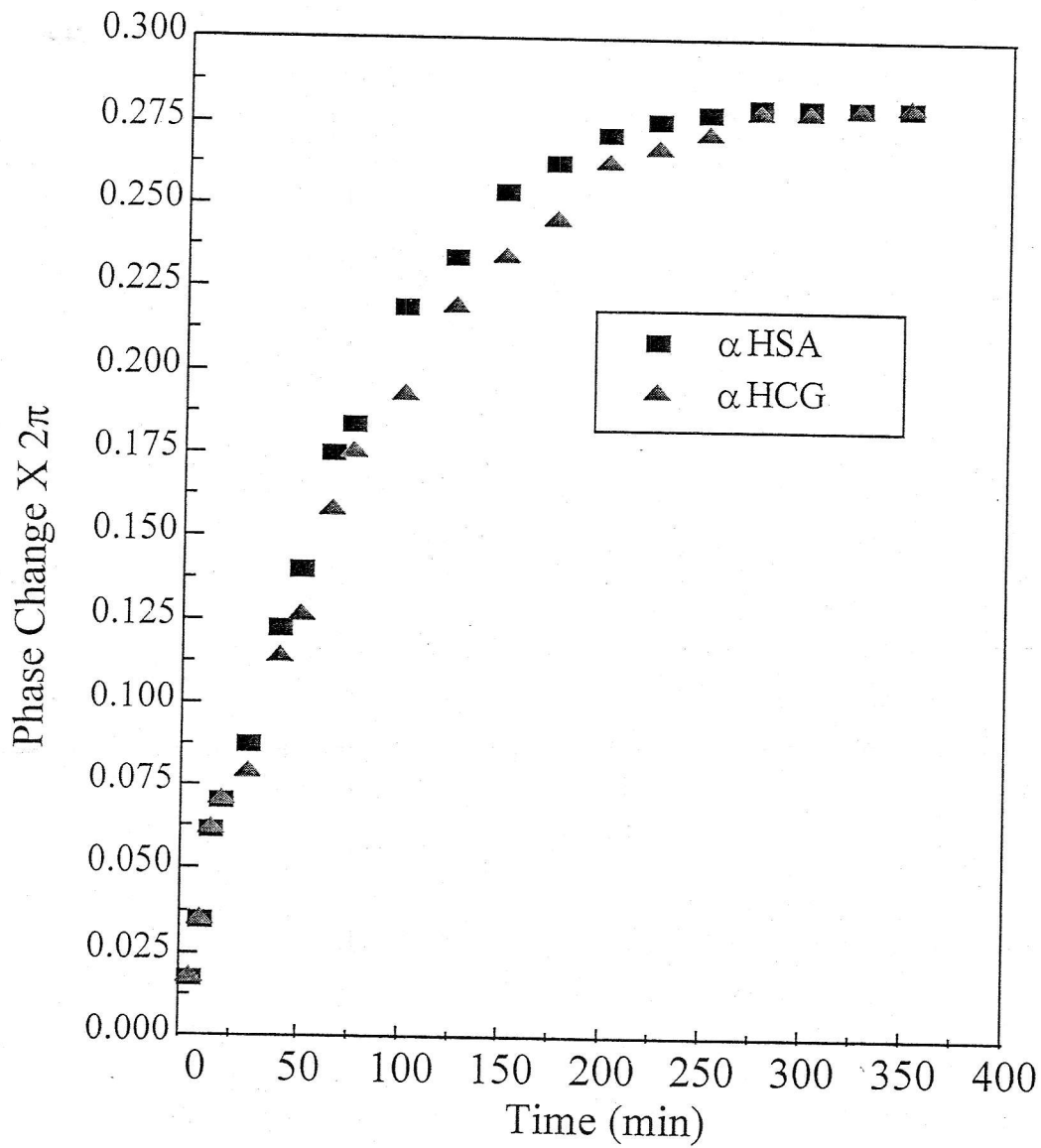


Fig 4. αHSA and αHCG adsorption shown as phase change measurement against time.

PRESENTATION OF A MASTER OF SCIENCE THESIS

REMOTE SUPERVISION OF TELECOMMUNICATION
TRANSPORT SYSTEMS AS A PART OF TMN

Master of Science Thesis

Author: Mr Željko V. Jungić

On April 10th, 1998 a promotion of a new Master of Science Thesis took place after the author's (Mr Željko V. Jungić) successful presentation.

The object of the thesis is to describe one solution of the system for telecommunication transport equipment remote supervision, which the author has developed and implemented within a number of telecommunication networks.

Telecommunication equipment supervision, that is error control, is one of the possible functions of the telecommunication management network - TMN.

The author has identified, through the general TMN model presentation, the place and role of his own solution, inside this complex TMN.

The importance of TMN implementation in up-to-date, very heterogeneous and complex telecommunication networks, as well as some experiences in these networks development in Republic of Srpska and all over the world, are outlined in the introduction and the second part of the thesis.

Many years ago, in 1985, the author recognized the importance of the remote supervision, control and measurement in the radio-relay transmission networks in the former Yugoslavia. The same year, the author started, with his colleagues from the Faculty of Electrical Engineering in Banja Luka, the development of a new microcomputer based system for remote supervision called CS RSCM 512/128 which has been used in telecommunication networks in Slovenia, Yugoslavia and later in the Republic of Srpska. These solutions have been incorporated and later presented in this thesis.

According to the papers quoted in the list of references, it can be also noted that since the creation of the first recommendations from M-30 series for TMN, which were defined on the CCITT Plenary Session in Melbourne in 1988, the author has made efforts to modify his own solution according to these recommendations.

The third part outlines the fundamental principles of TMN with a special emphasis on the physical and functional architecture. The elements of TMN physical architecture, TMN functions, as well as a presentation of the most important interfaces and protocols are described in detail. The author has also shown the role of his own solution within the global TMN.

In the fourth and fifth parts, which represent the essence of this paper, the author explained in detail his own CS RSCM system. The main system elements and their

functional and electrical characteristics are also presented. The precise description of all the Q-adapter functional blocks and mediator interface, with electrical schemes and signal timing diagrams in characteristic points, are illustrated.

The most important scientific contribution of this paper is given in the fifth part, where special input /output circuits applied in the solution, are described. These circuits highly enlarge the system immunity to interference, provide high security in transmission and network information processing and at the same time reduce implementation cost rapidly.

The frequency decoder description with hysteresis curve and the possibility for expanded area for application and realization in the form of monolithic integrated circuits in the standard CMOS technology deserves a special attention. In the paper, published in 1998 at the Yugoslav Conference ETAN in Sarajevo, Mr Jungić has proposed an original solution for a detector with hysteresis frequency transmission curve.

The seventh part of the thesis deals with the engineers' useful experience gained by designing and exploiting of circuits as well as the CS RSCM system circuits made in CMOS technology, with a special emphasis on the appearance of a latchup and the reasons for a system failure. The most common cases for the appearance of thyristor effect on input/output CMOS circuits structure, as well as the recommended steps for the system protection from this effect, are shown. The software system support, with the emphasis on the work with dynamic libraries and library functions for dynamic connection and specific problems related to operation system communications with exterior devices, are presented. A brief overview of the operation system characteristics from the aspect of software system realization for the remote supervision, is also given.

The presentation of a system for the future SDH transport networks management is given in the eighth part, and the comparison between SAM network and multilayer architecture applied to the OSI communication models is presented.

The new SDH radio-relay transport network construction and implementation, which is managed by its own SNM network, has just been finished, as the author showed in the ninth part and the importance of the CS RSCM solution for the management network is emphasized. A proposal for interconnection between his own solution of the analog and PDH transport equipment supervision and the new SNM network for SDH equipment management is given.

The purpose of the integrated network construction for supervision and control is the unique operative system exploitation and the use of the possibilities which the SDH network provides, in the sense of economic and reliable information transmission over existing DCC and ECC channels, within the section of STM-1 frame overhead.

The future network for transmission system management in Republic of Srpska, as well as the points and ways for the CS RSCM and SDH network integration are also illustrated.

Mentor :

Prof. Dr. Branko Dokić

ACKNOWLEDGEMENTS

The publishing of this issue of the Electronics, a journal of the Faculty of Electrical Engineering in Banja Luka, was enabled by electrical engineer graduates who entered their studies at the Faculty of Electrical Engineering in Banja Luka in 1967/68.

УПУТСТВО ЗА АУТОРЕ

У часопису ЕЛЕКТРОНИКА објављујемо научне и стручне радове из електронике, у најширем смислу, као што су: аутоматика, телекомуникације, рачунарска техника, енергетика, нуклеарна и медицинска електроника, анализа и синтеза електронских кола и система, нове технологије и материјали у електроници, итд. Осим научних, прегледних и стручних радова, презентујемо нове производе, приказујемо нове књиге, магистарске и докторске тезе. С циљем да се омогући унифицирање техничке обраде радова и поједностављење штампања часописа ЕЛЕКТРОНИКА, даје се ово упутство за ауторе.

Радови се достављају уреднику часописа електронском поштом или на адресу Факултета (обе адресе се налазе на полеђини прве корице) на дискети и одштампано у три примјерка.

Сва три примјерка рада треба да буду одштампана само са једне стране листа формата А4 (димензија 210x297 mm , односно ширине 8.27" , висине 11.69"), горње и доње маргине од 1" , лијеве и десне маргине од 1" , а за заглавље и нумерацију страница оставити 0.5" (header и footer су 0.5"). Рад може бити написан на српском или енглеском језику. Рад обавезно мора бити писан у двије колоне са размаком између колона од 0.5 cm. Сугерише се ауторима да радове обрађују на персоналном рачунару користећи процесор текста WORD FOR WINDOWS, а за слике графички програм CORELDRAW. Графикони иду из изворних програма, тј. из програма у којима су добијени. Рад не треба завршавати на почетку странице. Ако задња страница рукописа није попуњена, колоне на тој страници треба свести на исту дужину.

На средини прве странице рада написати у полуфету (bold) наслов рада словима величине 12pts. Затим, такође на средини прве странице помјерено за 1 проред у односу на наслов рада, треба навести имена аутора и имена институција у којима су запослени, величином слова којом су штампани и остали дијелови текста. Остале дијелове рукописа треба обрадити у двије колоне размакнуте за 10mm. Рад куцати у прореду величине 1 и величином слова не мањом од 10pts. Послије наслова рада и имена аутора слиједи кратак садржај на српском језику писан курзивом (italic). Поднаслов у рукопису писати у полуфету (bold) великим словима величине као у тексту (не мањим од 10pts). Сваки рад мора посједовати на почетку поднаслов УВОД, а на крају поднаслов ЗАКЉУЧАК и ЛИТЕРАТУРА. На крају рада налази се кратак садржај (Abstract) и наслов рада на енглеском језику са именима аутора.

Операторе и ознаке величина које не узимају бројне вриједности писати обичним словима, а ознаке величина које могу узимати бројне вриједности писати курзивом (italic). Једначине се пишу у једној колони са нумерацијом уз десну ивицу. Ако се не жели преламање једначине или слике, исте се могу ставити преко обе колоне.

Илустрације (табеле, слике, графикони и сл.) могу, по потреби, да буду шире од једне колоне. Изнад табеле треба да стоји натпис нпр: Табела 2. *Резултати експерименталних мјерења*. Слично важи за слике и графиконе, с тим што пропратни текст иде испод слике или графикана.

На крају рада треба пописати коришћену литературу оним редосљедом којим је позивана у тексту. Литературу у тексту треба наводити у угластим заградама, нпр: ...у [2] је показано...

INSTRUCTION FOR AUTHORS

In the review "Electronics", we publish the scientific and professional works from different fields of electronics in the broadest sense like: automatics, telecommunications, computer techniques, energetic, nuclear and medical electronics, analysis and synthesis of electronic circuits and systems, new technologies and materials in electronics etc. In addition to the scientific, reviewal and professional works, we present new products, new books, M. A. and D. Sc. theses.

In order to enable the unification of the technical arrangement of the works, to simplify the printing of the review "ELECTRONICS", we are giving this instruction for the authors of the works to be published in this professional paper.

The works are to be delivered to the editor of the review by the E-mail or to the address of the Electrical Engineering Faculty (both addresses are shown inside the front page) on a floppy and printed in three folds.

All of the three folds are to be printed on one side of the paper A4 format, 210 x 297 mm, i.e., 8.27 "width and 11.69 " height, upper and lower margins of 1", left and right margins of 1" and the header and footer are 0.5". The work may be written in Serbian or English language. Obligatory, the work has to be written in two columns with the spacing between columns of 0.5 cm. Our suggestion to the authors is to make their works on a PC using the word processor WORD FOR WINDOWS, and for the figures to use the graphic program CORELDRAW. The graphs are going from the original programs, i.e., from the programs received. The works should not be finished at the beginning of a page. If the last manuscript page is not full, the columns on that page should be made even.

The title of the work shall be written on the first page, in bold and 12 pts size. Also, on the first page, moved for one line spacing from title, the author's name together with the name of his institution shall be printed in the letter size of the remaining parts of the text. The remaining parts of the manuscript shall be done in two columns with 10 mm interspace. The work shall be typed with line spacing 1 and size not less than 10 pts. After the title of the work and the name of the author, a short content in Serbian language follows, written in italics. The subtitles in the text shall be written in bold, capital letters of the size as in the text (not less than 10 pts). Each work shall, at the beginning, comprise a subtitle INTRODUCTION, and, at the end, the subtitles CONCLUSION and BIBLIOGRAPHY. At the end of the work, there shall be a short abstract and the title in English accompanied with the names of authors.

The operators and size marks that do not use numerical values, shall be written in common letters. The size marks that can use numerical values shall be written in italics. The equations shall be written in one column with right edge numeration. If the breaking of equations or figures is not desired, those may be placed over both columns.

Illustrations (tables, figures, graphs etc.) may be wider than one column if necessary. Above a table there shall be a title for instance: Table 2. *The experimental measuring results*. The same applies to figures and graphs but the accompanying text comes underneath the figure of graphs.

At the end of each work, the used literature shall be listed in order as used in the text. The literature in the text, shall be enclosed in square brackets, for instance: ...in [2] shown is...



ELECTRONICS

Volume 2, Number 1, September 1998.

CONTENTS

Guest editor	1
Preface	2
Present Trends in Controlled Electrical Drives	3
<i>Sloban N. Vukosavić</i>	
The Basic Moving Average Algorithm of Present Count Digital Rate Meters.....	14
<i>Aleksandar Koturović, Vojislav Arandelković, Radomir Vukanović</i>	
The Gate Leakage Influence to the Mesfet Noise Modeling.....	18
<i>Branislav Milovanović, Vera Marković, Nataša Malesš-Ilić</i>	
Belgrade Grasping System	25
<i>Dejan Popović, Mirjana Popović</i>	
Suppression of Noise Contamination in Control Systems With Internal Model	33
<i>Milić R. Stojić, Milan S. Matijević</i>	
An Approach to the Design of a Self-Tuning Controller Using State Space Approach	43
<i>Branko Kovačević, Željko Đurović, Ljubiša Mišković</i>	
Comparative Analysis of the Visual Navigation Algorithms.....	51
<i>Stevica Graovac</i>	
Исползование Новблх Магнитнблх Материалов При Построении Датчиков Магнитнблх и Механических Величин.....	57
<i>Вийалий Ничога, Олеж Сокол-Куибловский</i>	
Comparative Analysis of MS Latches and Flip-Flops for High-Performance and Low-Power VLSI Systems.....	61
<i>Vladimir Stojanović, Vojin Oklobdžija</i>	
Optical D-Fibre Sensor for Biotechnological Applications	67
<i>F. A. Muhammad, H. S. Al-Raweshidy, J. M. Senior</i>	
PRESENTATION OF A MASTER OF SCIENCE THESIS:.....	75
Remote Supervision of Telecommunication Transport Systems as a Part of TMN	
<i>Branko L. Dokić</i>	
ACKNOWLEDGEMENT	77